

# Chapter 14

## Stellar rotation

### 14.1 Introduction

All stars rotate, as a consequence of the angular momentum they have accumulated during their formation process. Therefore, rotation is a fundamental property of stars, and the extent to which this affects their structure and evolution is an important question with a long history of investigation.

Stellar rotation rates are often expressed in terms of the equatorial velocity  $v_{\text{eq}}$ , which can be measured spectroscopically for most stars, although only in projection to our line of sight ( $v_{\text{eq}} \sin i$ ). Measured rotation velocities for main-sequence stars vary strongly with mass, as shown in Fig. 14.1, with typical values of  $< 10$  km/s for low-mass stars ( $\lesssim M_{\odot}$ , e.g. the Sun has  $v_{\text{eq}} = 2.0$  km/s) to hundreds of km/s for relatively massive main-sequence stars (O-, B- and A-type stars,  $\gtrsim 1.5 M_{\odot}$ ). A more physically meaningful measure of rotation is to compare  $v_{\text{eq}}$  to the *critical* or *break-up velocity*  $v_{\text{cr}}$ , the velocity for which the centrifugal force at the equator equals gravity (or in other words, the velocity of a test particle in a circular orbit at the equator). As long as  $v_{\text{eq}} \ll v_{\text{cr}}$ , we can expect rotation to have only a small effect on the structure, and we are probably justified to ignore it. A simple estimate of  $v_{\text{cr}}$ , assuming spherical symmetry, is  $v_{\text{cr}} = (GM/R)^{1/2}$ . For main-sequence stars, which follow a mass-radius relation  $R/R_{\odot} \approx (M/M_{\odot})^{0.8}$ , this gives  $v_{\text{cr}} \approx 440(M/M_{\odot})^{0.1}$  km/s, only weakly dependent on stellar mass. We see that low-mass stars are generally very slow rotators, but massive stars can spin at a significant fraction of the critical velocity. This is why the effects of rotation on stellar evolution have mostly been studied in the context of massive stars.

Inclusion of rotation complicates our description of stars, because it breaks the assumed spheri-

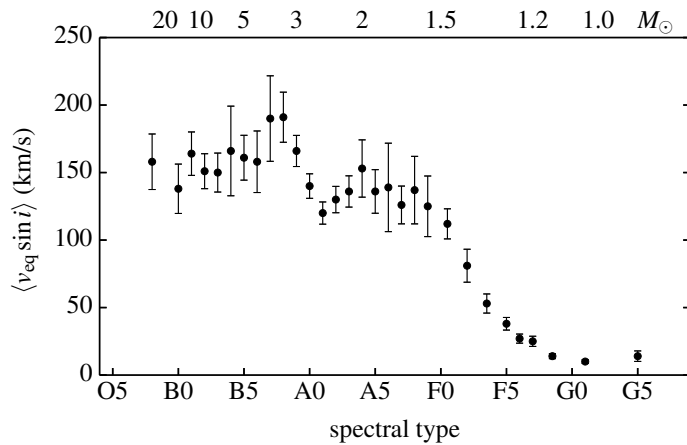


**Figure 14.1.** Average projected rotational velocities of main-sequence stars, as a function of spectral type. Approximate masses on the main sequence are indicated along the top axis. The error bars show the uncertainty in the mean value due to the limited sample sizes. Note that if the rotation axes are randomly oriented in space, the actual mean equatorial velocities  $\langle v_{\text{eq}} \rangle$  are a factor  $4/\pi$  larger. Data taken from Fukuda (1982).

cal symmetry. A rotating star is a three-dimensional object, although to a good approximation still axi-symmetric. Another complicating factor is that stars cannot generally be expected to rotate uniformly, i.e. with a constant angular velocity  $\Omega$  throughout. A case in point is the Sun, which rotates differentially both in terms of latitude across the surface (the equator has a shorter rotation period than the polar regions) and in terms of depth below the surface, as has been revealed by helioseismology. While differential rotation is only modest in the Sun, we can expect it will be greatly amplified during the course of stellar evolution; especially after the main sequence, when the core contracts and thus speeds up its rotation rate, while the envelope expands and slows down. The treatment of internal *angular momentum transport* is therefore an important, although uncertain, aspect of the evolution of rotating stars.

Even for stars whose structure and evolution are not directly affected by rotation, the inverse is not true: their rate and state of rotation will change as a result of stellar evolution. To understand the observed rotation rates of stars – both on the main sequence and beyond, including stellar remnants such as white dwarfs and neutron stars – we should take into account not only internal angular momentum transport but also the *angular momentum loss* associated with mass loss. For both the transport and the loss of angular momentum, the presence and/or generation of *magnetic fields* in the star can play a crucial role.

## 14.2 The stellar structure equations in three dimensions

As an intermezzo, we start by generalizing the stellar structure equations from spherical symmetry (eqs. 7.1–7.4) to three dimensions. This is useful not only for describing a rotating star, but any star that is deformed due to lack of spherical symmetry, e.g. in a binary system (Chapter 15). Because stars are gaseous objects, the three-dimensional structure equations are specific forms of the Navier-Stokes equations of hydrodynamics.

**Mass conservation** Mass conservation in fluid dynamics is expressed by the *continuity equation*,

$$\frac{\partial \rho}{\partial t} = -\vec{\nabla} \cdot (\rho \vec{v}). \quad (14.1)$$

The left-hand side is rate of change of the mass inside a unit volume, while the right-hand side expresses the net mass flux that enters or leaves this unit volume. For a star in complete equilibrium, both sides of eq. (14.1) vanish.

The continuity equation is equivalent to the mass conservation equation (2.3) we derived for spherical symmetry, even though it looks very different. One reason is that in Chapter 2 we considered a spherical mass shell, which loses its physical meaning in the general three-dimensional case. To see the relation, consider the partial derivatives of the mass coordinate  $m$  with respect to  $r$  and  $t$ , eq. (2.2), and in each case take the second partial derivative with respect to the other variable to obtain two expressions for  $\partial^2 m / \partial r \partial t$ . These expressions must be equal, which yields

$$\frac{\partial \rho}{\partial t} = -\frac{1}{r^2} \frac{\partial(r^2 \rho v)}{\partial r}.$$

This is just eq. (14.1) in spherical coordinates.

**Momentum conservation and hydrostatic equilibrium** The net acceleration  $\vec{a} = d\vec{v}/dt$  experienced by a parcel of gas is due to the forces exerted by the pressure gradient  $\vec{\nabla}P$ , by gravity

$\vec{g} = -\vec{\nabla}\Phi_{\text{gr}}$ , where  $\Phi_{\text{gr}}$  is the gravitational potential, and perhaps due to other external forces together giving an acceleration  $\vec{a}_{\text{ext}}$ . We will here ignore the acceleration term due to viscosity, which is generally very small in a stellar gas. The equation of motion is thus

$$\frac{d\vec{v}}{dt} = \frac{\partial \vec{v}}{\partial t} + (\vec{v} \cdot \vec{\nabla})\vec{v} = -\frac{1}{\rho} \vec{\nabla}P - \vec{\nabla}\Phi_{\text{gr}} + \vec{a}_{\text{ext}}. \quad (14.2)$$

The first equality relates the Lagrangian derivative of the velocity  $d\vec{v}/dt$  to the Eulerian partial derivatives with respect to  $t$  and  $\vec{r}$ . Eq. (14.2) is another of the Navier-Stokes equations of fluid dynamics, the equivalent of which in spherical symmetry is eq. (2.10) for the case where the only external force is due to gravity.

For a star in hydrostatic equilibrium the net acceleration vanishes everywhere and we obtain

$$\frac{1}{\rho} \vec{\nabla}P = -\vec{\nabla}\Phi_{\text{gr}} + \vec{a}_{\text{ext}}. \quad (14.3)$$

which is the equivalent of eq. (2.12) if we ignore external forces other than gravity. In a rotating star,  $\vec{a}_{\text{ext}}$  would result from the centrifugal force (see Sect. 14.3). In spherical symmetry, the gravitational acceleration has a very simple form,  $\vec{g} = -(GM/r^2)\hat{e}_r$ . In the general three-dimensional case, the gravitational potential must be derived from the density distribution  $\rho(\vec{r}, t)$  using Poisson's equation

$$\nabla^2\Phi_{\text{gr}} = 4\pi G \rho, \quad (14.4)$$

which must be solved together with eq. (14.3) or eq. (14.2).

**Energy conservation** We can use the same reasoning as in Section 5.1 to derive the equation for energy conservation in three dimensions, but we should write the net amount of energy flowing into or out of a unit volume as  $\vec{\nabla} \cdot \vec{F}$ . Here  $\vec{F}$  is the vector describing the magnitude and direction of the total energy flux at a certain position  $\vec{r}$  inside the star. For a unit mass of gas, we then obtain the 3D equivalent of eq. (5.6),

$$\frac{1}{\rho} \vec{\nabla} \cdot \vec{F} = \epsilon - T \frac{ds}{dt}. \quad (14.5)$$

Here we have combined nuclear energy generation and neutrino losses into  $\epsilon = \epsilon_{\text{nuc}} - \epsilon_{\nu}$ , and replaced  $\epsilon_{\text{gr}}$  by  $-Tds/dt$  (eq. 5.5). For a star in thermal equilibrium, the last term in eq. (14.5) vanishes. We note that in the general 3D case, the local luminosity  $l = 4\pi r^2 F$  loses its physical meaning, as does the mass coordinate  $m$ .

**Radiative energy transport** In Section 5.2.2 we derived an equation (5.15) for the radiative energy flux in the diffusion approximation,

$$\vec{F}_{\text{rad}} = -\frac{4acT^3}{3\kappa\rho} \vec{\nabla}T, \quad (14.6)$$

which reduces to eq. (5.16) for the radiative temperature gradient in spherical symmetry. If convection, or other bulk gas motions that carry heat are present, their energy fluxes should be added to  $\vec{F}_{\text{rad}}$  to give the total energy flux  $\vec{F}$ .

## 14.3 The structure of rotating stars

Rotation introduces additional forces on the star. A gas element that rotates with an angular velocity  $\vec{\Omega}$  experiences a centrifugal acceleration equal to  $\vec{a}_c = -\vec{\Omega} \times (\vec{\Omega} \times \vec{r})$ , where  $\vec{r}$  is its position vector relative to the centre of mass in the co-rotating frame. In addition, if a gas element moves with respect to the overall rotation velocity, it also experiences a Coriolis force  $-\vec{\Omega} \times d\vec{r}/dt$ . We will further ignore this complication and only consider the centrifugal force.

The problem is greatly simplified if the centrifugal force can be written as the gradient of a potential, which can then be combined with the gravitational potential  $\Phi_{\text{gr}}$  in eq. (14.2). This is true in the case of uniform rotation, which we discuss below; and also if  $\vec{\Omega}$  is constant on cylinders, i.e. if it only depends on the distance from the rotation axis. However, for the more general case of differential rotation, where  $\vec{\Omega}$  has a different dependence on  $\vec{r}$ , this simplification is not possible.

### 14.3.1 Solid-body rotation

Let us consider the simplest case: uniform rotation, also called solid-body rotation or rigid rotation, where  $\Omega$  is constant throughout the star. We choose a cylindrical coordinate system  $(\xi, \phi, z)$ , with the  $z$ -axis aligned with the rotation axis and  $\xi = (x^2 + y^2)^{1/2}$  is the distance from the rotation axis. In that case

$$\vec{a}_c = \Omega^2 \xi \hat{e}_\xi, \quad (14.7)$$

which can be derived from a potential as follows:

$$\vec{a}_c = -\vec{\nabla}\Phi_{\text{cf}} \quad \text{with} \quad \Phi_{\text{cf}} = -\frac{1}{2}\Omega^2 \xi^2. \quad (14.8)$$

We can then write the combined gravitational and centrifugal potential as  $\Phi = \Phi_{\text{gr}} + \Phi_{\text{cf}}$ , and the equation for hydrostatic equilibrium (14.3) becomes

$$\vec{\nabla}P = -\rho \vec{\nabla}\Phi. \quad (14.9)$$

Thus, at any point the pressure gradient is parallel with the gradient of the potential: this implies that surfaces of constant potential are also surfaces of constant pressure,  $P = P(\Phi)$ . From eq. (14.9), we then find that also  $\rho = -dP/d\Phi = \rho(\Phi)$  is constant on an equipotential surface. If in addition the composition is homogeneous, the equation of state implies that also the temperature is constant on equipotential surfaces,  $T = T(\Phi)$ . For the ideal-gas equation of state, a more general consequence is that the ratio  $T/\mu$  is constant on equipotential surfaces, but not necessarily  $T$  itself if the mean molecular weight varies over an equipotential surface.

To some extent, we have now regained a one-dimensional description of the structure of a rotation star, because  $P$ ,  $\rho$  and in most cases  $T$  only depend on one variable, the potential  $\Phi$ , which can then be used as a coordinate measuring depth within the star.

### 14.3.2 The Roche model

The shape of an equipotential surface is determined by the density distribution through Poisson's equation (14.4). Because the star is no longer spherical, the gravitational potential itself will depend on the rotation rate. To obtain an idea of the geometry of a rotating star, we can approximate the gravitational potential by that of a point mass, as if all the mass of the star were concentrated at its centre. This is the so-called *Roche model*, which has the big advantage that the gravitational field is independent of rotation. Since stars are generally quite centrally concentrated, this is a reasonable approximation for the outer layers.

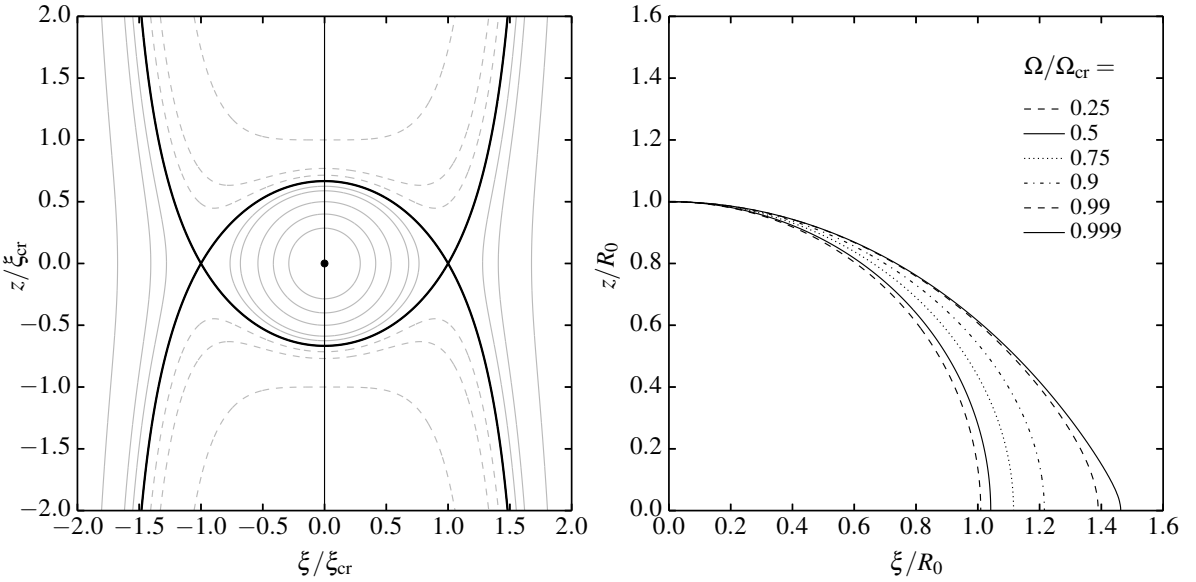


**Figure 14.2.** (a, left) Lines of constant potential  $\Phi$  in the meridional plane  $(\xi, z)$  in the Roche model. The rotation axis is shown as a vertical line. The critical potential surface  $\Phi_{\text{cr}}$  is indicated with a thick line; other solid curves have  $\Phi < \Phi_{\text{cr}}$  while dashed curves have  $\Phi > \Phi_{\text{cr}}$ . The axes are scaled to the critical equatorial distance  $\xi_{\text{cr}}$ . (b, right) The corresponding shape of a star in the meridional plane for different values of  $\Omega/\Omega_{\text{cr}}$ , between 0.25 and 0.999. Here the axes are scaled to the radius  $R_0$  of a non-rotating star.

We thus write

$$\Phi_{\text{gr}} = -\frac{GM}{r}, \quad (14.10)$$

so that, using  $r^2 = \xi^2 + z^2$ ,

$$\Phi = -\frac{GM}{(\xi^2 + z^2)^{1/2}} - \frac{1}{2}\Omega^2\xi^2. \quad (14.11)$$

In Fig. 14.2a, a number of surfaces with  $\Phi = \text{constant}$  is plotted in the  $(\xi, z)$  plane. It is clear that a critical surface exists, inside which the surfaces are closed and spheroidal in shape, and outside which the surfaces are open to infinity. The critical surface has  $\vec{g}_{\text{eff}} = -\vec{\nabla}\Phi = 0$  along the equator, at  $z = 0$  and  $\xi = \xi_{\text{cr}}$ . In other words, the gravitational and centrifugal acceleration exactly cancel each other at this location, which is the condition for break-up rotation. Applying this condition, which is equivalent to  $(\partial\Phi/\partial\xi)_{z=0} = 0$ , yields

$$\xi_{\text{cr}}^3 = \frac{GM}{\Omega^2}. \quad (14.12)$$

The critical surface intersects the rotation axis ( $\xi = 0$ ) at  $z = z_{\text{cr}}$ , which gives  $z_{\text{cr}} = \frac{2}{3}\xi_{\text{cr}}$  using eq. (14.11). The surface of a star in hydrostatic equilibrium must correspond to an equipotential surface inside the critical surface.

To study the implications, let us start with a non-rotating star with radius  $R_0$  and gradually spin it up, increasing  $\Omega$  while maintaining rigid rotation. Along the rotation axis  $\Phi$  is independent of  $\Omega$ ; thus, the stellar radius at the poles,  $R_p$ , will remain unchanged and equal to  $R_0$ . At other latitudes the effective gravitational acceleration decreases, most strongly in the equatorial regions which will start bulging out, giving the star a flattened shape. When  $\Omega$  reaches the critical value where  $\vec{g}_{\text{eff}} = 0$  at

the equator, the equatorial radius  $R_{\text{eq}}$  equals exactly  $\frac{3}{2}$  times the polar radius  $R_p = R_0$ . The critical or break-up angular velocity is, therefore,

$$\Omega_{\text{cr}} = \left( \frac{GM}{R_{\text{eq},\text{cr}}^3} \right)^{1/2} = \left( \frac{8}{27} \frac{GM}{R_p^3} \right)^{1/2} \quad (14.13)$$

and the corresponding critical equatorial velocity  $v_{\text{cr}} = R_{\text{eq}}\Omega_{\text{cr}}$  is

$$v_{\text{cr}} = \left( \frac{GM}{R_{\text{eq},\text{cr}}} \right)^{1/2} = \left( \frac{2}{3} \frac{GM}{R_p} \right)^{1/2}. \quad (14.14)$$

We see that, as a result of rotational flattening,  $v_{\text{cr}}$  is a factor  $\sqrt{2/3} \approx 0.82$  smaller than the simple estimate we made in Sect. 14.1. Fig. 14.2b shows the shape of a star in the Roche model for different values of  $\Omega/\Omega_{\text{cr}}$ . The shape is very close to spherical as long as  $\Omega$  is small compared to  $\Omega_{\text{cr}}$ . For  $\Omega/\Omega_{\text{cr}} = 0.5$ ,  $R_{\text{eq}} = 1.04R_p$  and for  $\Omega/\Omega_{\text{cr}} = 0.9$ ,  $R_{\text{eq}} = 1.21R_p$ .

While these results are strictly correct only in the Roche model, they still hold to good approximation for realistic mass distributions, as long as rotation is rigid. In particular, the expectation that  $R_p \approx R_0$  holds to within a few percent in models in which the mass distribution inside the star is taken into account; e.g. compare Fig. 14.2b to MAEDER's Fig. 2.2 for a  $20 M_\odot$  star. Several additional effects also become apparent in such detailed models. Because the centrifugal force decreases the effective gravity inside the star, the weight of the envelope is reduced and therefore the central pressure and temperature are smaller than in a non-rotating star. This results in a decrease of the luminosity, by up to several percent (depending on stellar mass) if  $\Omega$  approaches the critical value.

### 14.3.3 Gravity darkening

The equation of radiative transport (14.6) can be written as

$$\vec{F}_{\text{rad}} = -K_{\text{rad}} \vec{\nabla} T \quad \text{with} \quad K_{\text{rad}} = -\frac{4acT^3}{3\kappa\rho}, \quad (14.15)$$

where  $K_{\text{rad}}$  can be seen as the radiative ‘conductivity’. Because the opacity  $\kappa$  is a function of  $\rho$  and  $T$ , which both depend only on  $\Phi$  in a rigidly rotating star,<sup>1</sup> also  $K_{\text{rad}}$  is a function of  $\Phi$ . Furthermore, because  $T = T(\Phi)$  and  $\vec{\nabla}\Phi = -\vec{g}_{\text{eff}}$ , we can write this as

$$\vec{F}_{\text{rad}} = -K_{\text{rad}} \frac{dT}{d\Phi} \vec{\nabla}\Phi \equiv -f(\Phi) \vec{\nabla}\Phi = f(\Phi) \vec{g}_{\text{eff}}. \quad (14.16)$$

Thus, the radiative flux is everywhere parallel and proportional to the effective gravitational acceleration, the proportionality factor depending only on  $\Phi$ . However, because  $\vec{g}_{\text{eff}}$  varies across an equipotential surface, so does  $\vec{F}_{\text{rad}}$ . The radiative flux is smaller in regions with lower effective gravity, and vice versa. This is known as the Von Zeipel theorem, after Von Zeipel who derived it in 1924. Eq. (14.16) holds at every point in the star, including the photosphere. The flux of a rotating star varies across the stellar surface, with the equatorial regions emitting a smaller flux and thus appearing dimmer and cooler than the polar regions. This effect is called *gravity darkening*. Because the surface flux equals  $F = \sigma T_{\text{eff}}^4$ , we expect  $T_{\text{eff}} \propto g_{\text{eff}}^{0.25}$  for a purely radiative star.

Both the distortion of the shape of rapidly rotating stars and the associated gravity darkening have been observed using optical interferometry. The A-type star Altair ( $\alpha$  Aql) with a mass of  $1.8 M_\odot$  has a substantially flattened shape with  $R_{\text{eq}}/R_p \approx 1.24$  which implies  $\Omega \approx 0.92 \Omega_{\text{cr}}$  in the Roche model. The reconstructed image of the star clearly shows the effect of equatorial gravity darkening

---

<sup>1</sup>Provided the composition is also constant on an equipotential surface, Sect. 14.3.1.

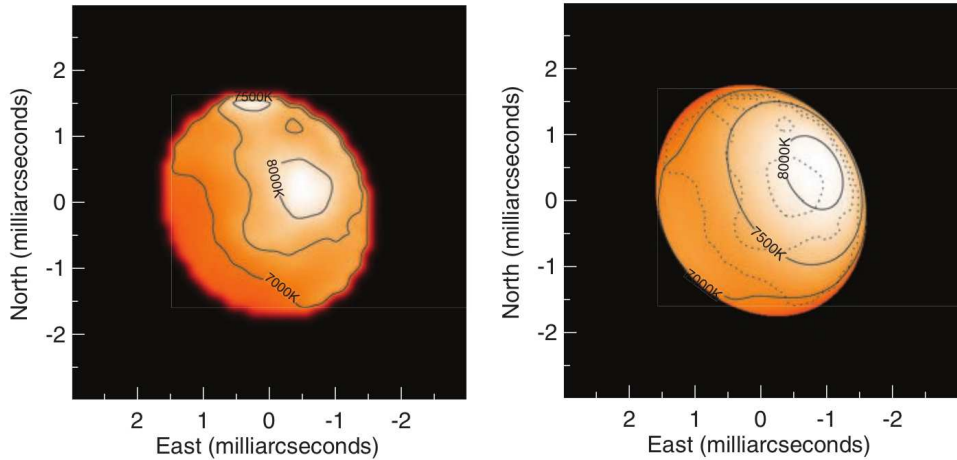


**Figure 14.3.** (left) Image of the rapidly rotating star Altair obtained with near-infrared wavelength interferometry. The contours show the corresponding blackbody temperatures. (right) The corresponding best-fitting Roche model with gravity darkening. Figures from Monnier et al. (2007).

(see Fig. 14.3). These effects are even stronger in the Be star Achernar ( $\alpha$  Eri,  $M \approx 8 M_\odot$ ) which rotates at 98% of its critical angular velocity and has  $R_{\text{eq}}/R_p = 1.35$  and  $T_{\text{eff},\text{eq}}/T_{\text{eff},p} = 0.74$ .<sup>2</sup>

#### 14.3.4 Von Zeipel's paradox and meridional circulation

You may have noticed an apparent contradiction in the previous sections: we found that  $T = T(\Phi)$  inside a rigidly rotating star, and yet at the stellar surface, which also has  $\Phi = \text{constant}$ , the temperature  $T_{\text{eff}}$  is *not* constant. In fact, the problem goes deeper than this, as first pointed out by Von Zeipel in 1924. For a star in thermal equilibrium, energy conservation implies, by eq. (14.5),

$$\vec{\nabla} \cdot \vec{F} = \epsilon\rho. \quad (14.17)$$

Let us assume  $\vec{F} = \vec{F}_{\text{rad}}$  and take the divergence of eq. (14.16),

$$\begin{aligned} \vec{\nabla} \cdot \vec{F} &= -\frac{df}{d\Phi} (\vec{\nabla}\Phi \cdot \vec{\nabla}\Phi) - f(\Phi) \nabla^2\Phi \\ &= -\frac{df}{d\Phi} |\vec{\nabla}\Phi|^2 - f(\Phi) [4\pi G\rho - 2\Omega^2]. \end{aligned} \quad (14.18)$$

In the last step we have used Poisson's equation for  $\nabla^2\Phi_{\text{gr}}$ , while  $\nabla^2\Phi_{\text{cf}} = -\nabla^2(\frac{1}{2}\xi^2\Omega^2) = -2\Omega^2$  for  $\Omega = \text{constant}$ . All factors appearing on the right-hand side of eq. (14.18) depend only on  $\Phi$ , except for  $|\vec{\nabla}\Phi|$ , which varies across an equipotential surface. Therefore,  $\vec{\nabla} \cdot \vec{F}$  cannot be constant on an equipotential surface. On the other hand, the right-hand side of eq. (14.17) is only a function of  $\Phi$  and therefore *is* constant on an equipotential surface. This means that *a uniformly rotating star cannot be simultaneously in hydrostatic, radiative and thermal equilibrium*. This is known as Von Zeipel's paradox.

The solution was proposed independently by Eddington and Vogt in 1925. Because  $\vec{\nabla} \cdot \vec{F} \neq \epsilon\rho$  everywhere on an equipotential surface, some parts of the surface are heated ( $\vec{\nabla} \cdot \vec{F} < \epsilon\rho$ , which

<sup>2</sup>In both stars, as well as in other stars where gravity darkening has been observed, the relation between  $T_{\text{eff}}$  and  $g_{\text{eff}}$  appears to have a smaller exponent than the expected 0.25 (about 0.19 and 0.17 for Altair and Achernar, respectively). This may be explained either by differential rotation, or by convection contributing to the total flux. In the case of convective energy transport eq. (14.16) does not hold; instead, for low-mass stars with convective envelopes it has been shown that  $T_{\text{eff}} \propto g_{\text{eff}}^{0.08}$ .

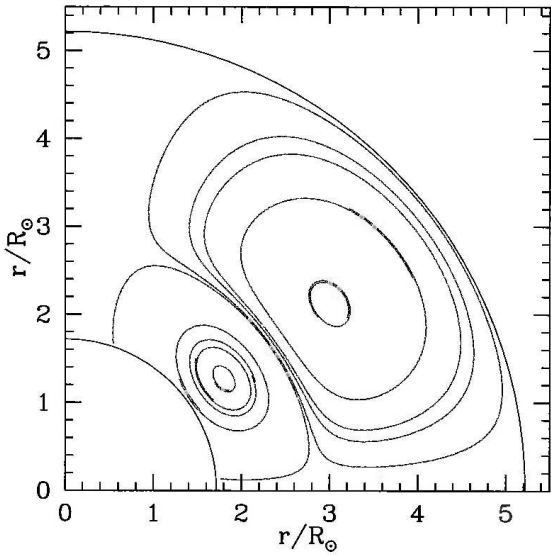


**Figure 14.4.** Example of the meridional circulation pattern inside a  $20 M_{\odot}$  star, about halfway through its main-sequence phase. Two circulation loops are present: in the inner loop the gas flow is clockwise, rising along the polar (vertical) axis and descending in the equatorial plane, while in the outer loop the flow is in the opposite sense. Only one quadrant is shown; the pattern is rotationally symmetric around the vertical axis and mirror-symmetric about the equatorial plane. The circle at  $r \approx 1.7 R_{\odot}$  indicates the edge of the convective core. Figure from MAEDER.

means  $ds/dt > 0$  by eq. 14.5) and other parts are cooled ( $\vec{\nabla} \cdot \vec{F} > \epsilon\rho$ ). Local heating of the gas causes expansion and an upward buoyancy force relative to the surroundings, while local cooling produces the opposite effect. As a result, a circulation pattern sets in where gas rises up at certain latitudes in the star, e.g. near the poles, gas sinks down at other latitudes, e.g. near the equator, and mass conservation ensures that gas travels horizontally inbetween these latitudes. Because of axial symmetry, the flow occurs in the meridional plane, hence the term *meridional circulation*. The gas flow transports energy, in addition to the radiative flux  $\vec{F}_{\text{rad}}$ . The star will then adjust its thermal structure such that, averaged over an equipotential surface,  $\langle \vec{\nabla} \cdot \vec{F} \rangle = \epsilon\rho$  and the star is globally still in thermal equilibrium.

The theory of meridional circulation is complicated by the fact that the flow also transports *angular momentum*, and thus the rotation state of the star is changed (it is no longer uniform), which in turn modifies the circulation pattern, etc. This turns out to be a very hard problem to solve. Stellar models in which this feedback effect is taken into account show that, in general, two circulation patterns develop, one in which matter flows up along the rotation axis and down along the equatorial plane, and another with a flow pattern in the opposite direction (see Fig. 14.4 for an example). This is related to the factor  $(4\pi G\rho - 2\Omega^2)$  in eq. (14.18), which changes sign when  $\rho < \Omega^2/(2\pi G)$ , i.e. in the low-density outer envelope of the star. The sizes and locations of these circulation loops depend on the mass, radius and rotation velocity of the star, and they change as the star evolves.

An important consequence of the circulation, if it is fast enough, is that matter from the central regions is transported and mixed with envelope material. Thus, matter whose composition has changed by nuclear reactions can be observed at the stellar surface. Whether this is a noticeable effect depends on the *timescale* of the circulation, also called the Eddington-Sweet timescale  $\tau_{\text{ES}}$ . Because the circulation is driven by a thermal instability, the timescale is related to the thermal timescale  $\tau_{\text{KH}}$  of the star, and we expect the timescale to be shorter for more rapid rotation. One can derive that, to an order of magnitude,

$$\tau_{\text{ES}} \approx \tau_{\text{KH}} \frac{2\pi G\bar{\rho}}{\Omega^2} \approx 5\tau_{\text{KH}} \left( \frac{\Omega}{\Omega_{\text{cr}}} \right)^{-2}, \quad (14.19)$$

where  $\bar{\rho} \approx 3M/(4\pi R^3)$  is the average density, and the expression (14.13) for the critical angular velocity is used in the last equality. We can compare the circulation timescale to the nuclear timescale for main-sequence stars, using eqs. (2.36) and (2.37) and adopting a mass-radius relation  $(R/R_{\odot}) \approx$

$$(M/M_{\odot})^{0.8},$$

$$\frac{\tau_{\text{ES}}}{\tau_{\text{nuc}}} \approx 0.015 \left( \frac{M}{M_{\odot}} \right)^{0.2} \left( \frac{\Omega}{\Omega_{\text{cr}}} \right)^{-2}. \quad (14.20)$$

For the Sun, with  $\Omega/\Omega_{\text{cr}} \approx 0.008$ , we find  $\tau_{\text{ES}} \approx 200\tau_{\text{nuc}}$ : meridional circulation is negligibly slow inside the Sun, and the same is true for other slowly rotating stars and for low-mass stars in general. On the other hand, massive stars typically rotate at a substantial fraction of their critical velocity. For a  $20 M_{\odot}$  star, eq. (14.20) indicates that  $\tau_{\text{ES}} < \tau_{\text{nuc}}$  when  $\Omega/\Omega_{\text{cr}} \gtrsim 0.2$ , so that even moderate rotation rates induce circulations that may affect the composition of the star during its main-sequence lifetime.

### 14.3.5 Differential rotation and angular momentum transport

Even if a star initially rotates as a solid body, this state may not necessarily persist for very long. As argued above, the meridional circulations that set in transport angular momentum and lead to non-uniform rotation. In addition, evolutionary changes in the structure induce differential rotation, already during the main-sequence phase, as the central parts of the star tend to contract and the outer layers expand (Sect. 9.3). To see the consequences, let us assume the star is not rotating too rapidly so that it is still approximately spherical in shape. The angular momentum of a spherical shell at radius  $r$  equals  $\Delta J = \frac{2}{3}r^2\Omega\Delta m$ ; that is, the *specific* angular momentum (angular momentum per unit mass) of such a shell is  $j = \frac{2}{3}r^2\Omega$ . If each mass shell conserves its own angular momentum, then  $r^2\Omega$  is constant for each shell. The contracting central parts of the star will experience an increase in angular velocity ( $\Omega \propto r^{-2}$ ) while the expanding outer layers will slow down their rotation rate. Thus,  $\Omega(r)$  is expected to decrease from the centre outwards, and the profile will get steeper over time as the star evolves.

In recent years it has become possible to measure the internal rotation profiles of stars by the technique of stellar seismology. This has first been applied to the Sun, revealing that the radiative inner part of the Sun rotates as a solid body, while the convective outer layers show some degree of differential rotation in latitude, but little in the radial direction (see Fig 14.5). Recently, the internal rotation profiles of red giants and subgiants have been measured with data from the *Kepler* satellite. These observations show that the cores of red giants indeed rotate faster than their envelopes, but the contrast in  $\Omega$  between core and envelope is much smaller than expected from simply considering local angular momentum conservation, as we did above. Similarly, the remnants of stellar evolution, white dwarfs and newly-formed neutron stars, rotate much slower than expected from local angular

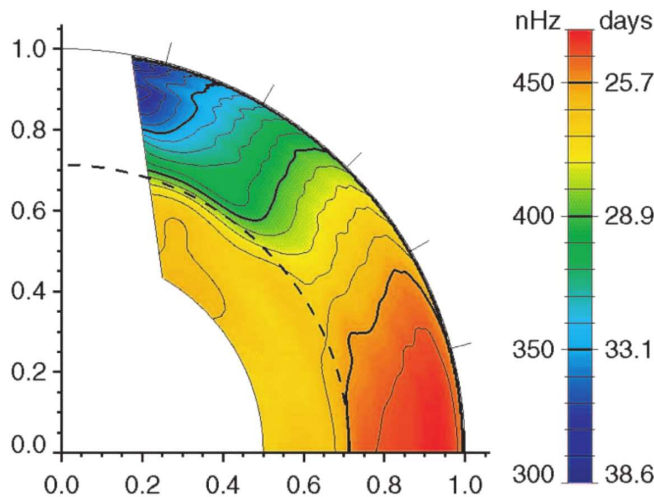


**Figure 14.5.** Internal angular velocity profile ( $\Omega/2\pi$ ) of the Sun, as deduced from helioseismology. The rotation axis is vertical, the horizontal axis is in the equatorial plane. The dashed line at  $r/R_{\odot} = 0.71$  indicates the boundary between the radiative interior, which has nearly constant  $\Omega$ , and the convective envelope, which shows differential rotation. Relatively fast rotation is shown in red, slow rotation in blue. Figure from Brun & Toomre (2002).

momentum conservation. Clearly, there are processes at work that counteract the differential rotation induced by structural changes during evolution, by transporting angular momentum from the core outwards. However, the nature and efficiency of these angular momentum transport processes is still very uncertain.

### Angular momentum transport in radiative regions

An important process to consider in radiative regions is the *shear* between gas layers moving with different velocities relative to each other. If the velocity gradient becomes larger than a certain critical limit, the shear flow becomes unstable to turbulence. The resulting turbulent eddies have a large effective viscosity, resulting in a torque that tends to reduce the difference in angular velocity. This *shear instability* is the most important of a range of hydrodynamical instabilities that may occur in a situation of differential rotation. The angular momentum transport induced by these instabilities and by meridional circulations have been included, in parameterized form, in stellar evolution calculations of rotating stars (see Sec. 14.4). However, such models cannot reproduce the rigid rotation of the solar interior, and they predict rotation rates of red-giant cores, white dwarfs and neutron stars that are too fast compared to observations. Therefore, additional and more efficient angular momentum transport mechanisms must operate. Possible mechanisms are internal gravity waves (*g*-mode oscillations) and torques exerted by internal *magnetic fields*.

### Convective regions

The situation in convective regions of a star is very different, because the turbulent convective motions are much more efficient at transporting angular momentum than any of the mechanisms discussed above. The large turbulent viscosity might be expected to rapidly reduce any differential rotation present and lead to rigid rotation (constant  $\Omega$ ) of the entire convective region. This is what is commonly assumed in models of rotating stars. However, this is correct only if the turbulence is isotropic, and this is not the case in a stellar convection zone. The turbulent motions are driven by the temperature gradient and thus occur mainly in the vertical (radial) direction. If one assumes that the largest-scale eddies dominate the flow and that these conserve their angular momentum, the angular velocity profile of a convective region would behave as  $\Omega \propto \xi^{-2}$ , where  $\xi$  is the distance from the rotation axis. The real situation may be somewhere in between these two extremes. That the actual situation is more complicated is also indicated by the observed solar rotation profile (Fig. 14.5), and confirmed by three-dimensional simulations of convection.

## 14.4 Stellar evolution with rotation

By making some simplifying assumptions, it has been possible to include the effects of rotation in one-dimensional stellar evolution codes. We saw in Sec. 14.3.1 that in the case of rigid rotation, the pressure, density and temperature are functions only of the potential  $\Phi$ , which can then be used as a one-dimensional coordinate. In the more general case of differential rotation, which naturally develops during stellar evolution, this is no longer possible. The centrifugal acceleration can not be derived from a potential, and eq. (14.9) no longer holds. Surfaces of constant pressure do not coincide with equipotential surfaces, nor with surfaces of equal density, but these surfaces are inclined with respect to each other. This situation is called *baroclinic*.

To deal with this situation, one commonly makes the assumption that  $\Omega$  remains constant on surfaces of constant pressure, also called *isobaric* surfaces, but it may vary with depth:  $\Omega = \Omega(P)$ . Such a situation is called *shellular rotation*. The main physical argument to justify this assumption is

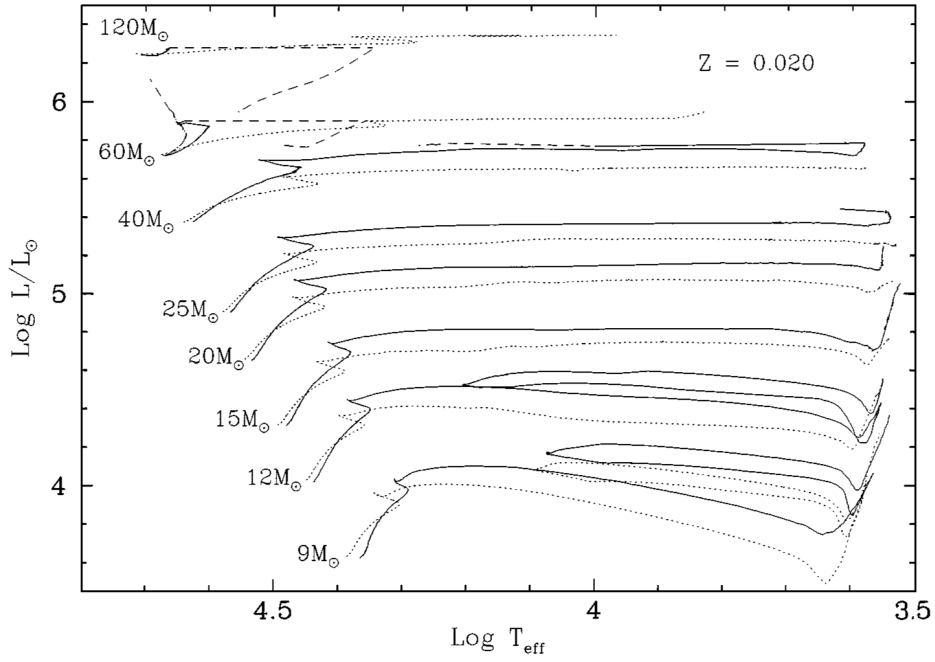


**Figure 14.6.** Evolution tracks for non-rotating stars (dotted lines) and rotating stars (solid lines) with an initial equatorial rotation velocity  $v_{\text{eq}} = 300 \text{ km/s}$ . The dashed parts of the rotating models indicate the beginning of the Wolf-Rayet phase. Figure from Maeder & Meynet (2000).

that the baroclinic condition induces strong turbulent motions in the horizontal direction (i.e. in a plane with constant pressure). These are expected to rapidly quench any substantial deviations from uniform rotation on isobaric surfaces. One then redefines the radial coordinate  $r$  as the radius of a sphere with the volume enclosed by an isobaric surface, and the mass coordinate  $m$  as the mass contained in this volume. Physical quantities such as density, temperature, and the effective gravitational acceleration are taken as the appropriate averages over an isobaric surface, and correction factors are applied to the stellar structure equations to account for the deformation of these isobaric surfaces. In that way, a set of stellar structure equations very similar in form to eqs. (7.1–7.4) is regained. To this set is added a differential equation that describes the changes in  $\Omega$  as a function of time and mass coordinate, taking into account angular momentum transport by meridional circulation and hydrodynamical instabilities (see e.g. MAEDER for details).

Especially in the case of massive stars ( $\gtrsim 10 M_{\odot}$ ) the rotation rate has a substantial effect on the evolution tracks calculated in this way. To a large extent this is the result of rotationally induced mixing processes (see below), which are expected to be more effective in more massive stars. The evolution of a single star then depends on its initial rotation rate  $\Omega$ , as well on its initial mass  $M$  and metallicity  $Z$ .

### Rotationally induced mixing

An important motivation for including the effects of rotation in stellar evolution models was the discovery that the abundances of certain elements, notably nitrogen and helium, are enhanced at the surface of massive main-sequence stars. These elements are produced in the CNO cycle, and additional mixing induced by rotation is one way to account for their presence at the stellar surface. The same processes that transport angular momentum, in particular meridional circulations and the shear instability, can also induce mixing in radiative regions of the star. However, the speed of such

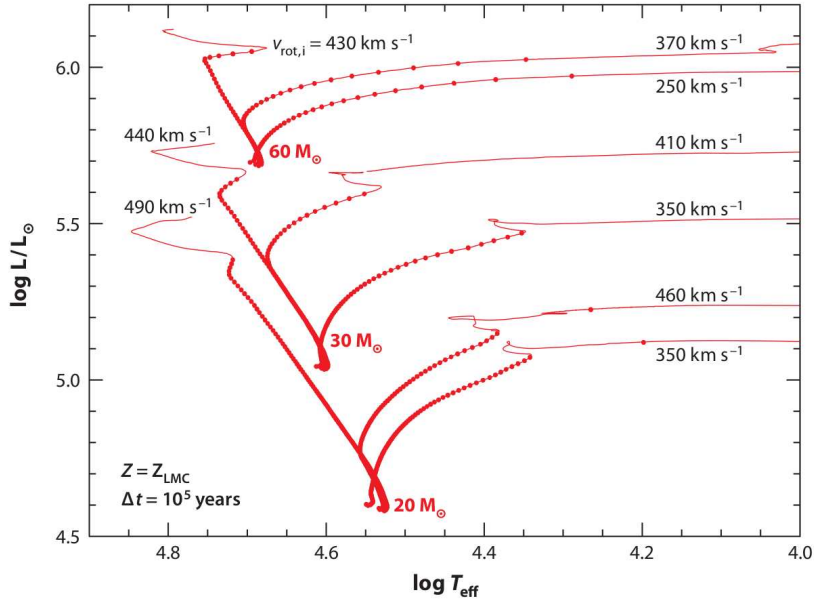


**Figure 14.7.** Evolution tracks for rotating stars with the metallicity of the Large Magellanic Cloud, for three different initial masses and initial rotation velocities. For large rotation velocities, rotational mixing is so strong that the stars evolve with almost homogeneous composition and evolve to higher  $T_{\text{eff}}$  during central hydrogen burning. Figure from Langer (2012).

mixing is quite uncertain. In the case of meridional circulation, our estimate (14.20) of the circulation timescale would lead to the conclusion that massive stars that rotate even at moderate speeds should be completely mixed within their main-sequence lifetime. This is not observed, and the actual speed of mixing by meridional circulation is reduced by a large factor, probably by the action of horizontal turbulence mentioned above. Another important uncertainty lies in the role of composition gradients, sometimes called ‘ $\mu$  barriers’. As a star evolves, nuclear burning in the core produces a gradient of the mean molecular weight  $\mu$  that decreases outwards. Similar to the case of convection (Sec. 5.5), such a  $\mu$  gradient generally stabilizes the star against mixing because rising material becomes heavier than its surroundings. As a result, the timescale of mixing is increased by an uncertain factor, which is usually treated as a free parameter in stellar evolution calculations and is adjusted to match the observations.

### Effects of rotation on stellar evolution

Fig. 14.6 compares the evolution tracks of a set of non-rotating massive-star models (similar to those discussed in Chapter 12) to rotating stellar models with an initial equatorial rotation velocity  $v_{\text{eq}} = 300 \text{ km/s}$ , which corresponds roughly to  $\Omega \approx 0.5\Omega_{\text{cr}}$  on the zero-age main sequence. The first noticeable difference occurs on the zero-age main sequence, where the rotating models have lower effective temperatures. In fact, the ZAMS luminosity is also smaller by a few percent, but this is not noticeable on the scale of the figure. These differences are purely the result of the changes in structure discussed in Sec. 14.3. Because of gravity darkening  $T_{\text{eff}}$  is not constant over the surface, but is higher at the poles than along the equator. The  $T_{\text{eff}}$  values shown in Fig. 14.6 are average values calculated as  $T_{\text{eff}}^4 = L/\sigma S$  where  $S$  is the total surface area of the star; this value corresponds to the actual  $T_{\text{eff}}$  at a latitude of about  $35^\circ$ . The non-isotropic surface flux also means that the *apparent* luminosity of the star depends on the viewing angle: if the star is viewed in the equatorial plane it appears to be fainter,

while if its is viewed pole-on it appears to be brighter, even though the actual luminosity is somewhat smaller than that of a non-rotating star.

As the star evolves along its main sequence track, the structural differences resulting from rapid rotation are gradually overwhelmed by differences that result from rotationally induced mixing. These mixing processes not only bring the products of the CNO cycle into the envelope, but also mix hydrogen from the envelope into the convective core. The changes in structure lead to a larger convective core than in a non-rotating star. In this respect, the effect of rotational mixing is similar to that of convective overshooting: the main-sequence lifetime is extended, and the star reaches a higher luminosity and lower (average) effective temperature by the end of core hydrogen burning, together producing a wider main-sequence band in the H-R diagram. These effects persist after the main sequence, where the crossing of the Hertzsprung gap and the He-burning loop both occur at larger luminosity, due to the larger He-core mass left after the main sequence. However, for the most massive stars additional differences occur, because the timescale for rotational mixing is shorter in more massive stars. The outward mixing of He lowers the opacity in the envelope, which increases the luminosity further and also makes the stars hotter and the evolution tracks bluer, thus decreasing the width of the main-sequence band for  $M \gtrsim 40 M_\odot$ .

In the most massive and most rapidly rotating stars, the timescale for rotational mixing may become shorter than the nuclear timescale. In that case, the  $\mu$  gradient that reduces the mixing efficiency may never build up and the star may be almost completely mixed while undergoing central hydrogen burning. This *quasi-homogeneous* evolution produces main-sequence tracks that are qualitatively very different from the ‘normal’ ones: rather than lowering their effective temperatures, such stars evolve to higher  $T_{\text{eff}}$  values during the main sequence. Examples of this type of evolution are shown in Fig. 14.7. The evolution towards larger  $L$  and  $T_{\text{eff}}$  of such nearly homogeneous stars can in fact be understood quite easily from the main-sequence homology relations (7.32) and (7.36). Assuming the mass to remain constant, which is not quite correct because such massive stars have strong mass loss, the luminosity and radius of chemically homogeneous stars behave as  $L \propto \mu^3$  and  $R \propto \mu^{\frac{\nu-4}{\nu+3}} \approx \mu^{0.67}$ , assuming  $\nu \approx 18$  for the CNO cycle. This results in  $T_{\text{eff}} \propto L^{0.25}/R^{0.5} \propto \mu^{0.42}$ . Thus both  $L$  and  $T_{\text{eff}}$  increase as hydrogen is transformed into helium throughout the star and  $\mu$  increases.

## 14.5 The evolution of stellar rotation rates

The angular momentum of an axially symmetric, rotating star can be written quite generally as

$$J = \int_V \rho \Omega \xi^2 dV \quad (14.21)$$

where  $\xi$  is the distance to the rotation axis, as before, and the integral is over the whole volume of the star. This is the magnitude of the angular momentum vector, which is aligned with the rotation axis. In the case of rigid rotation the constant  $\Omega$  can be taken outside the integral and we can write

$$J = I\Omega \quad \text{with} \quad I = \int_V \rho \xi^2 dV, \quad (14.22)$$

where  $I$  is the moment of inertia. For an approximately spherical star with radius  $R$  it is common to write the moment of inertia as  $I = r_g^2 MR^2$ , where  $r_g$  is the *gyration radius*, a dimensionless quantity that only depends on the relative density distribution in the star. Thus we can write

$$J = r_g^2 MR^2 \Omega. \quad (14.23)$$

A sphere with constant density has  $r_g^2 = \frac{2}{5}$ , while a polytrope with  $n = 1.5$  has  $r_g^2 = 0.2$  and an  $n = 3$  polytrope has  $r_g^2 = 0.05$ . The more centrally concentrated the star, the smaller its  $r_g$ . Typical values of  $r_g^2$  for main-sequence stars are between 0.04 and 0.1.

Let us consider what happens to the rotation rate as a star evolves. We ignore mass loss for the moment, so that the total angular momentum is conserved. Let us first consider the hypothetical case of a star that expands or contracts homologously, so that  $r_g^2$  remains constant, while maintaining rigid rotation. Then  $\Omega \propto R^{-2}$  by eq. (14.23), while eq. (14.13) shows that at the same time the critical rotation rate changes as  $\Omega_{\text{cr}} \propto R^{-3/2}$ , so that  $\Omega/\Omega_{\text{cr}} \propto R^{-1/2}$ . Thus, homologous contraction will increase  $\Omega$  faster than  $\Omega_{\text{cr}}$  and bring the star closer to break-up rotation. Conversely, homologous expansion will take the star further from critical rotation.

However, we know that stellar evolution does not proceed homologously: from the zero-age main sequence onwards, the core contracts and the envelope tends to expand. This can lead to differential rotation, as we saw in Sec. 14.3.5, unless internal torques redistribute the angular momentum efficiently such that rigid rotation is maintained. This is likely to be true at least during the main-sequence phase, so let us assume this is the case. As the star evolves across the main sequence, core contraction and envelope expansion concentrate the mass distribution towards the centre which results in a decrease of  $r_g^2$ . If we approximate this as  $r_g^2 \propto R^{-x}$ , with  $x$  a positive constant, then conservation of angular momentum leads to  $\Omega \propto R^{x-2}$  and hence  $\Omega/\Omega_{\text{cr}} \propto R^{x-0.5}$ . Thus, if  $x > 0.5$  expansion during the main sequence will bring a star *closer* to critical rotation, even though  $\Omega$  itself decreases. For stars with  $M \gtrsim 2 M_\odot$ , detailed stellar models show that  $x \approx 0.7$ . Therefore, in the absence of mass loss, such moderately massive stars will indeed show an increasing  $\Omega/\Omega_{\text{cr}}$ , although only mildly. If such a star starts with a rotation rate close to critical, it can reach and maintain this critical state during its main sequence phase. This may be the case with so-called *Be stars* or B-emission stars, which have the fastest rotation rates among B-type stars, with masses of approximately  $3\text{--}20 M_\odot$ . These stars show evidence, by their H $\alpha$  emission lines, of equatorial mass shedding in the form of transient circumstellar disks.

### 14.5.1 Angular momentum loss by stellar winds

A star that loses mass in a stellar wind must also lose angular momentum. If the stellar surface is approximately spherical and the stellar wind is isotropic (the same mass flux from each surface element), then the angular momentum carried away per unit mass equals  $\frac{2}{3}R^2\Omega$ . The rate at which angular momentum is lost from a star with mass-loss rate  $\dot{M}$  is therefore

$$\dot{J} = \frac{2}{3}\dot{M}R^2\Omega. \quad (14.24)$$

Comparing this to the angular momentum of the star, eq. (14.23), we obtain

$$\frac{\dot{J}}{J} = \frac{2}{3r_g^2} \frac{\dot{M}}{M}. \quad (14.25)$$

For main-sequence stars, the factor  $2/3r_g^2$  in eq. (14.25) has values in the range  $\approx 7\text{--}20$ . Hence, mass loss will be accompanied by such rapid angular-momentum loss that stars generally spin down as a result of their stellar wind. For main-sequence stars up to  $\approx 15 M_\odot$  winds are not strong enough to have a significant effect on their rotation rates, but significant spin-down is expected for more massive MS stars (O stars), as well as for less massive stars during later evolution phases.

The above derivation does not take into account the surface deformation of rapidly rotating stars. On the one hand, Von Zeipel's theorem predicts a higher radiative flux from the polar regions which may therefore also have higher wind mass-loss fluxes. This would reduce the angular-momentum loss compared to eq. (14.24), because these regions are closer to the rotation axis and have a smaller moment of inertia than a spherical shell. On the other hand, the reduced effective gravity near the equator may also enhance mass loss from the equator, in particular in stars that are close to break-up rotation. The mass-loss disks observed in Be star show that this can indeed take place. This effect

would increase the angular-momentum loss compared to eq. (14.24). Which of these two effects dominates is not yet clear.

### 14.5.2 Magnetic braking

Single stars of spectral type F or later ( $M \lesssim 1.5 M_{\odot}$ ) show signs of magnetic activity, such as star spots and X-ray emission. They have much smaller rotation velocities than more massive stars (Fig. 14.1) and their rotation is observed to slow down with age. This is interpreted as loss of angular momentum via their stellar winds. Even though the amount of mass lost in the wind is very small, the concurrent loss of angular momentum may be appreciable because the magnetic field of the star forces the wind matter to co-rotate to a large distance from the stellar surface.

A simple theoretical estimate of the angular-momentum loss due to magnetic braking can be made as follows. We assume the ionized wind particles are forced to move along magnetic field lines that co-rotate with the star, until they reach the *Alfven surface* where the energy density of the magnetic field equals the kinetic energy of the wind. Beyond the Alfven surface the magnetic field is too weak to force co-rotation and the wind expands freely. The angular-momentum loss rate can then be expressed analogously to eq. (14.24), but replacing the stellar radius with the radius  $R_A$  of the approximately spherical Alfven surface,

$$J = \frac{2}{3} \dot{M} R_A^2 \Omega. \quad (14.26)$$

The Alfven radius is determined by the condition

$$\rho v_w^2 = \frac{B^2}{4\pi}, \quad (14.27)$$

where  $B$  is the magnetic field strength and  $\rho$  and  $v_w$  are the wind density and velocity, which is related to the mass-loss rate by the continuity condition

$$|\dot{M}| = 4\pi r^2 \rho v_w. \quad (14.28)$$

A further assumption is that the magnetic field lines are stretched out by the outflowing wind to an almost radial configuration, which means that the field strength depends on radius as  $B \propto r^{-2}$ . Combining this with eqs. (14.27) and (14.28) then yields the dependence of the Alfven radius on the magnetic field strength at the stellar surface,  $B_0$ , and the stellar wind properties:

$$R_A^2 = \frac{B_0^2 R^4}{|\dot{M}| v_w}. \quad (14.29)$$

Keeping in mind that  $\dot{M}$  is negative, we thus find an angular-momentum loss rate of

$$J = -\frac{2}{3} \frac{B_0^2 R^4}{v_w} \Omega. \quad (14.30)$$

Surprisingly, this is independent of the mass-loss rate in this simple model, although a small amount of mass loss is of course required for magnetic braking to work.

The rate of angular momentum loss can also be derived empirically as follows. Skumanich found in 1972 that the rotation velocities of single G dwarfs decreases with age approximately as  $v_{\text{eq}} \approx 5.0(t/\text{Gyr})^{-0.5}$  km/s. Since  $J = I\dot{\Omega}$  and  $v_{\text{eq}} = \Omega R$ , one finds that this requires that  $\dot{\Omega} \propto -t^{-1.5} \propto -\Omega^3$ . Using eq. (14.23), the corresponding angular momentum loss should be

$$J = -K r_g^2 M R^4 \Omega^3, \quad (14.31)$$

where the constant  $K \approx 4 \times 10^{-29}$  (in cgs units). This gives a similar dependence of  $J$  on  $\Omega^3$  as in eq. (14.30), provided the surface magnetic field strength scales as  $B_0 \propto \Omega$ . This linear scaling is expected from stellar dynamo theory, where the magnetic field is generated by convective motions in a rotating stellar envelope, and is also roughly what is observed: faster rotating stars exhibit stronger magnetic activity.

---

## Suggestions for further reading

The contents of this chapter are covered in much greater detail by MAEDER, in particular Chapters 2, 4, 11, 12 and 27. An introduction to the structure of rotating stars is given in Chapters 41–43 of KIPPENHAHN.

---

## Exercises

### 14.1 The Roche model and gravity darkening

- (a) Show that for a uniformly rotating star in the Roche model the ratio  $R_{\text{eq}}/R_p \equiv \alpha$  is related to  $\Omega/\Omega_{\text{cr}} \equiv \omega$  as follows:

$$\frac{1}{\alpha} + \frac{4}{27} \alpha^2 \omega^2 = 1. \quad (14.32)$$

- (b) Express the ratio of effective gravities at the equator and the pole,  $g_{\text{eff},\text{eq}}/g_{\text{eff},\text{p}}$ , in terms of  $\alpha$  and  $\omega$ .
- (c) Compute the equatorial to polar temperature ratio  $T_{\text{eff},\text{eq}}/T_{\text{eff},\text{p}}$  for a radiative star with  $\omega = 0.5$  and  $\omega = 0.9$ .

## **Part II**

# **Binary Evolution**

In the next few chapters we will consider evolutionary processes that occur in binary stars. In particular we will address the following questions: (1) Which kinds of interaction processes take place in binaries, and how do these affect their evolution as compared to that of single stars? (2) How do observed types of binary systems fit into the binary evolution scenario?

# Chapter 15

## Dynamical and structural aspects of binary stars

### 15.1 Orbital dynamics

We describe the orbital motion of two stars in a binary system by approximating the stars as two point masses moving under the influence of their mutual gravity in the classical, Newtonian limit. For a full derivation of the equations given below we refer to the lectures notes of Verbunt (2013).

The relative motion of two point masses  $M_1$  and  $M_2$  at positions  $\vec{r}_1$  and  $\vec{r}_2$  can be described in terms of the vector  $\vec{r} = \vec{r}_1 - \vec{r}_2$  that connects the two masses.<sup>1</sup> The equation of motion for the relative orbit is

$$\mu \ddot{\vec{r}} = -\frac{GM_1 M_2}{r^2} \hat{\mathbf{e}}_r \quad (15.1)$$

where  $\hat{\mathbf{e}}_r$  is a vector of unit length in the direction of  $\vec{r}$ , and  $\mu$  is the *reduced mass* of the system

$$\mu = \frac{M_1 M_2}{M_1 + M_2}. \quad (15.2)$$

The angular momentum of the system, relative to its centre of mass, can be written as

$$\vec{J} = \mu \vec{r} \times \dot{\vec{r}}, \quad (15.3)$$

which is conserved because  $\ddot{\vec{r}} \parallel \vec{r}$ , so that  $\dot{\vec{J}} = \mu(\dot{\vec{r}} \times \dot{\vec{r}} + \ddot{\vec{r}} \times \vec{r}) = 0$ . The motion of the two masses is therefore in a plane perpendicular to  $\vec{J}$  and can be described by two coordinates in this plane, for which we take polar coordinates  $r$  and  $\phi$ . Therefore

$$\vec{J} = \mu r^2 \dot{\phi} (\hat{\mathbf{e}}_r \times \hat{\mathbf{e}}_\phi) \quad (15.4)$$

and the length of the angular momentum vector is

$$J = \mu r^2 \dot{\phi} \equiv \mu j, \quad (15.5)$$

where the last equality defines the angular momentum per unit reduced mass,  $j$ . The total energy of the relative orbit is the sum of the kinetic and potential energy,

$$E = \frac{1}{2} \mu \dot{\vec{r}}^2 - \frac{GM_1 M_2}{r}, \quad (15.6)$$

---

<sup>1</sup>Note that here  $\vec{r}$  has a different meaning than in previous chapters, where the symbol referred to a general position vector relative to the center of mass. In this chapter we will write this general position vector as  $\vec{s}$ .

which is also conserved (this follows from taking the time derivative and comparing to eq. 15.1). We can write the total energy as

$$E = \mu \left[ \frac{1}{2}(\dot{r}^2 + r^2\dot{\phi}^2) - \frac{G(M_1 + M_2)}{r} \right] \equiv \mu\epsilon, \quad (15.7)$$

where  $\epsilon$  is the orbital energy per unit reduced mass.

Both  $J$  and  $E$ , or  $j$  and  $\epsilon$ , are constants of motion. The general solutions of eqs. (15.5) and (15.7) in terms of  $r$  and  $\phi$  are conic sections. If  $E < 0$  the orbit is bound and described by an ellipse (Kepler's first law), characterised by the semi-major axis  $a$  and the eccentricity  $e$ :

$$r = \frac{a(1 - e^2)}{1 + e \cos(\phi - \phi_0)}. \quad (15.8)$$

The angle  $\phi_0$  corresponds to the distance of shortest approach, called periastron, while the longest distance, called apastron, is reached at  $\phi_0 + \pi$ . They are located at, respectively,

$$r_p = a(1 - e) \quad \text{and} \quad r_a = a(1 + e). \quad (15.9)$$

The angular momentum and energy per unit reduced mass for elliptic motion are

$$j^2 = G(M_1 + M_2)a(1 - e^2) \quad \text{and} \quad \epsilon = -\frac{G(M_1 + M_2)}{2a}. \quad (15.10)$$

Eq. (15.8) describes the shape of the orbit, but not the time-dependence of  $r$  and  $\phi$ . The time-dependent motion follows from Kepler's second law, which states that the vector  $\vec{r}$  sweeps out equal areas in equal times. This is a direct result of the conservation of angular momentum: by eq. (15.3), the area covered per unit time is

$$\frac{dA}{dt} = \frac{1}{2}|\vec{r} \times \dot{\vec{r}}| = \frac{J}{2\mu} = \text{constant}. \quad (15.11)$$

This can be used to derive an equation for  $\phi(t)$ , known as Kepler's equation, but this is somewhat convoluted and we will not use this in the remainder of these lecture notes. However, it follows immediately from Kepler's second law that the relative velocity  $v^2 = \dot{r}^2 + r^2\dot{\phi}^2$  must be largest at periastron and smallest at apastron. The combination of eqs. (15.7) and (15.10) gives

$$v^2 = G(M_1 + M_2) \left( \frac{2}{r} - \frac{1}{a} \right). \quad (15.12)$$

Useful expressions for the velocities  $v_p$  and  $v_a$  at periastron and apastron are

$$v_p^2 = \frac{G(M_1 + M_2)}{a} \frac{1+e}{1-e} \quad \text{and} \quad v_a^2 = \frac{G(M_1 + M_2)}{a} \frac{1-e}{1+e}. \quad (15.13)$$

A full ellipse is covered during a time interval  $P$ , the orbital period. From Kepler's second law and eq. (15.10) it follows that the orbital period is related to the semi-major axis and the total mass of the binary,

$$\left( \frac{2\pi}{P} \right)^2 = \frac{G(M_1 + M_2)}{a^3}, \quad (15.14)$$

which constitutes Kepler's third law.

The case  $e = 0$  describes a circular orbit. For a given angular momentum, this is the situation with the smallest possible orbital energy, as can be seen by analysing eqs. (15.10). In this case the separation and orbital velocity are constant in time, and the angular velocity is simply  $\dot{\phi} = 2\pi/P$ .

### 15.1.1 Perturbations to Keplerian orbits

In practice, binary orbits often deviate slightly from the Keplerian motion described above. This can be the result of a number of different processes:

- Real stars in binary systems are not point masses but have a finite extent, and as a result their structure is modified by their mutual gravity and by rotation. Under certain circumstances the resulting distortion can be conveniently described by the Roche model, see Sect. 15.2. Because a distorted star has a quadrupole moment, its gravitational field is not exactly that of a point mass. This can lead to *apsidal motion*: the slow rotation of the semi-major axis around the rotation axis of the binary. Apsidal motion is commonly observed among eccentric, short-period binaries – for example in eclipsing binaries, where it shows up as a periodic variation in the orbital phase at which eclipses are observed. The rate of apsidal motion can be measured and used to test models of the internal stellar structure.

Less commonly, the rotation axis of one or both stars can be oblique to the orbital axis. In that case the distortion can lead to *precession* of both the spin axes and the orbital axis.

- General relativity (GR) modifies the Newtonian inverse-square law of gravity. Therefore GR also results in apsidal motion, and it must be taken into account when performing the tests mentioned above. Somewhat counter-intuitively, the apsidal motion due to GR drops off much more slowly with increasing orbital period than that due to structural distortion, and dominates in binaries with periods larger than about 10 days.
- A third body orbiting the binary can cause both precession and apsidal motion, even if it orbits at a rather large distance. In addition, if the orbit of the outer body is sufficiently inclined it can induce periodic fluctuations in the eccentricity and the inclination, known as Kozai cycles. Because a non-negligible fraction of stars occur in triple or higher-order multiple systems, these processes can occur in a considerable number of systems.

The above processes either do not change the shape of the orbit or, in the case of Kozai cycles, do so only in a cyclic way. In addition, there are a number of processes that produce long-lasting orbital changes, thereby affecting the evolution of the binary. These include, among others: gravitational wave radiation, another consequence of GR, which leads to loss of orbital angular momentum and energy; tidal friction, i.e. the dissipation of energy raised by tides from the companion star; mass loss from one or both stars; and mass transfer between the stars. We shall treat these *evolutionary processes* in some detail in future chapters.

## 15.2 Roche geometry

The shape of a star is no longer spherical when it feels the gravitational attraction of a companion star. The structure of stars in close binary systems and their interaction are often described in terms of the *Roche model*, an extension of the model we used in Sec. 14.3 to describe rotating stars.

### 15.2.1 The Roche potential

In the Roche model, the gravitational field of each star is approximated by that of a point mass, as if all the mass of the star were concentrated at its centre. The stars are assumed to be in a circular orbit, so that their separation is constant in time and equal to  $a$ . Then the angular velocity of the system is equal to  $\omega = 2\pi/P$  and is related to the stellar masses and the separation by Kepler's law (15.14). In a

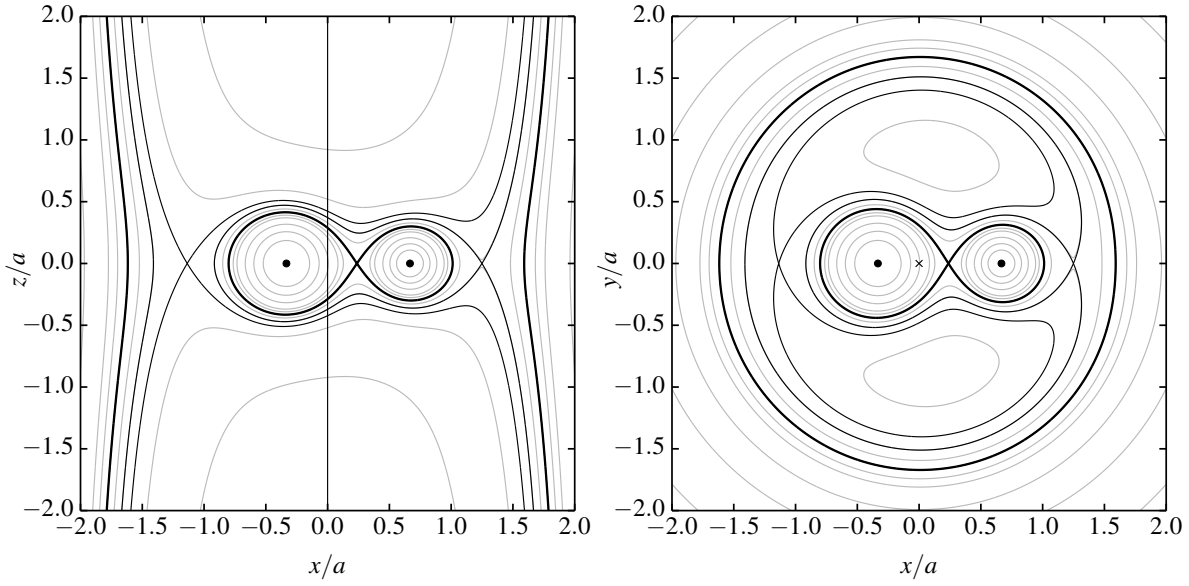


**Figure 15.1.** Equipotential surfaces of the Roche potential for a binary with mass ratio  $M_2/M_1 = 0.5$ , in the plane perpendicular to the orbit (*left*) and in the orbital plane (*right*). The critical surface defining the Roche lobes is shown as a thick solid line, the surfaces passing through  $L_2$  and  $L_3$  are thinner solid line. Several other equipotential surfaces are shown as thin gray lines. The rotation axis of the binary is shown as a vertical line (*left*), the centre of mass as a cross (*right*).

frame that co-rotates with the binary, a stationary free particle feels an effective acceleration that can be derived from a potential,

$$\vec{g}_{\text{eff}} = -\vec{\nabla}\Phi, \quad (15.15)$$

where  $\Phi$  is the combined gravitational and centrifugal potential of the binary, known as the *Roche potential*. If  $\vec{s}$  is a position vector with its origin in the centre of mass of the binary, then

$$\Phi(\vec{s}) = -\frac{GM_1}{|\vec{s} - \vec{r}_1|} - \frac{GM_2}{|\vec{s} - \vec{r}_2|} - \frac{1}{2}\omega^2\xi^2 \quad (15.16)$$

where  $\vec{r}_1$  and  $\vec{r}_2$  point to the centres of the stars, with masses  $M_1$  and  $M_2$ , respectively, and  $\xi$  is the distance of position  $\vec{s}$  to the orbital axis of the binary. When we write eq. (15.16) in dimensionless units (mass in units of the total mass  $M_1 + M_2$  and distance in units of the semi-major axis  $a$ ), we see that the shape of surfaces of constant  $\Phi$  depends only on the mass ratio  $M_2/M_1$ .

Figure 15.1 shows several such equipotential surfaces for a binary with a mass ratio  $M_2/M_1 = 0.5$ . We can discriminate four types of surfaces  $\Phi = -C$ , with  $C$  a positive constant. For large  $C$ , there are two closed surfaces, one around each star. For a critical value of  $C$ , the two closed surfaces touch in the inner Lagrangian point  $L_1$ , forming a figure-of-eight shape. This critical equipotential surface encloses the so-called *Roche lobes* of the two stars.  $L_1$  is a neutral saddle point in the potential, and there are two more such neutral saddle points,  $L_2$  and  $L_3$ , further out on the line connecting the stellar centres. For values of  $C$  smaller than that of the critical Roche surface, but larger than that of  $L_2$  and  $L_3$ , we have a peanut-shaped closed surface around both stars. For even smaller values of  $C$  the surfaces become open.

When  $M_2 \rightarrow 0$  eq. (15.16) reduces to the Roche potential for a rotating star, eq. (14.11). In this limit we can see star 2 as a massless test particle orbiting with the spin angular frequency of a star

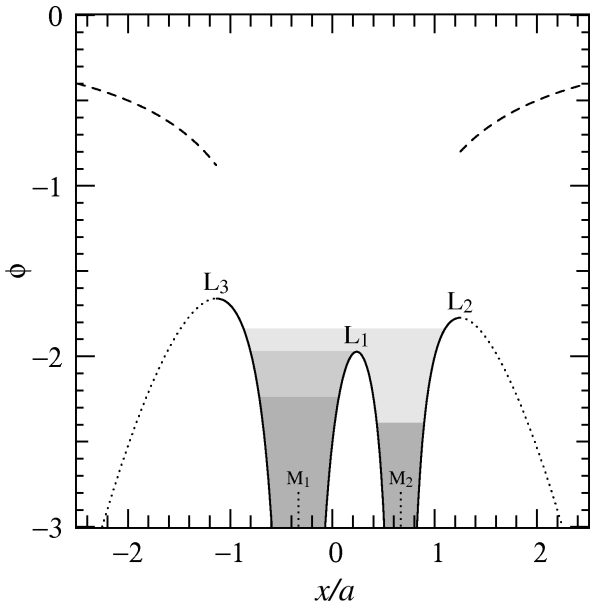


**Figure 15.2.** Shape of the Roche potential (solid line) along the line connecting the two stars, for a binary with mass ratio  $M_2/M_1 = 0.5$ . The horizontal scale is in units of the semi-major axis  $a$ , and the potential  $\phi$  is in units of  $G(M_1 + M_2)/a$ . The locations of the centres of mass of the two stars are indicated by  $M_1$  and  $M_2$ , and the Lagrangian points by  $L_1$ ,  $L_2$  and  $L_3$ . Gray scales indicate the three possible stable binary configurations: detached (dark), semi-detached (medium) and contact (light gray).

Outside  $L_2$  and  $L_3$  the Roche potential, shown with dotted lines, loses its physical meaning (see text). Here one needs to consider the gravitational potential of the binary as a whole, shown schematically with dashed lines.

with mass  $M_1$ . The surfaces through  $L_1$ ,  $L_2$  and  $L_3$  then coincide and the neutral point becomes a circle in the equatorial plane.

The volume of the Roche lobe can be calculated numerically. We can define an equivalent radius of the Roche lobe,  $R_L$ , as the radius of a sphere with the same volume,  $V_L = \frac{4}{3}\pi R_L^3$ . Because the shape of the Roche lobe depends only on the mass ratio, so does its size relative to the orbit. The following equation provides a fitting formula for the Roche radius of star 1 that is accurate to better than 1% over the entire range of mass ratios  $0 < q = M_1/M_2 < \infty$ :

$$\frac{R_{L,1}}{a} = \frac{0.49q^{2/3}}{0.6q^{2/3} + \ln(1 + q^{1/3})} \quad (15.17)$$

The Roche radius of star 2 is obtained by simply taking  $q = M_2/M_1$ . We will often use a somewhat less accurate but simpler fitting formula that is valid for  $0.1 < q < 10$ :

$$\frac{R_{L,1}}{a} \approx 0.44 \frac{q^{0.33}}{(1 + q)^{0.2}} \quad (15.18)$$

Both these expressions are due to P. Eggleton.

### 15.2.2 Stellar structure in the Roche geometry

The Roche potential also applies to the stellar material, provided that the stars rotate rigidly with the same angular frequency  $\omega$ . In that case hydrostatic equilibrium can be expressed by eq. (14.9),

$$\vec{\nabla}P = -\rho\vec{\nabla}\Phi. \quad (15.19)$$

with  $\Phi$  the gravitational-centrifugal potential of the binary. The same conclusions hold as for a single star in uniform rotation (Sec. 14.3.1), in particular: the pressure  $P$ , the density  $\rho$  and (for homogeneous composition) the temperature  $T$  are all constant on equipotential surfaces.

Hydrostatic equilibrium in the co-rotating frame requires that the stellar surface coincides with an equipotential surface. This allows three possible configurations in which both stars are in hydrostatic equilibrium (see Fig. 15.2), all of which are observed to occur in nature:

- In a *detached binary* each star fills an equipotential surface inside its own Roche lobe. Although the surface is distorted, especially if it lies close to the Roche lobe, the deviation from spherical symmetry is small enough that the internal structure is not strongly affected by the Roche geometry. To first order, the structure and evolution of both stars can be approximated by that of single stars.
- If one of the stars exactly fills its Roche lobe while the other is still smaller, the binary is *semi-detached*. Matter at the surface of the lobe-filling star can then move freely into the Roche lobe of the companion. This is the principle behind mass transfer by Roche-lobe overflow (see Chapter 17).
- A final possibility is where both stars fill the same equipotential surface, at a value of the potential above that of  $L_1$  but below that of the outer Lagrangian point  $L_2$ . Such a configuration is known as a *contact binary*, since it requires the stars to be in physical contact. This means that the stars can not only exchange mass, but also heat can flow between the stellar envelopes, as indeed appears to be the case in observed contact binaries.

Although stellar structure in the Roche geometry is often approximated by that of single stars, it should be kept in mind that the deviation from spherical symmetry affects the structure of binary stars in similar ways as it does in rotating stars, as discussed in Chapter 14. For example, if the star has a radiative envelope the Von Zeipel theorem (14.18) holds, which leads to gravity darkening at the stellar surface. Similarly to a single rotating star, a star that fills (or is close to filling) its Roche lobe in a binary has a lower effective temperature around its equator and especially near the inner Lagrangian point. We may also expect meridional circulations to play a role in binary stars, but because – unlike in single rotating stars – the Roche potential is not axially symmetric, these are likely to have quite complicated patterns.

### Validity of the Roche model

In the Roche model we have made three important assumptions, and it is important to reiterate them and assess their validity:

1. The gravitational fields of both stars are assumed to be those of point masses.
2. The orbit is assumed to be circular, so that the angular velocity is constant.
3. Both stars are assumed to be in rigid rotation and synchronized with the orbital motion, because the Roche geometry only applies to matter that co-rotates with the orbit.

The first assumption is not unreasonable, even when stars are quite extended, because most stars are very centrally concentrated. Nevertheless, the small deviation from spherical symmetry should be taken into account when studying processes such as apsidal motion and tidal interactions.

The last two assumptions are certainly not generally valid, as many binaries have eccentric orbits and stellar rotation rates are in general not synchronized. However, when stars are close to filling their Roche lobes, these conditions can often be satisfied because of strong *tidal interaction*. We will see in Chapter 16 that tides tend to dissipate energy until the total energy of the binary is minimized, which happens when the orbit is circular and rotation is synchronized. The timescales for circularization and synchronization become very short when a star is close to filling its Roche lobe. Whether or not these processes are completely effective, the Roche geometry can be seen as the energetically most favourable configuration that a binary can find itself in, given its total angular momentum.

When the stellar surfaces in a contact binary exceed the outer Lagrangian point  $L_2$ , hydrostatic equilibrium can no longer be maintained. If we apply the Roche geometry to matter outside  $L_2$  or  $L_3$ , we might conclude that this matter is able to ‘roll down the potential hill’ and escape to infinity by the action of the centrifugal force (see Fig. 15.2). However, this is incorrect because gas located outside  $L_2$  or  $L_3$  cannot maintain co-rotation with the orbit, and the Roche potential loses its physical meaning. Such matter is still bound to the system, as indicated by the dashed lines in Fig. 15.2 that represent the gravitational potential of the binary at large distance.

### 15.2.3 Implications for binary evolution and mass transfer

Binaries usually start out in a detached configuration. As a result of evolution, i.e. expansion due to nuclear evolution of the stars, possibly combined with orbital shrinking owing to angular momentum loss,  $R_1/R_{L,1}$  and  $R_2/R_{L,2}$  increase with time. A detached binary can thus evolve into a semi-detached binary or, if both stars fill their Roche lobes, into a contact binary.

We briefly recall some results from Part I of these notes, on single-star evolution (Chapters 9–12). Fig. 15.3a shows evolution tracks in the Hertzsprung-Russell diagram for stars with masses between 1.0 and  $25 M_\odot$ , together with lines of constant radius. For three masses (representing low-mass stars, intermediate-mass stars and massive stars, respectively) the corresponding variation of the stellar radius with time is depicted in Fig. 15.3b-d. During the main sequence (central hydrogen burning) phase all stars show a mild increase in radius. Low-mass stars (e.g. the  $1.6 M_\odot$  star) subsequently expand strongly but relatively slowly – on the nuclear timescale of hydrogen-shell burning – during the ascent of the first giant branch, where they develop degenerate helium cores that grow in mass until the occurrence of the helium flash when the core mass  $M_c \approx 0.47 M_\odot$ . In contrast, intermediate-mass stars (e.g. the  $4 M_\odot$  star) expand much more rapidly – on a thermal timescale – as they cross the Hertzsprung gap, before they ignite helium non-degenerately. During helium burning low- and intermediate-mass stars describe a loop in the H-R diagram, and their radius remains smaller than it was at the tip of the giant branch. After helium exhaustion in the centre the radius increases again on the asymptotic giant branch, where such stars develop degenerate carbon-oxygen cores. Massive stars (e.g. the  $16 M_\odot$  star) expand more strongly as they cross the Hertzsprung gap and, at least up to about  $25 M_\odot$ , burn helium as a red supergiant while their radius keeps expanding slightly. Even more massive stars experience such strong mass loss that their hydrogen-rich envelope is removed by the time helium ignites; their radius decreases and they become Wolf-Rayet stars.

Based on the variation of the stellar radius with time, three cases of mass transfer can be distinguished. An evolving star in a binary can fill its Roche lobe for the first time:

- as it expands on the main sequence (Case A),
- as it expands after hydrogen exhaustion but before helium ignition (Case B),
- or as it expands after helium exhaustion (Case C).<sup>2</sup>

This is depicted in Fig. 15.3b-d for three different masses. Which of the three cases applies depends on the size of the Roche lobe, which in turn depends on the separation between the two stars and (to a lesser extent) on the mass ratio (see eq. 15.17 or 15.18).

The distinction between cases A, B and C contains information about the evolution state of the remnant of the donor after mass transfer. Just as important, however, is a distinction based on the stability of mass transfer. This depends crucially on whether the donor has a radiative or a convective

---

<sup>2</sup>Unlike for low- and intermediate-mass stars, in massive stars central helium burning can occur at larger radii than helium ignition, e.g. see Fig. 15.3d. Mass transfer that starts during this phase is intermediate between cases B and C, and is sometimes designated as ‘Case BC’.

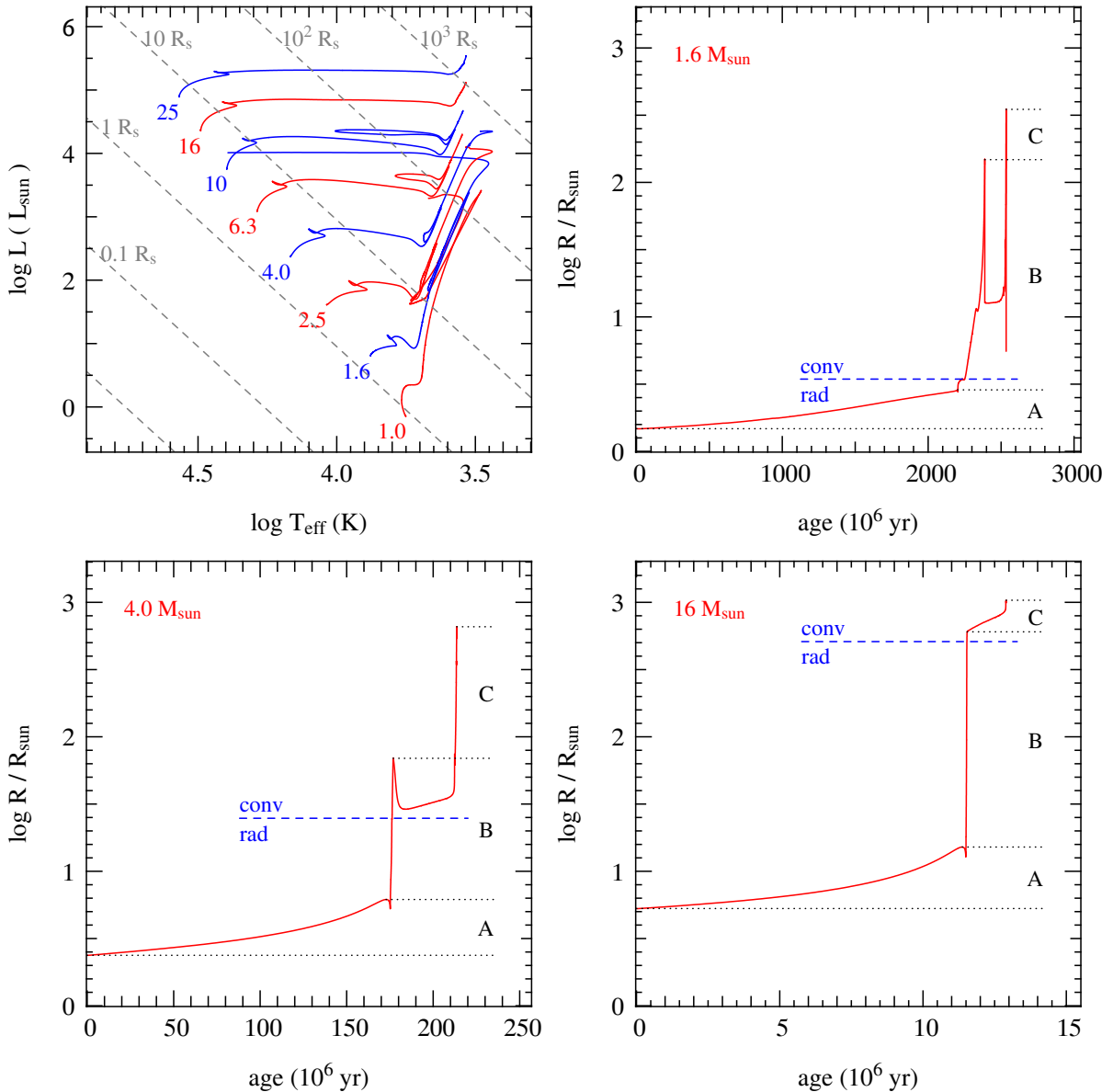


**Figure 15.3.** Evolution in the H-R diagram (panel a) of single stars with masses between  $1.0$  and  $25 M_{\odot}$ , as indicated, together with lines of constant radii (in solar radii, dashed lines). The other panels show the variation of the radii of stars of (b)  $1.6 M_{\odot}$ , (c)  $4 M_{\odot}$  and (d)  $16 M_{\odot}$  between the ZAMS and either the end of the AGB ( $1.6$  and  $4 M_{\odot}$ ) or carbon burning ( $16 M_{\odot}$ ). The models have been calculated for a metallicity  $Z = 0.02$  and a moderate amount of overshooting. The dotted lines indicate the radii at the ZAMS, the end of the MS, the ignition of He, and the maximum radius. The dashed blue line shows the radius at which the stars develop a deep convective envelope on the giant branch.

envelope, as will be discussed in Sect. 17.3. The radius at which stars reach the red giant branch and develop a deep convective envelope is also indicated in Fig. 15.3.

### Core mass-radius relation for low-mass giants

Low-mass stars ( $\lesssim 2 M_{\odot}$ ) on the first giant branch have degenerate helium cores and their luminosity is generated entirely by hydrogen-shell burning around the growing core. The envelope is so extended

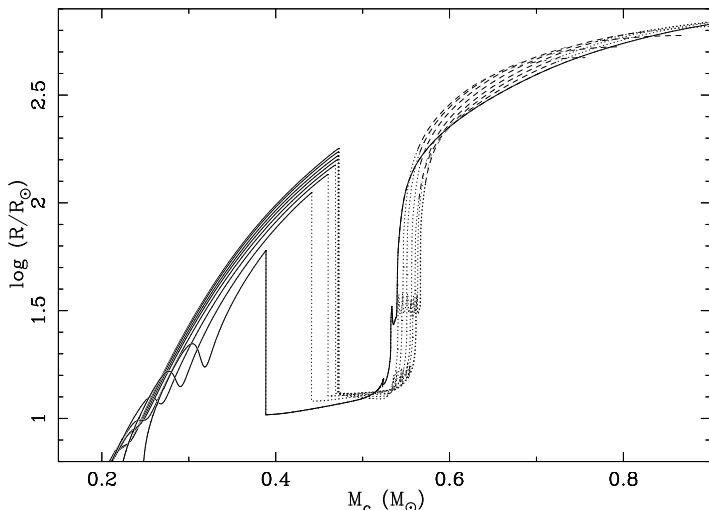


**Figure 15.4.** Core mass-radius relations for low-mass stars, from detailed stellar models with masses between  $0.9$  and  $2.0 M_{\odot}$  computed by van der Sluys et al. (2006). The solid lines correspond to the first giant branch when these stars have a degenerate helium core. The dashed lines show the asymptotic giant branch, with a degenerate carbon-oxygen core. The dotted lines correspond to the core helium-burning phase, when the stellar radius is smaller than the maximum reached on the first giant branch, and during which time such stars cannot fill their Roche lobes.

that it exerts negligible pressure on the dense core, and the luminosity depends only on the mass of the core: low-mass giants follow a very tight core-mass luminosity relation (see Sec. 10.2.2). These stars have deep convective envelopes and are forced to evolve along a Hayashi line at almost constant effective temperature, which only weakly depends on the mass of the star. Hence there is also a fairly tight core-mass radius relation, as depicted in Fig. 15.4. This relation plays an important role in the evolution of low-mass binaries with compact objects, as we shall see in later chapters.

The core-mass radius relation breaks down for masses  $\gtrsim 2 M_{\odot}$  (the highest mass indicated in Fig. 15.4, as a solid line) and for core masses  $\gtrsim 0.47 M_{\odot}$  when the radius shrinks in response to helium burning. However, for  $M_c \gtrsim 0.6 M_{\odot}$  low-mass stars again follow a core mass-radius relation on the asymptotic giant branch.

## Exercises

### 15.1 Kepler's laws

Start from Kepler's second law (15.11) to derive his third law (15.14). [Hint: use the fact that the *semi-minor axis* of an ellipse equals  $b = a(1 - e^2)^{1/2}$ .]

### 15.2 Roche geometry

- Rewrite eq. (15.16) in dimensionless units, by writing all distances in units of semi-major axis  $a$  and all masses in units of  $M_1 + M_2$ , and show that the shape of the Roche surfaces depends only on the mass ratio  $M_1/M_2$ .
- At the inner Lagrangian point, the net force is zero. Write down the equation for this. Write the distance of the inner Lagrangian point to the stellar centres and to the orbital rotation axis in terms of  $a$ . Finally, make the equation dimensionless, in the form  $\mathcal{F}(r/a) = 0$ .
- Note: we can use the Newton-Raphson method on the dimensionless equation of (b) to solve for the inner Lagrangian point. Knowing its position we can calculate its potential  $\Phi_L$ , the potential of the Roche surface. We can derive similar equations as in (b) for the second and third Lagrangian points.

### 15.3 Roche radii

Show that the ratio of the Roche-lobe radii of binary components is given approximately by

$$\frac{R_{L,1}}{R_{L,2}} \approx q^{0.46} \quad (15.20)$$

for  $q = M_1/M_2$  lying between 0.1 and 10.

#### 15.4 Orbital period and mean density

For semi-detached binaries there is a relation between the orbital period and the average density of the Roche-lobe filling component, as follows:

$$P = F \left( \frac{\bar{\rho}}{\bar{\rho}_\odot} \right)^{-1/2} \quad \text{with} \quad F \approx 0.35 \text{ d} \left( \frac{2}{1+q} \right)^{0.2}, \quad (15.21)$$

where  $F$  only depends very weakly on the mass ratio, and can be considered a constant (0.35 d) for practical purposes.

- (a) Derive this relation.
- (b) Certain ‘ultra-compact’ binaries have orbital periods of less than 20 minutes. Compare their average density to that of:
  - normal main-sequence (MS) stars,
  - low-mass helium MS stars, entirely composed of helium, which follow a mass-radius relation  $R/R_\odot \approx 0.2(M/M_\odot)$  and have a mass of at least  $0.3 M_\odot$ , the minimum mass for helium burning.
- (c) What can you conclude about the evolution state of the mass donor in such ultra-compact systems?

#### 15.5 Cases of mass transfer

Fig. 15.3c shows how the radius of a star of  $4 M_\odot$  changes during its evolution. Assume such a star has a binary companion of  $3 M_\odot$ . Use this plot to calculate:

- (a) for which range of orbital periods does mass transfer occur according to case A, case B or case C (determine the transition radii as accurately as possible);
- (b) for which orbital periods does the donor star have a radiative envelope.

# Chapter 16

## Tidal interaction

Tidal interaction is the main physical process that causes secular changes to the orbits of detached close binary systems. The differential gravitational field of the companion star causes a deformation of the stellar surface layers, which typically gives the star a somewhat elongated shape, in the form of two tidal bulges. In general, the orbit may be eccentric ( $e > 0$ ), the rotation frequencies of either star  $\Omega_{1,2}$  may be different from the mean angular speed of the orbit  $\omega = 2\pi/P$ , and the stellar rotation axes may be misaligned with the binary axis. In all of these circumstances, the tidal distortions on the stellar surface are time-dependent, either in amplitude (due to the varying distance in eccentric orbits) or in position on the surface with respect to the frame of rotation of the star. These time-dependent changes are not completely adiabatic: *tidal friction* causes dissipation of the kinetic energy raised by the tides, converting it into heat. Tidal friction thus decreases the total mechanical energy of the binary, while conserving the total angular momentum. However, angular momentum can be exchanged between the orbit and the stellar spins by the dissipative tidal forces, which is why tidal interaction is also known as *spin-orbit coupling*. The coupling results from a torque caused by the misalignment of the tidal bulges with the line connecting the stellar centres, if the rotation is not synchronized with the orbit.

The total angular momentum  $\vec{J}$  of a binary can be written as the sum of orbital angular momentum and spin angular momentum of the two stars. The orbital angular momentum follows from (15.5) and (15.10), and the rotational angular momentum can be written as  $\vec{J}_{\text{rot}} = I\vec{\Omega}$ , where  $I$  is the moment of inertia of the star. If we ignore the possibility of misalignment, we need to consider only the magnitude of  $\vec{J}$ ,

$$J = M_1 M_2 \sqrt{\frac{G a (1 - e^2)}{M_1 + M_2}} + I_1 \Omega_1 + I_2 \Omega_2. \quad (16.1)$$

The total energy  $E$ , considering that the kinetic energy of rotation can be written as  $E_{\text{rot}} = \frac{1}{2} I \Omega^2$ , is

$$E = -\frac{GM_1 M_2}{2a} + \frac{1}{2} I_1 \Omega_1^2 + \frac{1}{2} I_2 \Omega_2^2. \quad (16.2)$$

Tidal dissipation means that  $E$  decreases while  $J$  remains constant, until an equilibrium situation is reached when the energy is minimized.

### 16.1 Tidal equilibrium and its stability

*For details see Hut, P. (1980) A&A, 92, 167.* It is intuitively clear that in the special situation of (1) a circular orbit, (2) co-rotation of both stars with the orbit and (3) alignment of the stellar spin

vectors with the orbital angular momentum, the tidal bulges are stationary in the frame that rotates with the same angular velocity as the binary. In this situation the Roche geometry applies (Sec. 15.2) and determines the stellar shapes. Since the tidal bulges are stationary, no tidal friction occurs and we expect an equilibrium state. Hut (1980) shows on the basis of a general analysis that the minimum energy situation of a binary is reached if and only if these three conditions are fulfilled. He also demonstrates that this *tidal equilibrium* is stable only if the orbital angular momentum is larger than three times the sum of the spin angular momenta of the stars.

To clarify the latter, let us consider the restricted case where the orbit is already circular and co-planar. We only consider the rotation of one star (with mass  $M$ , moment of inertia  $I$  and spin frequency  $\Omega$ ); the companion with mass  $m$  is treated as a point mass. Then from (16.1) and (16.2) we get

$$\dot{J} = \frac{1}{2}Mm\sqrt{\frac{Ga}{M+m}}\frac{\dot{a}}{a} + I\dot{\Omega}, \quad (16.3)$$

$$\dot{E} = \frac{GMm}{2a^2}\dot{a} + I\Omega\dot{\Omega}. \quad (16.4)$$

Conservation of angular momentum means  $\dot{J} = 0$ , which we can use to express  $\dot{a}$  in terms of  $\dot{\Omega}$ :

$$\dot{a} = -\frac{2I}{\mu a \omega}\dot{\Omega}. \quad (16.5)$$

Here we have made use of Kepler's law (15.14) and  $\mu = Mm/(M+m)$  is the reduced mass (15.2). We then obtain

$$\dot{E} = I\dot{\Omega}(\Omega - \omega), \quad (16.6)$$

which relates the rate of change of  $\Omega$  to the rate at which energy is dissipated,  $\dot{E}$ . From (16.6) we immediately see that  $\dot{E} = 0$  when co-rotation ( $\Omega = \omega$ ) has been achieved. Furthermore, if  $\Omega \neq \omega$  then dissipation ( $\dot{E} < 0$ ) implies that either (1) the star spins down,  $\dot{\Omega} < 0$ , if  $\Omega > \omega$ ; or (2) the star spins up,  $\dot{\Omega} > 0$ , if  $\Omega < \omega$ .

To conclude whether this indeed leads to co-rotation, we must also consider how  $\omega$  changes in response. For example, spin-up requires transfer of orbital into spin angular momentum and thus a decrease of  $a$ , i.e. an increase of  $\omega$ . From (16.5) and Kepler's law we find

$$\dot{\omega} = \frac{3I}{\mu a^2}\dot{\Omega}. \quad (16.7)$$

Evolution towards co-rotation requires  $|\dot{\omega}| < |\dot{\Omega}|$ , and therefore  $3I < \mu a^2$ . This is the requirement for stable tidal equilibrium in co-rotation, i.e.  $3J_{\text{rot}} < J_{\text{orb}}$  when  $\Omega = \omega$ . Now consider case (2) above, where  $\omega > \Omega$ . If  $3I > \mu a^2$  then spin-up leads to such a rapid decrease of orbital angular momentum that  $\omega - \Omega$  becomes even larger, and co-rotation can never be achieved. The orbit keeps on decaying as the star spins up, until the two stars collide. This is called the *Darwin instability*, after George Darwin (1879).

## 16.2 Tidal evolution

*For details see Hut, P. (1981) A&A, 99, 126.* In order to determine the time evolution of the orbit and the stellar spins under the influence of tidal friction, we need a physical model of dissipation. This is a very complicated problem, especially when the star is forced to oscillate in response to the

time-dependent tidal forces. Various eigen modes and resonances are possible in this *dynamical tide*, which can produce a highly non-linear behaviour.

A simple description of tidal evolution is possible if we only consider the *equilibrium tide*, i.e. the stellar distortion caused by the instantaneous tidal potential, combined with a model for weak friction. Hut (1981) gives a simple and lucid analysis of this model and its effect on the evolution of the binary, and provides a good physical insight into the tidal forces.

An important result of this model is that the dissipative tidal force has a very strong dependence on the distance  $r$  between the stars:  $F_{\text{tid}} \propto r^{-7}$ . This means that the effect of tidal friction quickly becomes negligible if the orbit is moderately wide, and that in an eccentric orbit tidal friction is by far the strongest near periastron passage. By averaging the work done by the tidal force over one orbit, Hut (1981) derives evolution equations for  $a$ ,  $e$  and  $\Omega$ . Here we give the results in a simplified form, valid in the limit of small eccentricities  $e^2 \ll 1$ :

$$\dot{a} \approx -6 \frac{k}{T} q(1+q) \left(\frac{R}{a}\right)^8 a \left(1 - \frac{\Omega}{\omega}\right), \quad (16.8)$$

$$\dot{e} \approx -27 \frac{k}{T} q(1+q) \left(\frac{R}{a}\right)^8 e \left(1 - \frac{11}{18} \frac{\Omega}{\omega}\right), \quad (16.9)$$

$$\dot{\Omega} \approx 3 \frac{k}{T} \frac{q^2}{r_g^2} \left(\frac{R}{a}\right)^6 (\omega - \Omega). \quad (16.10)$$

In these equations  $q = m/M$  is the mass ratio;  $r_g^2$  is the dimensionless moment of inertia, defined by  $I = r_g^2 M R^2$ ;  $R$  is the radius of the star;  $k$  is the so-called apsidal-motion constant, a dimensionless quantity that depends on the mass distribution within the star; and  $T$  is a typical timescale for tidal dissipation. The equations show, once again, that  $a$  increases and  $\Omega$  decreases when  $\Omega > \omega$ , and vice versa. Eq. (16.9) shows that the eccentricity can increase, rather than decrease, if  $\Omega \gtrsim \frac{18}{11} \omega$ . The increase of both  $a$  and  $e$  are in fact seen in the Earth-Moon system, in which  $\Omega \approx 30\omega$ .

Most importantly, the tidal evolution equations demonstrate the very strong dependence of tidal friction on the ratio  $R/a$ . From (16.9) and (16.10) we can derive typical timescales for the synchronization of spin and orbit,

$$\tau_{\text{sync}} = \left| \frac{\Omega - \omega}{\dot{\Omega}} \right| \approx \frac{r_g^2}{3} \frac{T}{k q^2} \left(\frac{R}{a}\right)^{-6}, \quad (16.11)$$

and for orbital circularization,

$$\tau_{\text{circ}} = \left| \frac{e}{\dot{e}} \right| \approx \frac{2}{21} \frac{T}{k q(1+q)} \left(\frac{R}{a}\right)^{-8}. \quad (16.12)$$

In the latter equation we have assumed that  $\Omega = \omega$  already. This is justified by the weaker  $R/a$ -dependence of  $\tau_{\text{sync}}$  compared to  $\tau_{\text{circ}}$ : typically synchronization is achieved well before circularization, unless  $R/a$  is relatively large. If  $e$  is substantial, the binary typically first comes into a state of *pseudo-synchronization*, where  $\Omega$  is synchronized with the orbital angular speed close to periastron,  $\omega_p > \omega$ . This is because the tides are strongest near periastron passage. Circularization and full synchronization then happen on the longer timescale  $\tau_{\text{circ}}$ . All these effects are discussed in more detail by Hut (1981).

### 16.2.1 Tidal dissipation mechanisms

The timescale  $T$  appearing in the tidal evolution equations, which depends on the details of tidal dissipation, is undetermined by the simple model of Hut (1981). To determine  $T$  we need to assume a dissipation mechanism. The equilibrium tide model is expected to be a reasonable approximation for turbulent dissipation in *convective envelopes*, in which case  $T$  is related to the turnover timescale  $\tau_{\text{conv}}$  of convective eddies. This model can indeed reproduce the observed distribution of orbital periods and eccentricities (the  $e$ -log  $P$  diagram) of binaries containing red giants (Verbunt & Phinney, 1995). However, binaries with low-mass MS components, which also possess convective envelopes, appear to be circularised up to longer periods ( $\approx 10$  days) than predicted by the equilibrium tide model. These binaries have presumably already circularised during the pre-main sequence contraction phase.

For stars with radiative envelopes, such as in massive MS binaries, one needs to consider the *dynamical tide*. Dissipation then comes from radiative damping of the forced stellar oscillations, which is much less effective than turbulent dissipation. It is also a much more complex problem to treat, mostly because of the possibility of resonances between the tidal forcing frequency and the natural stellar oscillation frequencies (eigenmodes), which makes the process highly non-linear. Some existing models (e.g. Zahn, 1977) indicate an even stronger dependence on  $R/a$  than given by (16.8–16.10).

## Exercises

### 16.1 Angular momentum

- (a) Compute the total angular momentum of a binary consisting of two stars with masses  $M_{1,2}$  and radii  $R_{1,2}$ , and show that it can be separated into the angular momentum of the orbit and the angular momenta of the two stars around their own axes of rotation. Start from the general definition of angular momentum,

$$\vec{J} = \int_V \rho \vec{r} \times \vec{v} dV. \quad (16.13)$$

Assume that the stars are perfectly spherical, and save on computing by clever use of anti-symmetry. The orbital angular velocity is  $\omega$ , the angular velocities of the stars around their own axes are  $\Omega_{1,2}$ .

- (b) Consider synchronous rotation,  $\omega = \Omega_1 = \Omega_2$ , and derive the condition for which the rotation of the two stars around their own axes can be neglected.

### 16.2 Tidal equilibrium (After Counselman, C. 1973, *ApJ* 180, 307)

Two stars with masses  $M$  and  $m$ , with  $M \gg m$ , orbit one another in a circular orbit with angular velocity  $\omega$ . The star with mass  $M$  also rotates around its own axis with angular velocity  $\Omega$  and its moment of inertia is  $r_g^2 MR^2$ . We consider the orbital energy and angular momentum relative to the center of mass.

- (a) Compute the total angular momentum  $J$  and the total energy  $E$  of this binary system, expressed in  $m$ ,  $M$ ,  $\omega$  and  $\Omega$ . Make these quantities dimensionless by defining:

$$\sigma^2 \equiv \frac{GM}{R^3}; \quad \kappa \equiv \left(\frac{m}{r_g^2 M}\right)^{1/4} \left(1 + \frac{m}{M}\right)^{1/6}; \quad W \equiv \frac{\Omega}{\sigma} \kappa^{-3}; \quad N \equiv \left(\frac{\omega}{\sigma}\right)^{1/3} \kappa^{-1}$$

and show that

$$\mathcal{L} \equiv \frac{J}{r_g^2 M R^2 \kappa^3 \sigma} = W + \frac{1}{N}; \quad \mathcal{E} \equiv \frac{E}{r_g^2 M R^2 \kappa^6 \sigma^2} = \frac{1}{2}(W^2 - N^2).$$

- (b) Sketch lines of constant  $\mathcal{E}$  in the  $N$ – $W$  plane for  $\mathcal{E} = 0, 0.5, -0.5$ ; and lines of constant  $\mathcal{L}$  for  $\mathcal{L} = 0, 1, 2, -1, -2$ . Argue from this sketch that the location where a line of constant angular momentum is tangent to a line of constant energy corresponds to an extremum of energy for fixed

angular momentum. This implies that the tangent point is an equilibrium situation. Show that in such a point  $W = N^3$ , i.e.  $\Omega = \omega$  (synchronous rotation). Sketch this line in the figure as well.

- (c) Compute in the equilibrium point from (b):

$$\left( \frac{\partial \mathcal{E}}{\partial N} \right)_{\mathcal{L}=\text{const}} \quad \text{and} \quad \left( \frac{\partial^2 \mathcal{E}}{\partial N^2} \right)_{\mathcal{L}=\text{const}}$$

When is the equilibrium of synchronous rotation stable?

# Chapter 17

## Mass transfer

A binary system starts out as detached, with both stars in hydrostatic equilibrium and filling an equipotential surface inside their Roche lobes. As a result of evolution, the stars will gradually fill a larger fraction of their Roche lobes. This is usually the result of stellar expansion due to nuclear evolution (Sec. 15.2.3), but can also be owing to angular momentum losses that shrink the orbit. Because tidal interaction depends very sensitively on the ratio  $R/a$  (Ch. 16), usually both the orbital circularization timescale and the synchronization timescale become shorter than the stellar expansion timescale when  $R$  approaches  $R_L$ . One may then expect the orbit to be circular and the stars to be in co-rotation, and the Roche geometry to apply, by the time one of the stars fills its Roche lobe.

Usually the most massive star, which has the shortest nuclear timescale and evolves more rapidly than its companion, is the first to fill its Roche lobe. It then encounters a ‘hole’ in its surface equipotential near  $L_1$ . This means that hydrostatic equilibrium is no longer possible in the vicinity of the inner Lagrangian point and matter must flow through the nozzle around  $L_1$  into the Roche lobe of its companion. This is the idea behind Roche-lobe overflow. Before deriving an expression for the mass-transfer rate by Roche-lobe overflow and the consequences for the stability of mass transfer, in the first section of this chapter we study how variation of the stellar masses, either by mass transfer or mass loss from the binary, affect the evolution of the orbit.

In a binary, both stars (\*1 and \*2) can fill their Roche lobes at subsequent evolutionary stages. We use the convention where \*1 denotes the *initially* more massive star of the binary, and \*2 the originally less massive star. In this convention the initial mass ratio  $q = M_2/M_1 < 1$ . During phases of mass transfer we denote the mass-losing star, the *donor*, with subscript ‘d’ and the companion star, the *accretor*, with subscript ‘a’ (even if it turns out there is effectively very little or no accretion taking place). Hence the donor can be either \*1 or \*2, depending on the phase of evolution, but during the first mass transfer phase the donor will always be \*1.

### 17.1 Orbital evolution during mass transfer and mass loss

The orbital angular momentum  $J$  of a binary is given by (see Sec. 15.1)

$$J^2 = G \frac{M_1^2 M_2^2}{M_1 + M_2} a(1 - e^2). \quad (17.1)$$

In many situations the angular momentum stored in the rotation of the two stars is negligible compared to the orbital angular momentum (Exercise 16.1), so that to a good approximation (17.1) also represents the total angular momentum of the binary. By differentiating this expression we obtain a

general equation for orbital evolution:

$$2\frac{\dot{J}}{J} = \frac{\dot{a}}{a} + 2\frac{\dot{M}_1}{M_1} + 2\frac{\dot{M}_2}{M_2} - \frac{\dot{M}_1 + \dot{M}_2}{M_1 + M_2} - \frac{2e\dot{e}}{1 - e^2}. \quad (17.2)$$

In the case of Roche-lobe overflow in an already circularized binary, the last term is zero. The  $\dot{J}$  term represents angular momentum loss from the binary, which can be due to spontaneous processes (such as gravitational wave radiation) or it can be associated with mass loss from the binary as a whole or from the component stars. In the latter case  $\dot{J}$  is related to the  $\dot{M}$  terms.

### 17.1.1 Conservative mass transfer

We first consider *conservative mass transfer*, in which the total mass and orbital angular momentum of the binary are conserved. In that case we can set

$$\dot{J} = 0 \quad \text{and} \quad \dot{M}_a = -\dot{M}_d,$$

and (17.2) reduces to

$$\frac{\dot{a}}{a} = 2\left(\frac{M_d}{M_a} - 1\right)\frac{\dot{M}_d}{M_d}. \quad (17.3)$$

Eq. (17.3) tells us that, because  $\dot{M}_d < 0$ , the orbit shrinks ( $\dot{a} < 0$ ) as long as  $M_d > M_a$  and the orbit expands when  $M_d < M_a$ . In other words, the minimum separation for conservative mass transfer occurs when  $M_d = M_a$ . An explicit relation between the separation and the masses can be found by integrating (17.3), or more directly from (17.1) with  $e = 0$ :

$$M_d^2 M_a^2 a = \text{constant}, \quad \text{or} \quad \frac{a}{a_i} = \left(\frac{M_{d,i} M_{a,i}}{M_d M_a}\right)^2 \quad (17.4)$$

The index 'i' denotes the initial value. We can use Kepler's law to obtain similar relations between the rate of change of the orbital period  $\dot{P}$  and the rate of mass transfer  $\dot{M}_d$ , and between the period and masses directly:

$$\frac{\dot{P}}{P} = 3\left(\frac{M_d}{M_a} - 1\right)\frac{\dot{M}_d}{M_d}, \quad \text{and} \quad \frac{P}{P_i} = \left(\frac{M_{d,i} M_{a,i}}{M_d M_a}\right)^3 \quad (17.5)$$

The usefulness of the first equation is that it allows a determination of the mass transfer rate of observed semi-detached binaries, if the masses and the period derivative can be measured (and if the assumption of conservative mass transfer is valid). This is complicated by the fact that many binaries show short-term period fluctuations, while what is needed is the long-term average of the period derivative. However, for some binaries this long-term trend has been determined with reasonable accuracy.

### 17.1.2 Non-conservative mass transfer and mass loss

The assumption of conservation of total mass and angular momentum is a useful idealization, but it cannot be expected to hold in many circumstances. This is unfortunate because the situation becomes much more complicated and uncertain when mass and angular momentum loss from the binary have to be considered. Observationally there is evidence for both conservatively and non-conservatively evolving binaries, as we will discuss in a later chapter. For now we will just derive some useful expressions for orbital evolution, in which mass and angular momentum loss are simply parameterized.

These can also be applied to the situation where one or both of the stars is losing mass by a stellar wind, in the absence of mass transfer.

Suppose that only a fraction  $\beta$  of the transferred mass is accreted by the companion star, so that

$$\dot{M}_a = -\beta \dot{M}_d \quad \text{and} \quad \dot{M}_a + \dot{M}_d = (1 - \beta) \dot{M}_d.$$

We also need to specify how much angular momentum is taken away by the matter that is lost from the binary. This can be parameterized in different ways, here we will take the specific angular momentum of the ejected matter to be  $\gamma$  times the specific angular momentum of the binary, i.e.

$$j_{\text{loss}} \equiv \frac{\dot{J}}{\dot{M}_a + \dot{M}_d} = \gamma \frac{J}{M_a + M_d} \quad (17.6)$$

so that in (17.2) we can replace the  $\dot{J}$  term by

$$\frac{\dot{J}}{J} = \gamma(1 - \beta) \frac{\dot{M}_d}{M_d + M_a} \quad (17.7)$$

We can now derive an expression for the change in separation resulting from non-conservative mass transfer:

$$\frac{\dot{a}}{a} = -2 \frac{\dot{M}_d}{M_d} \left[ 1 - \beta \frac{M_d}{M_a} - (1 - \beta)(\gamma + \frac{1}{2}) \frac{M_d}{M_d + M_a} \right] \quad (17.8)$$

Note that the difficulty is in specifying  $\beta$  and  $\gamma$ , or rather, how these parameters depend on say the masses of the stars and on the details of the mass transfer process. We will address some of these problems later.

For some (still idealized) physical situations at least  $\gamma$  can be specified in terms of other quantities. Several ‘modes’ of non-conservative mass transfer can be considered:

**Fast mode or Jeans mode** If mass is lost from the donor star in the form of a fast isotropic wind, it will simply take away the specific orbital angular momentum of the donor in its relative orbit around the centre of mass, with  $a_d = a M_a / (M_d + M_a)$ . The assumption of a fast wind implies that the ejected matter does not interact with the binary system, and a further assumption is that the physical size of the star is neglected so that it is treated as a point mass. Then the specific angular momentum of the wind matter is

$$j_{\text{loss}} = a_d^2 \omega = \left( \frac{M_a}{M_d + M_a} \right)^2 \sqrt{G(M_d + M_a) a} \quad (17.9)$$

which can be verified to correspond to  $\gamma = M_a/M_d$ .

**Isotropic re-emission** Another physical situation that may arise is when mass is actually transferred to the companion by RLOF, but only part of this matter is accreted with the rest being ejected isotropically from the close vicinity of the accreting star. This can be the case when mass accretion drives an enhanced stellar wind from the accretor, or when the excess mass is ejected in the form of jets from a compact object. In that case  $j_{\text{loss}} = a_a^2 \omega$  which corresponds to  $\gamma = M_d/M_a$ .

**Circum-binary ring** The last situation, also sometimes called the ‘intermediate mode’, is when the mass that is lost is not ejected from the potential of the binary but forms a ring around the system. This may occur when a contact binary is formed and the critical potential surface corresponding to the outer Lagrangian point  $L_2$  is reached. Mass will then be lost through  $L_2$

without having enough energy to escape (see Fig. 15.2), and it may end up in a Keplerian orbit around the binary at some distance  $a_{\text{ring}}$  from the centre of mass. Then the specific angular momentum of such a ring will be

$$j_{\text{ring}} = [G(M_d + M_a) a_{\text{ring}}]^{1/2} \quad (17.10)$$

which corresponds to

$$\gamma = \frac{(M_d + M_a)^2}{M_d M_a} \sqrt{\frac{a_{\text{ring}}}{a}} \quad (17.11)$$

A more detailed description of orbital evolution according to these modes, as well as for a combination of several modes, can be found in the paper by Soberman et al. (1997, A&A, 327, 620). Beware, however, that a different notation is used in that paper.

## 17.2 The rate of mass transfer by Roche-lobe overflow

Mass flow through the inner Lagrangian point is, in its generality, a rather complicated hydrodynamical problem. In the following we will make it plausible that the rate of mass transfer through  $L_1$  depends very sensitively on the fractional radius excess of the donor,  $\Delta R/R_L = (R_d - R_L)/R_L$ . This allows a great simplification of the problem in many practical applications.

The rate of mass flow  $\dot{M}$  can be written as the product of the density  $\rho$  and the velocity  $v$  of the gas at  $L_1$ , and the cross section  $S$  of the stream,

$$\dot{M} \approx (\rho v)_{L_1} \cdot S \quad (17.12)$$

To estimate  $S$  consider the Roche potential in the plane through  $L_1$  perpendicular to the line connecting both stars, i.e. in the plane  $x = 0$ . In the vertical ( $y$ ) direction the potential has a roughly parabolic shape as follows from the Taylor expansion

$$\Delta\Phi \equiv \Phi(x, y) - \Phi(x, 0) = \left. \frac{\partial\Phi}{\partial y} \right|_{L_1} y + \frac{1}{2} \left. \frac{\partial^2\Phi}{\partial y^2} \right|_{L_1} y^2 \quad (17.13)$$

$$\approx \frac{1}{2} \omega^2 y^2 \quad (17.14)$$

The first derivative of  $\Phi$  is zero since  $(x, y) = (0, 0)$  corresponds to a saddle point in the potential. Furthermore it can be shown, from the definition of the Roche potential in combination with Kepler's law, that to within a factor of order unity  $(\partial^2\Phi/\partial y^2)|_{L_1} \approx \omega^2$  where  $\omega$  is the orbital frequency, which gives the second equation. This is interpreted as follows: the amount  $\Delta\Phi$  by which the surface potential of the donor exceeds the critical potential, is approximately  $\omega^2$  times the cross section  $y^2$  of the stream passing through  $L_1$ . By considering a point on the surface of the donor far away from  $L_1$ , where the potential is roughly spherical and dominated by the gravitational potential,  $\Phi \approx -GM_d/R_d$ , we also obtain

$$\Delta\Phi \approx \frac{GM_d}{R_d} \frac{\Delta R}{R} \quad \Rightarrow \quad S \approx y^2 \approx \frac{GM_d}{\omega^2 R_d} \frac{\Delta R}{R} \quad (17.15)$$

The product  $\rho v$  can be estimated by considering that at  $L_1$  the gas expands freely into the Roche lobe of the companion, so that the velocity is given by the local sound speed  $c_s = \sqrt{P/\rho}$ . We can

eliminate  $\rho$  by considering the equation of state, approximated by the polytropic relation<sup>1</sup>  $P = K\rho^\gamma$ . This gives  $c_s = \sqrt{K\rho^{\gamma-1}}$  and hence  $\rho \propto c_s^{2/(\gamma-1)}$ , so that

$$(\rho v)_{L_1} \propto c_s^{\frac{\gamma+1}{\gamma-1}}$$

Finally, at  $L_1$  the kinetic energy in the stream should equal the potential difference across it, i.e.  $\frac{1}{2}v^2 = \Delta\Phi$  which gives us  $c_s \approx v \propto \sqrt{\Delta R/R}$  from (17.15). With both  $\rho v$  and  $S$  now expressed in terms of  $\Delta R/R$  we arrive at a dimensional relation between  $\dot{M}$  and  $\Delta R/R$ :

$$\dot{M} \propto \left(\frac{\Delta R}{R}\right)^{\frac{3\gamma-1}{2\gamma-2}}$$

For stars with convective envelopes, i.e red giants or low-mass main-sequence stars,  $\gamma = \frac{5}{3}$  and the value of the exponent equals 3. However, any other reasonable value of  $\gamma$  also yields a strong dependence of  $\dot{M}$  on  $\Delta R/R$ .

A more detailed derivation applying Bernoulli's law to the gas flow through the nozzle around  $L_1$  yields the following equation:

$$\dot{M} = -A \frac{M_d}{P} \left(\frac{\Delta R}{R}\right)^3 \quad (17.16)$$

where  $M_d$  is the donor mass,  $P$  the orbital period and  $A$  is a numerical constant of order  $\sim 10$ . This relation implies that (1) the mass transfer rate is highly sensitive to the radius excess, with a slowly increasing  $\Delta R/R$  leading to strongly increasing  $\dot{M}$ , and (2) even a modest radius excess of say 10 % would lead to an enormous mass transfer rate and to the transfer of the entire donor mass in about a hundred orbits. In practice this means that for relatively slow, steady mass transfer, such as is observed semi-detached binaries, the donor only overfills its Roche radius by a small fraction. This can be seen by writing (17.16) as

$$\frac{\Delta R}{R} \sim \left(\frac{\dot{M}}{M} P\right)^{1/3} = \left(\frac{P}{\tau_{\dot{M}}}\right)^{1/3} \quad (17.17)$$

where  $\tau_{\dot{M}}$  is the timescale of mass transfer. For mass transfer occurring on the nuclear timescale or even on the thermal timescale of the donor this yields  $\Delta R/R_d < 0.01$ . Hence, unless mass transfer is much more rapid than the thermal timescale of the donor, it is a very good approximation to take  $R_d = R_L$ .

### 17.3 Stability of mass transfer

When Roche-lobe overflow starts, the stability of the mass transfer process and its consequences depend on (1) how the radius of the donor responds to the imposed mass loss, and (2) how the orbit (and therefore  $R_L$ ) responds to mass transfer. Once mass transfer is initiated its development and outcome also depend on (3) the response of the companion star to the mass that is being transferred to it. We defer this last issue to a later section, and for now assume the accreting star is an inert point mass and consider only the effect on the donor star.

We can derive *stability criteria* for the onset of mass transfer by considering points (1) and (2). We do this by comparing the stellar radius to the Roche radius as a function of decreasing donor mass in the  $R$ - $M$  diagram, as depicted schematically in Fig 17.1a. The diagram shows the Roche radius

---

<sup>1</sup>Beware that the polytropic index  $\gamma$  used here is different from the  $\gamma$  used in the previous section!

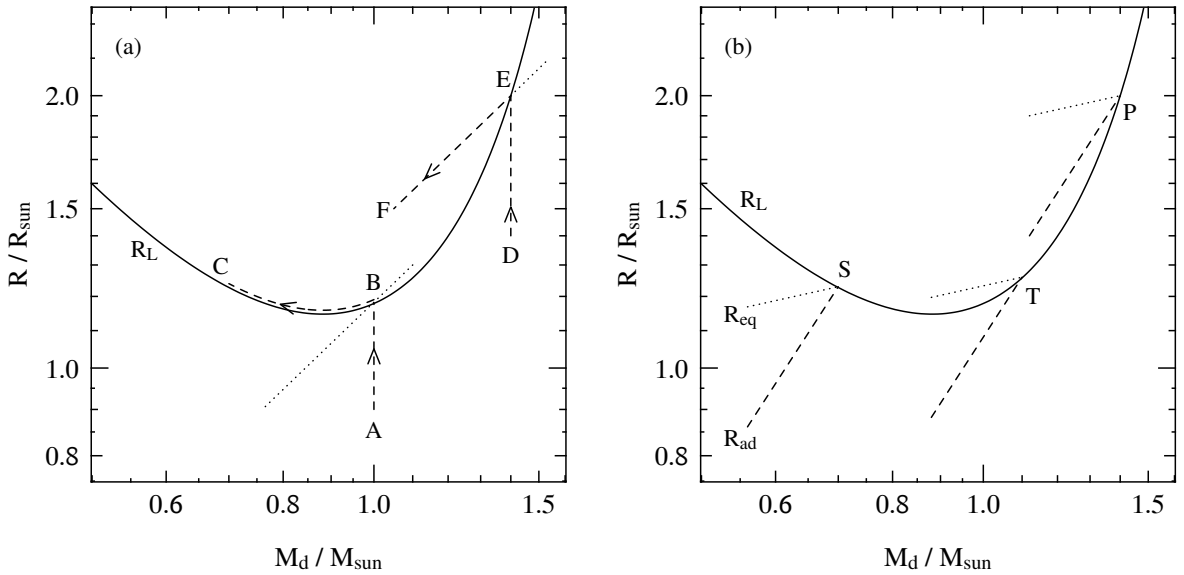


**Figure 17.1.** (a) Schematic behaviour of the Roche radius (solid line) and stellar radius (dashed lines, for two cases) as functions of the donor mass. The Roche radius curve is drawn for conservative mass transfer in a binary with total mass  $2 M_{\odot}$ . The dotted lines show a fiducial stellar mass-radius relation, for the purpose of this example taken as  $R \propto M$  (i.e.  $\zeta_* = 1$ ). See text for discussion. (b) The solid curve is the same Roche radius as in panel a, but now the dashed and dotted lines indicate schematically the adiabatic ( $R_{\text{ad}}$ ) and thermal-equilibrium ( $R_{\text{eq}}$ ) responses of the donor to mass loss, respectively (for the purpose of illustration it is assumed that  $\zeta_{\text{ad}} = 1.5$  and  $\zeta_{\text{eq}} = 0.25$ ). Mass transfer starting at S, T and P correspond to stable, thermal-timescale and dynamically unstable mass transfer respectively, as discussed in the text.

of the donor star for conservative mass transfer in a binary with total mass  $2 M_{\odot}$ , and two examples of evolution tracks, for initial donor masses  $1.0 M_{\odot}$  (starting at point A) and  $1.4 M_{\odot}$  (starting at point D). The stars evolve vertically upwards in this diagram (nuclear expansion at constant mass) until the onset of RLOF at point B and E, respectively, when  $R_d = R_L$ . Upon mass loss the donor radius may behave as given by the dotted lines through points B and E. After a small amount of mass loss,  $\delta M < 0$ , we look at the quantity  $\delta R = R_d - R_L$  and we can have either that  $R_d \leq R_L$  ( $\delta R \leq 0$ , e.g. point B in Fig 17.1a) or  $R_d > R_L$  ( $\delta R > 0$ , e.g. point E). In the first case, the donor detaches from its Roche lobe and it has to re-expand before RLOF can continue. Obviously this is the condition for stable mass transfer. In this case it is nuclear expansion that makes the donor continue to fill its Roche lobe and to drive mass transfer, and the stellar radius follows path B-C. In the second case ( $\delta R > 0$ ) the mass transfer rate – which depends very strongly on  $\delta R/R$  as shown in Sec. 17.2 – increases, leading to even more mass loss and a larger  $\delta R$  (path E-F in Fig 17.1a). This is a runaway situation, leading to unstable mass transfer. It thus appears that we have to compare the slope of the mass-radius relation, of both the stellar radius and the Roche radius. These slopes are expressed by the so-called mass-radius exponents,

$$\zeta_* \equiv \frac{d \log R_d}{d \log M}, \quad \zeta_L \equiv \frac{d \log R_L}{d \log M}, \quad (17.18)$$

where  $\zeta_* \geq \zeta_L$  implies stability and  $\zeta_* < \zeta_L$  implies instability of RLOF. The situation is complicated, however, by the fact that stars react to perturbations (like mass loss) on two very different timescales.

If a star suddenly loses mass both its hydrostatic equilibrium and its thermal equilibrium will be disturbed. The star reacts by readjusting its structure and thereby its radius in order to recover equilibrium. Since hydrostatic readjustment happens on the star's dynamical timescale, which is much

shorter than the Kelvin-Helmholtz timescale on which it readjusts thermally, the initial (dynamical) response to mass loss will be almost adiabatic. For the question of the *dynamical stability* of mass transfer we must thus consider the *adiabatic* response of the stellar radius to mass loss. This can be expressed as  $(\delta R/R)_{\text{ad}} = \zeta_{\text{ad}} \delta M/M$ , i.e. we define the adiabatic mass-radius exponent,

$$\zeta_{\text{ad}} \equiv \left( \frac{d \log R}{d \log M} \right)_{\text{ad}}. \quad (17.19)$$

The criterion for dynamical stability of mass transfer then becomes  $\zeta_{\text{ad}} \geq \zeta_L$ .

If this criterion is fulfilled, then the donor will shrink within its Roche lobe on a dynamical timescale and is able to recover hydrostatic equilibrium. In that case the slower thermal readjustment of the donor becomes relevant. On the Kelvin-Helmholtz timescale the star will attempt to recover the thermal equilibrium radius appropriate for its new mass  $M + \delta M (< M)$ , and the change in its equilibrium radius can be expressed as  $(\delta R/R)_{\text{eq}} = \zeta_{\text{eq}} \delta M/M$  or

$$\zeta_{\text{eq}} \equiv \left( \frac{d \log R}{d \log M} \right)_{\text{eq}}. \quad (17.20)$$

If, in addition to  $\zeta_{\text{ad}} \geq \zeta_L$ , also  $\zeta_{\text{eq}} \geq \zeta_L$  then the new equilibrium radius will be smaller than the Roche radius, and we have the condition for *secularly stable* mass transfer. In the intermediate case,  $\zeta_{\text{ad}} \geq \zeta_L > \zeta_{\text{eq}}$ , thermal readjustment of the donor keeps pushing it to overfill its Roche lobe. Mass transfer then occurs on the donor's thermal timescale as discussed below.

Based on the above stability considerations we can distinguish three modes of mass transfer, corresponding to different timescales, which are illustrated schematically in Fig 17.1b. (This classification is independent of the division into cases A, B and C discussed before!)

**Mode 1: stable mass transfer** if  $\zeta_L \leq \min(\zeta_{\text{ad}}, \zeta_{\text{eq}})$

This corresponds to mass transfer starting at point S in Fig 17.1b. The donor remains in thermal equilibrium, and continuing mass transfer is driven either by nuclear evolution of the donor (expansion, i.e.  $R_{\text{eq}}$  increases with time) or by orbital shrinkage due to angular momentum loss ( $R_L$  decreases). Mass transfer thus occurs on the nuclear timescale of the donor, or on the timescale for angular momentum loss, whichever is shorter.

**Mode 2: thermal-timescale mass transfer** if  $\zeta_{\text{ad}} \geq \zeta_L > \zeta_{\text{eq}}$

Mass transfer is dynamically stable, but driven by thermal readjustment of the donor. This corresponds to mass transfer starting at point T in Fig 17.1b. Initially the mass transfer rate increases, but then saturates at a value determined by the donor's thermal timescale:

$$\dot{M}_{\text{max}} \approx -M_d / \tau_{\text{KH,d}} \quad (17.21)$$

This mode is sometimes called ‘thermally unstable’ mass transfer but this is misleading: despite the thermal disequilibrium of the donor, mass transfer is stable and *self-regulating*. If  $\dot{M}$  were smaller than (17.21) the donor would be allowed to expand to regain equilibrium, leading to an increasing mass transfer rate. On the other hand if  $\dot{M}$  were much larger the donor would react almost adiabatically and shrink inside its Roche lobe. The radius excess  $\delta R/R$  adjusts itself to maintain the thermal-timescale mass loss rate. As shown in Sec. 17.2, this implies  $\delta R/R < 0.01$ . Hence also in this case, the donor radius closely follows the Roche radius, but  $R_d < R_{\text{eq}}$ .

### Mode 3: dynamically unstable mass transfer    if $\zeta_L > \zeta_{ad}$

This corresponds to mass transfer starting at point P in Fig 17.1b. The adiabatic response of the donor is unable to keep it within its Roche lobe, leading to ever-increasing mass-transfer rates. As discussed above this is an unstable, runaway situation. Detailed calculations show that mass transfer accelerates to a timescale in between the thermal and dynamical timescale of the donor. This has dramatic effects on the evolution of the binary, probably leading to a common-envelope situation (Sec. 19.2).

For these criteria to be of practical use, we need to consider how the various  $\zeta$ 's depend on the properties of the binary system and on the mass and evolution state of the donor.

#### 17.3.1 Response of the Roche radius to mass loss

The example shown in Fig 17.1 indicates that the reaction of the Roche radius depends primarily on the binary mass ratio. This can be easily shown for the case of conservative mass transfer, for which (see Exercise 17.1)

$$\zeta_L = 2.13 \frac{M_d}{M_a} - 1.67, \quad \text{for } M_d/M_a \lesssim 10. \quad (17.22)$$

The important consequence of this expression is that the stability criteria for mass transfer can be rewritten in terms of a critical mass ratio (see Sec. 17.3.3 below). However, it is important to realize that  $\zeta_L$  can take on different values for non-conservative mass transfer, i.e. it depends on the mode of mass and angular-momentum loss, as well as on the mass ratio. For a particular mode, such as those discussed in Sec. 17.1.2, the dependence of  $\zeta_L$  on mass ratio can be derived (see the article by Soberman et al., 1997).

#### 17.3.2 Response of the stellar radius to mass loss

The adiabatic response of a star to mass loss, and hence the value of  $\zeta_{ad}$ , depends critically on the structure of its envelope, in particular on whether the envelope is convective or radiative. Detailed calculations show that stars with radiative envelopes shrink rapidly in response to mass loss (i.e.  $\zeta_{ad} \gg 0$ ), while stars with convective envelopes tend to expand or keep a roughly constant radius ( $\zeta_{ad} \lesssim 0$ ).

We can make this plausible by recalling the criterion for convection to occur. If a gas element is displaced upwards adiabatically from its equilibrium position, while maintaining pressure equilibrium with its surroundings, it will experience an upward buoyancy force if its density is smaller than that of its surroundings. The envelope is then unstable to convective motions, which efficiently redistribute energy so as to make the envelope structure nearly adiabatic. This means that  $P \propto \rho^{\gamma_{ad}}$ , i.e. the density within a convective envelope falls off with pressure as  $\rho \propto P^{1/\gamma_{ad}}$ . On the other hand, if the envelope is stable against convection, the density gradient must necessarily be steeper than adiabatic in order for the buoyancy force on a displaced gas element to restore it to its original position. This means that radiative envelopes are more centrally concentrated than convective envelopes, and have relatively low density in the outer layers. When the outermost layers of a star are suddenly removed by mass loss, the layers below it are decompressed and will expand adiabatically to restore pressure equilibrium. For a convective envelope that is already adiabatically stratified, we may therefore expect that the density distribution (measured at constant pressure) will remain the same, and the star will therefore occupy about the same volume when hydrostatic equilibrium is restored. In other words,  $R_{ad}$  is insensitive to mass loss. On the other hand, the steeper initial density profile in a radiative envelope means that, first of all, the layers exposed by mass loss lie deeper within the star. After adiabatic expansion, the outer

layers will furthermore have a higher density when measured at constant pressure. Therefore when hydrostatic equilibrium is restored, a star with a radiative envelope will occupy a *smaller* volume and have a smaller radius.

This expectation is borne out by more detailed considerations. For example, polytropic stellar models with index  $n$  and constant  $K$  (constant entropy) follow a mass-radius relation  $R \propto M^{(n-1)/(n-3)}$  (Chapter 4), so that

$$\zeta_{\text{poly}} = \frac{n-1}{n-3}. \quad (17.23)$$

An  $n = 3$  polytrope, which to first order approximates a star in radiative equilibrium, thus has  $\zeta_{\text{ad}} \rightarrow \infty$ : it would shrink infinitely fast upon mass loss. Detailed models of stars with radiative envelopes show that  $\zeta_{\text{ad}} \gg 0$ , although the value is still finite;  $\zeta_{\text{ad}} \approx 4$  is a rough but reasonable approximation. On the other hand, completely convective stars behave like  $n = \frac{3}{2}$  polytropes which have  $\zeta_{\text{ad}} = -\frac{1}{3}$ ; such stars expand upon mass loss. This is relevant for low-mass main-sequence stars with  $M \lesssim 0.35 M_{\odot}$  which are completely convective, and for evolved stars on the red giant branch with deep convective envelopes. Red giants also have a dense compact core, which turns out to modify their response to mass loss; such stars can be described by so-called condensed polytropes. The response of such models to mass loss was studied by Hjellming & Webbink (1987) who found  $\zeta_{\text{ad}}$  to increase with the fractional mass of the dense core, turning positive for  $M_c > 0.2M$ ; see Fig. 1 of Soberman et al. (1997) who also provide a convenient fitting formula, eq. (60). To summarize, stars with deep convective envelopes respond to mass loss by either expanding or keeping their radius roughly constant. This has important consequences for mass transfer from red giants.

The equilibrium radius response to mass loss also depends on the evolution state of the donor, but in a different way. For homogeneous stars, i.e. stars on the zero-age main sequence,  $R_{\text{eq}}$  is simply given by their mass-radius relation. Hence for upper ZAMS stars ( $M \gtrsim 1 M_{\odot}$ ) we have  $\zeta_{\text{eq}} \approx 0.6$  and for low-mass ZAMS stars ( $M \lesssim 1 M_{\odot}$ )  $\zeta_{\text{eq}} \approx 1.0$ . However for stars that are more evolved, and have a non-homogeneous composition profile, we cannot simply apply the MS mass-radius relation. We need to consider the response on a timescale that is much slower than thermal, so that the star remains in TE, but faster than the nuclear timescale, so that the composition profile does not change. The effect of a non-homogeneous composition is to make stars expand rather than contract in response to mass loss, as is borne out by detailed calculations. Hence  $\zeta_{\text{eq}} \lesssim 0$  for fairly evolved MS stars. Detailed calculations also show that for stars in post-MS phases, the equilibrium radius is insensitive to the total stellar mass, hence  $\zeta_{\text{eq}} \approx 0$ . On the other hand, for low-mass red giants the radius depends strongly on the *core* mass, see Sec. 15.2.3.

Finally, for white dwarfs the response is again given by their mass-radius relation, i.e.  $\zeta_{\text{eq}} = -\frac{1}{3}$ . For these degenerate configurations there is no distinction between the adiabatic and thermal response.

### 17.3.3 Consequences for binary evolution

The stability criteria discussed above translate, with the use of (17.22), into critical mass ratios for the stability of (conservative) mass transfer. Since the initial mass ratio  $q = M_a/M_d < 1$ , the initial value of  $\zeta_L$  is always  $> 0.46$ . Stars with deep convective envelopes, i.e. red giants and red supergiants, have  $\zeta_{\text{ad}} \lesssim 0$ , so the first stage of mass transfer from such donors will always be dynamically unstable. Comparison with Fig 15.3 shows that Case C mass transfer is always expected to be dynamically unstable, as well as Case B mass transfer in low-mass binaries and late Case B mass transfer in intermediate-mass binaries, with RLOF starting on the first giant branch. Dynamically unstable mass transfer can only be avoided in these binaries if stellar-wind mass loss reduces the donor mass to well below the accretor mass, so that  $q \gtrsim 1.25$  when RLOF starts.

For donors with radiative envelopes, having  $\zeta_{\text{ad}} \gg 0$ , RLOF will only be dynamically unstable if the donor is much more massive than the accretor. For  $q \gtrsim 0.25$  mass transfer is dynamically stable and usually occurs on the thermal timescale, since for practically all stars  $\zeta_{\text{eq}} \lesssim 0$ . Only if the donor fills its Roche lobe very close to the ZAMS ( $\zeta_{\text{eq}} \approx 0.6 - 1.0$ ) in a very close binary with nearly equal masses, can one expect stable (nuclear-timescale) mass transfer. Therefore thermal-timescale mass transfer should occur in most Case A binaries, as well as early Case B binaries of intermediate and high mass with periods such that mass transfer occurs during the Hertzsprung-gap expansion of the donor.

## Exercises

- 17.1** Using the approximate expression (15.18) for the Roche-lobe radius of the donor, show that for conservative mass transfer the rate of change of  $R_L$  is given by

$$\frac{\dot{R}_L}{R_L} = \left( 2.13 \frac{M_d}{M_a} - 1.67 \right) \frac{\dot{M}_d}{M_d} \quad (17.24)$$

and that  $R_L$  has a minimum for  $M_d \approx 0.78 M_a$ .

- 17.2**  $\beta$  Lyrae is a semi-detached eclipsing binary in which the orbital period has been observed to change over the last 100 years. The observed ephemeris (the time of primary eclipse as a function of orbital cycle) is quite accurately fitted by a parabolic expression:

$$T_{\text{prim.eclipse}}(d) = \text{JD}2408247.966 + 12.913780 E + 3.87196 \times 10^{-6} E^2$$

where  $E$  counts the number of eclipses.

(a) Derive the orbital period of  $\beta$  Lyr and the rate of change of its orbital period.

(b) From the radial velocity variations the masses of the components have been measured as  $M_1 \sin^3 i = 12.94 \pm 0.05 M_\odot$  and  $M_2 \sin^3 i = 2.88 \pm 0.10 M_\odot$ . The inclination is not accurately measured, however. Assuming conservative mass transfer is taking place, calculate the mass transfer rate and estimate its uncertainty.

- 17.3** Show that in a binary system in which one star is losing mass in a fast, isotropic stellar wind, the separation relates to the total binary mass as

$$a(M_1 + M_2) = \text{constant} \quad (17.25)$$

if the finite dimensions of the star are ignored (i.e. it is treated as a point mass).

This result implies that if one or both stars are losing mass, the binary separation increases (inversely with total mass) even though the angular momentum decreases.

- 17.4** Derive the following expression for the mass transfer rate for stable (nuclear-timescale) mass transfer, in terms of the mass-radius exponents  $\zeta_L$  and  $\zeta_{\text{eq}}$  and the rate at which the stellar (equilibrium) radius would change in the absence of mass loss,  $(\partial R_{\text{eq}}/\partial t)_M$ :

$$\dot{M}_d = - \frac{M_d}{\zeta_{\text{eq}} - \zeta_L} \left( \frac{\partial \ln R_{\text{eq}}}{\partial t} \right)_M \quad (17.26)$$

(Hint: write  $\dot{R} = dR/dt$  in terms of the partial derivatives with respect to  $t$  and  $M$ , and use the condition that the donor star just keeps filling its Roche lobe exactly, which is accurate to  $\lesssim 0.1\%$ .)

Verify that this indeed gives reasonable mass transfer rates if the condition for stable mass transfer is fulfilled.

# Chapter 18

## Conservative binary evolution

In the previous chapter we came to the conclusion that when mass transfer starts while the donor still has a radiative envelope, i.e. it first fills its Roche lobe on the main sequence or the Hertzsprung gap (case A or early case B), and if the initial mass ratio  $M_a/M_d \gtrsim 0.25$ , then mass transfer should occur on the donor's thermal timescale. Although this can imply quite high rates of mass transfer, the process itself is self-regulating and stable. Under such circumstances it is not unreasonable to make the assumption of conservative mass transfer (Sec. 17.1.1), because the matter that is transferred through the inner Lagrangian point does not have sufficient energy to escape from the companion's Roche lobe. In this chapter we therefore consider conservative binary evolution according to case A and case B.

Whether mass transfer really is conservative depends on the response of the companion star to accretion. This constitutes a still unsolved problems in the evolution of close binaries: how much mass and angular momentum are lost from a binary system during phases of stable Roche-lobe overflow, and how does this depend on the masses and orbital parameters of the binary? We will address this question in Sec. 18.3 of this chapter.

### 18.1 Case A evolution and the Algol systems

In short-period binaries evolving according to case A, the first phase of mass transfer can usually be divided into a rapid phase on the thermal timescale of the primary, followed by a slow phase on the much longer nuclear timescale. This is illustrated in Fig. 18.1, which shows the result of a detailed evolution calculation for the primary component in a binary with initial masses  $10.0$  and  $8.9 M_{\odot}$  and an initial period  $P = 2.2$  d. The  $M$ - $R$  diagram can be compared to Fig. 17.1 in the previous chapter. The rapid phase of mass transfer, starting at point B, continues until the primary has regained thermal equilibrium, i.e. when its equilibrium radius becomes smaller than its Roche radius (point C). By this time the primary has become the less massive star in the binary, in other words the mass ratio has been reversed. Further mass transfer is driven by expansion of the primary and takes place on the nuclear timescale, until the primary has reached the end of its main-sequence phase (point D).

For the same binary, Fig. 18.2 shows the evolution of both components. The binary is detached during phase A–B. During the rapid mass-transfer phase (B–C) both stars are out of thermal equilibrium: the primary is somewhat less luminous due to mass loss, while the secondary is somewhat more luminous as a result of accretion (see Sec. 18.3). At point C both stars have regained thermal equilibrium, and phase C–D is a long-lived phase of nuclear-timescale mass transfer. The secondary has a luminosity and radius appropriate for a MS star of its increased mass, but the now less massive primary is over-luminous for its mass, and has a larger radius than the secondary.

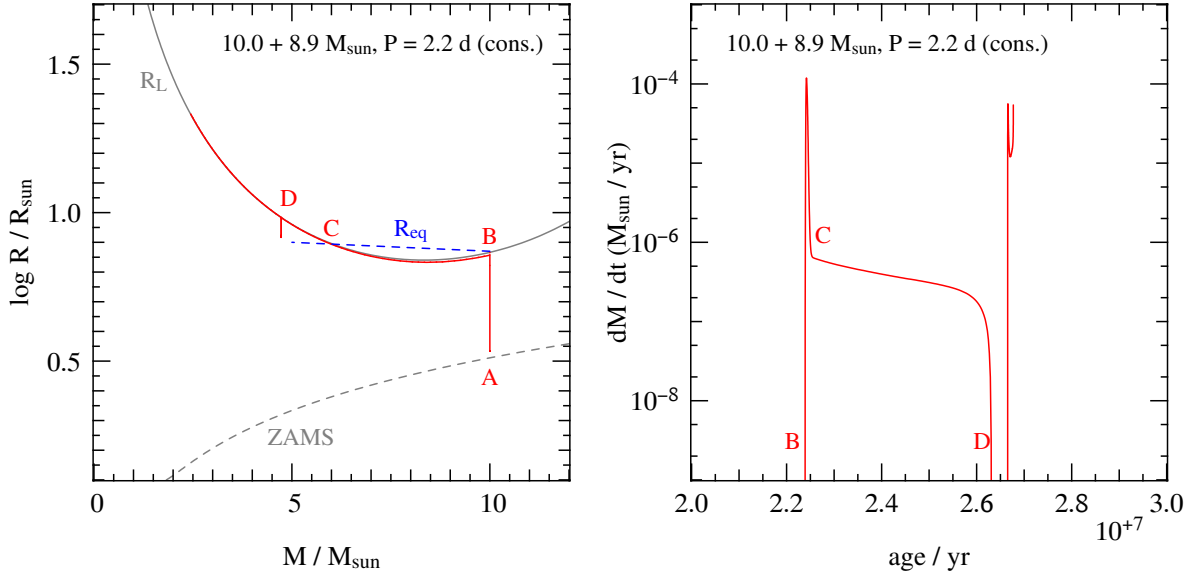


**Figure 18.1.** Mass-radius diagram of the primary star in a massive binary with initial parameters  $10.0 + 8.9 M_{\odot}$ ,  $P = 2.2$  d, with metallicity  $Z = 0.004$ . The right diagram shows the corresponding mass transfer rate as a function of time. The primary expands during its main-sequence evolution from point A to point B, when it fills its Roche lobe. The dashed line indicates the equilibrium radius, which is larger than the Roche radius between B and C. This corresponds to a phase of rapid, thermal-timescale mass transfer. At C the primary regains thermal equilibrium, and further mass transfer (C-D) is driven by expansion and takes place on the nuclear (MS) timescale. Point D corresponds to the end of the MS phase of the primary, when it detaches from its Roche lobe for a short time. During H-shell burning the primary re-expands, giving rise to further mass transfer past point D (on the much faster expansion timescale associated with crossing the Hertzsprung gap).

**Table 18.1.** Some observed Algol-type binaries. Masses, radii and luminosities are given in solar units.

| name                | spectra       | $P$ (d) | $M_1$ | $M_2$ | $R_1$ | $R_2$ | $\log L_1$ | $\log L_2$ |
|---------------------|---------------|---------|-------|-------|-------|-------|------------|------------|
| V Pup               | B2 + B1V      | 1.45    | 9     | 17    | 5.3   | 6.3   | 3.85       | 4.20       |
| TT Aur              | B6 + B3       | 1.33    | 5.4   | 8.1   | 4.2   | 3.9   | 3.21       | 3.71       |
| U Her               | B8-9 + B2V    | 2.05    | 2.9   | 7.6   | 4.4   | 5.8   | 2.49       | 3.68       |
| Z Vul               | A2III + B3V   | 2.45    | 2.3   | 5.4   | 4.5   | 4.7   | 2.07       | 3.30       |
| U CrB               | G0III + B5.5V | 3.45    | 1.46  | 4.98  | 4.94  | 2.73  | 1.43       | 2.51       |
| $\beta$ Per (Algol) | G8III + B8V   | 2.87    | 0.8   | 3.7   | 3.5   | 2.9   | 0.65       | 2.27       |
| V356 Sgr            | A2III + B4V   | 8.90    | 4.7   | 12.1  | 14    | 6     |            |            |

These properties are typical of many observed semi-detached binaries, so-called Algol-type binaries. Table 18.1 lists observed properties of several Algol-type systems. The primary (\*1) is now filling its Roche lobe and is interpreted as the originally most massive star. The secondary (\*2) is currently the more massive and more luminous star, but is often smaller in radius than the primary. Many such binaries are known, which is in accordance with the fact that the semi-detached phase of slow mass transfer lasts for the remaining main-sequence lifetime of the primary. The first group of six systems in Table 18.1 are interpreted as undergoing slow case A mass transfer. The last system is an example of a group of rarer, wider semi-detached systems that may be undergoing case B mass

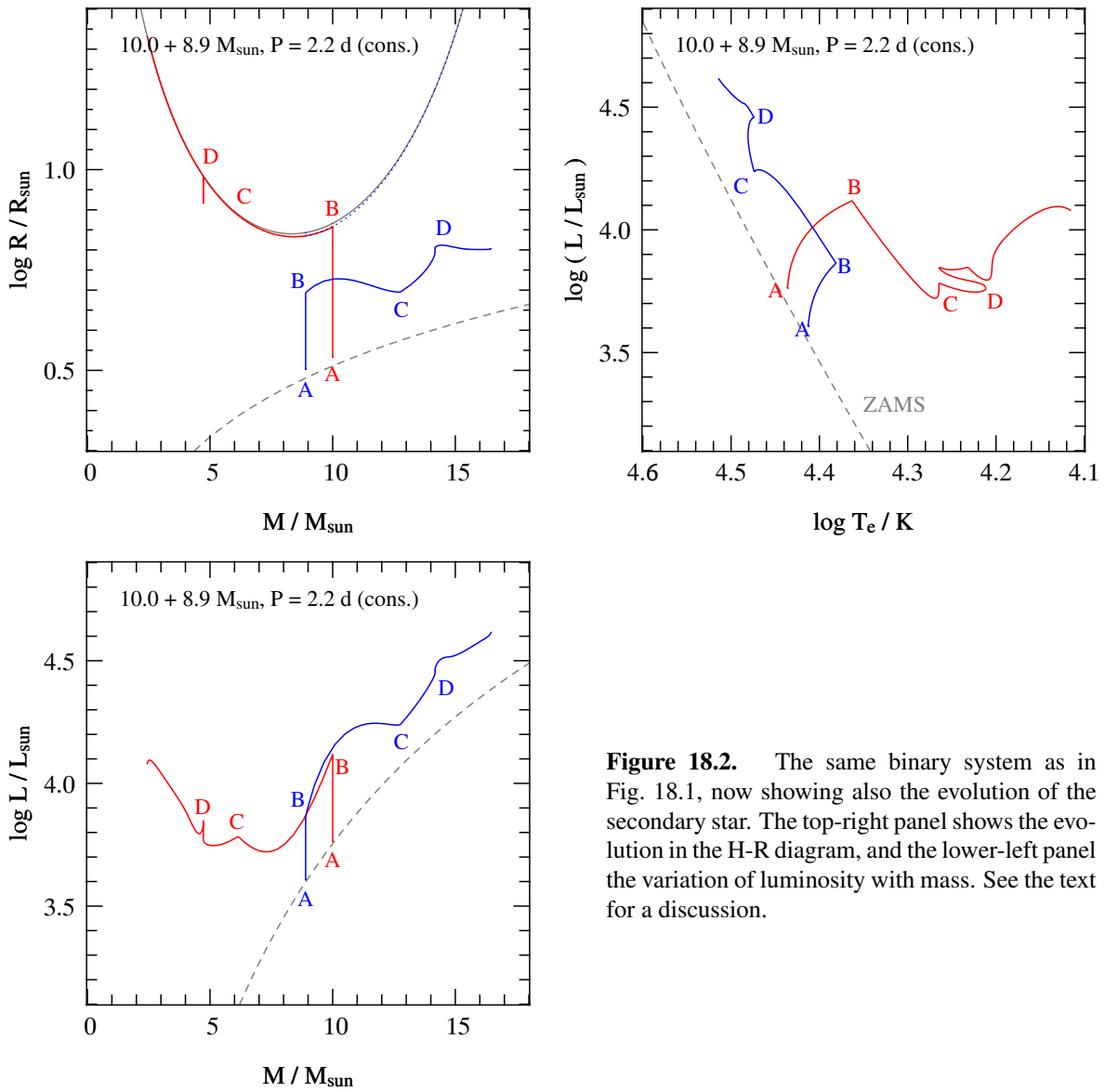


**Figure 18.2.** The same binary system as in Fig. 18.1, now showing also the evolution of the secondary star. The top-right panel shows the evolution in the H-R diagram, and the lower-left panel the variation of luminosity with mass. See the text for a discussion.

transfer (see Sec. 18.2).

Nelson & Eggleton (2001) computed a large grid of conservative case A evolution models, covering the entire parameter space in masses and orbital periods. They compared their models to observed Algol binaries. de Mink et al. (2007) performed similar calculations, also taking into account the possibility of non-conservative mass transfer ( $\beta < 1$ , see Sec. 17.1.2), and compared these models to semi-detached binaries in the Small Magellanic Cloud. These papers provide interesting background reading.

## 18.2 Case B evolution

Early case B mass transfer occurs in intermediate-mass and massive binaries with periods ranging from a few days up to tens or hundreds of days. The upper period limit is determined by the radius at which the donor star develops a deep convective envelope, which strongly depends on its mass (see Fig. 15.3); for low-mass stars the period range for this mode of mass transfer is very small as these

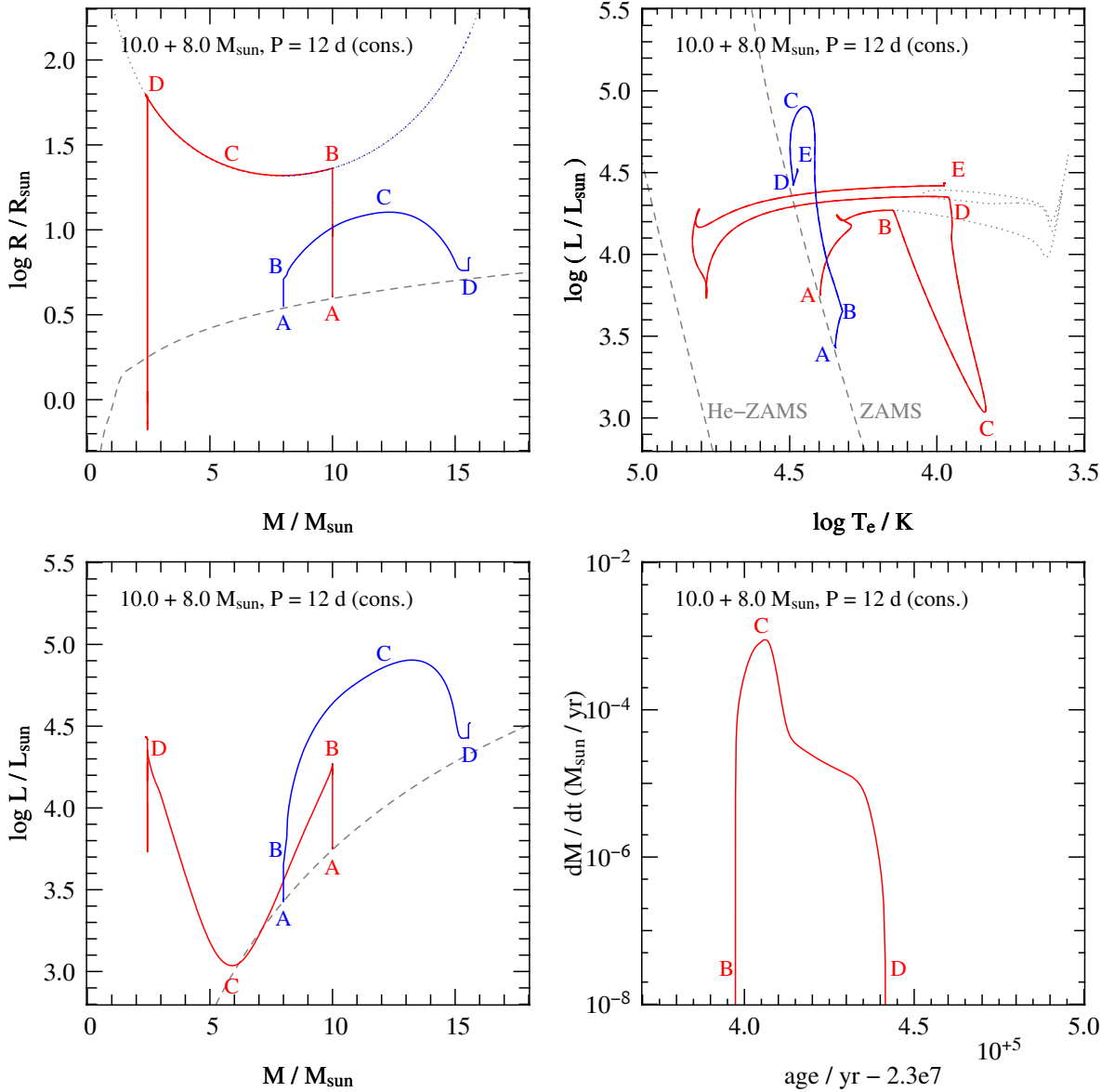


**Figure 18.3.** Conservative evolution of a binary of  $10.0 + 8.0 M_{\odot}$ ,  $P = 12$  d, undergoing case B mass transfer. Panels are similar to those in Fig 18.2, with the bottom-right panel showing the mass transfer rate as a function of time. Note the expanded scale: the entire mass-transfer phase (B-D) lasts  $< 2\%$  of the preceding MS lifetime. Point C corresponds to the maximum mass-transfer rate, coinciding with the minimum in the primary's luminosity and the maximum in the secondary's luminosity.

stars become red giants after only little expansion.

In many respects early case B mass transfer is similar to case A mass transfer. Since the donor's envelope is radiative, mass transfer starts with a rapid, thermal-timescale phase during which the mass ratio is reversed. An important difference is that since the primary is more extended and therefore has a shorter thermal timescale compared to case A, the mass transfer rates during the rapid phase are correspondingly higher. Furthermore the primary is itself in a rapid phase of evolution: while crossing the Hertzsprung gap it is out of thermal equilibrium and expands on the timescale at which its

**Table 18.2.** Some observed post-RLOF binaries. Masses and radii are given in solar units.

| name       | spectra         | $P$ (d) | $M_1$ | $M_2$ | $R_1$ | $R_2$ |
|------------|-----------------|---------|-------|-------|-------|-------|
| CQ Cep     | WN7 + O6        | 1.64    | 24    | 30    | 8.8   | 7.9   |
| V398 Car   | WN4 + O4-6      | 8.26    | 19    | 37    |       |       |
| GP Cep     | WN6/WC + O3-6   | 6.69    | 15    | 27    |       |       |
| CV Ser     | WC8 + O8-9      | 29.7    | 13    | 27    |       |       |
| V444 Cyg   | WN5 + O6        | 4.21    | 9.3   | 28    | 2.9   | 8.5   |
| $\phi$ Per | HeI em + B1IIIe | 127     | 1.15  | 9.3   | 1.3:  | 5.5–8 |

core contracts. As a consequence, after mass-ratio reversal mass transfer continues on the expansion timescale of the primary, only slightly slower than the thermal timescale. Therefore there is no ‘slow’ phase of mass transfer as in case A binaries. Mass transfer continues at a fairly high rate until most of the envelope has been transferred, as illustrated in Fig. 18.3. The evolution track describes a loop in the H-R diagram during the mass transfer phase, points B-D, with the maximum transfer rate coinciding with the minimum in luminosity of the primary at point C. The decrease in luminosity during mass transfer is caused by the strong thermal disequilibrium of the primary: as described in Sec. 17.3 a radiative donor star shrinks in response to mass loss and has to re-expand to regain thermal equilibrium. This requires the absorption of gravitational energy, so that the surface luminosity during thermal-timescale mass transfer is (much) smaller than the nuclear luminosity provided by the H-burning shell.

When helium is ignited in the core (point D) mass transfer stops: the primary contracts and detaches from its Roche lobe. This happens when the primary is almost reduced to its bare helium core, with only a thin H-rich layer. The primary moves to a position close to the helium main-sequence in the H-R diagram. From single-star evolution models of intermediate-mass and massive stars, the mass of the helium core after the main sequence (when the star crosses the Hertzsprung gap) is reasonably well approximated by

$$M_{\text{core}}/M_{\odot} \approx 0.10(M_i/M_{\odot})^{1.4} \quad \text{for } 2.5 M_{\odot} \lesssim M_i \lesssim 40 M_{\odot}, \quad (18.1)$$

where  $M_i$  is the initial mass. If we make the assumption of conservative mass transfer, we can use this relation to either (1) predict the outcome of case B mass transfer, or (2) trace back the evolution of an observed binary that we believe to have undergone case B mass transfer.

Since the mass-transfer phase in case B binaries is very short compared to case A binaries, observational counterparts are rare. Indeed the vast majority of observed Algol-type binaries have short periods,  $P < 10$  d. One likely example of a binary currently undergoing case B mass transfer is  $\beta$  Lyrae which we encountered in Exercise 17.2. On the other hand, the remnants of case B mass transfer are in a long-lived phase of evolution: these are binaries consisting of the almost bare helium-burning core of the primary and a more massive main-sequence star. Conservative mass transfer will have widened their orbits significantly. Observed counterparts of this evolution phase among massive systems are the WR+O binaries, consisting of a Wolf-Rayet star and a massive O star. Some examples are given in Table 18.2. Among intermediate-mass binaries on the other hand, not many counterparts are known. This is probably a selection effect: the He star is much hotter and less luminous than its companion, so it will be optically much fainter. Furthermore its low mass and the wide orbit after conservative mass transfer imply that the orbital velocity of the main-sequence star is undetectably small. The best candidate for this phase of evolution is the system  $\phi$  Persei: a binary with  $P_{\text{orb}} = 127$  d consisting of

a B1e main sequence star and a He emission-line object, presumably a naked He-burning star (Gies et al., 1998, see Table 18.2).

Some case A binaries – those that are able to avoid evolving into contact, see Sec. 18.3.3 – also experience a further phase of mass transfer after the primary star has finished central hydrogen burning, i.e. after point D in Figs. 18.1 and 18.2. This phase of mass transfer is rapid because it is driven by the rapid expansion of the donor star after it leaves the main sequence, even though the orbit expands in response to mass transfer since the donor has already become less massive than its companion. Similar to case B mass transfer, this mass transfer phase (often referred to in the literature as ‘case AB’ mass transfer) continues until almost the entire remaining hydrogen-rich envelope has been transferred and the donor becomes an almost bare helium star. The mass of the remaining helium star after case AB mass transfer will be smaller than given by eq. (18.1), because the donor star’s mass has been reduced by mass transfer during its main sequence phase so that it forms a less massive core than in case B binaries. In other respects, however, the remnants of case AB binaries have similar properties to those of case B binaries, and some of the systems listed in Table 18.2 may have followed such an evolution path.

## 18.3 Accretion and the response of the mass gainer

The mass transfer stream from the donor star that passes through the nozzle around the  $L_1$  point will follow a more-or-less ballistic trajectory into the Roche lobe of the companion. Due to the Coriolis force in the frame that co-rotates with the binary, the infalling gas gains angular momentum with respect to the accreting star, such that it would pass the center of mass of the star at a certain minimum distance  $d_{\min}$ . Detailed calculations show that  $d_{\min}$  scales approximately with the Roche-lobe radius  $R_{L,a}$  of the accreting star,  $d_{\min} \approx (0.1 \dots 0.2) R_{L,a}$ , with the proportionality factor depending on the mass ratio  $M_a/M_d$ . If  $d_{\min}$  is smaller than the radius  $R_a$  of the accreting star, the stream hits the star directly. In relatively wide orbits, when  $d_{\min} > R_a$ , the stream continues in its orbit around the star and collides with itself, forming an accretion disk around the companion. In either case, an important consequence is that not only mass but also angular momentum is transferred to the companion; relatively more in the case of an accretion disk. In the following we discuss the consequences of accretion for the structure and evolution of the companion star.

### 18.3.1 Accretion power

As matter falls towards the surface of the star it gains kinetic energy. The amount of energy gained per unit mass equals the difference in the gravitational-centrifugal potential between the Roche surface (the critical potential  $\Phi_L$ ) and the stellar surface ( $\Phi_a \approx -GM_a/R_a$ ). For a mass-transfer rate  $\dot{M}$  this yields an *accretion luminosity*

$$L_{\text{acc}} = \dot{M} \left( \frac{GM_a}{R_a} - |\Phi_L| \right) \quad (18.2)$$

If  $\dot{M}$  is large, or if the accretor is deep inside its Roche lobe – in which case the  $\Phi_L$  term can be ignored – a substantial luminosity can be generated.

This is particularly true if the accretor is a compact object (a white dwarf, neutron star or black hole); in this case we can write

$$L_{\text{acc}} = \frac{GM_a \dot{M}}{R_a} \quad (18.3)$$

This is the process that powers e.g. X-ray binaries. The smaller the radius, the more energy can be released. For a white dwarf with  $M \approx 0.7 M_\odot$  and  $R \approx 0.01 R_\odot$ , this yields  $L_{\text{acc}} \approx 1.5 \times 10^{-4} \dot{M} c^2$ .

For a neutron star with  $M \approx 1.4 M_{\odot}$  and  $R \approx 10$  km, we find  $L_{\text{acc}} \approx 0.2 \dot{M} c^2$  and for a black hole with Schwarzschild radius  $R \sim 2GM/c^2$  we find  $L_{\text{acc}} \sim 0.5 \dot{M} c^2$ , i.e. in the ideal case a sizable fraction of the rest mass may be released as energy. This accretion process is thus potentially much more efficient than nuclear fusion.

However, the accretion luminosity should not be able to exceed the Eddington luminosity,

$$L_{\text{acc}} \leq L_{\text{Edd}} = \frac{4\pi c GM_a}{\kappa} \quad (18.4)$$

where the opacity  $\kappa$  may be taken as the electron scattering opacity,  $\kappa_{\text{es}} = 0.2(1 + X) \text{ cm}^2/\text{g}$  for a hydrogen mass fraction  $X$ . Thus a compact accreting star may not be able to accrete more than a fraction of the mass that is transferred onto it by its companion. By equating  $L_{\text{acc}}$  to  $L_{\text{Edd}}$  we obtain the maximum accretion rate,

$$\dot{M}_{\text{Edd}} = \frac{4\pi c R_a}{\kappa} \quad (18.5)$$

The remainder of the mass may be lost from the binary system, in the form of a wind or jets blown from the vicinity of the compact star, or it may accumulate in the accretor's Roche lobe or in a common envelope around the system. For a white dwarf with  $R \approx 0.01 R_{\odot}$  accreting hydrogen-rich gas ( $X = 0.7$ ) we find  $\dot{M}_{\text{Edd}} \approx 1.2 \times 10^{-5} M_{\odot}/\text{yr}$ , and for a neutron star with  $R \approx 10$  km,  $\dot{M}_{\text{Edd}} \approx 1.7 \times 10^{-8} M_{\odot}/\text{yr}$ .

In the case of accreting main-sequence stars, the radii are so large that the Eddington limit plays a minor role in the accretion process. Instead, we are mainly interested in the effect of accretion on the structure of the accreting star. In the case that an accretion disk forms, the accretion energy is dissipated by viscous friction, partly inside the accretion disk and partly in the boundary layer between the inner edge of the disk and the stellar surface. In the case of direct impact ( $d_{\min} < R_a$ ), a 'hot spot' forms where the gas stream shocks with the stellar surface layers. In either case, the accretion luminosity is radiated away and very little, if anything, is added to the energy budget of the interior layers of the accreting star. Therefore, the structure of the star is believed to remain unaffected by the direct effects of accretion energy.

### 18.3.2 Evolutionary consequences of accretion

#### Spin-up of the accreting star

The matter that is transferred to the accreting star carries a significant amount of angular momentum, especially if it passes through an accretion disc. This can spin up the star to break-up rotation after accreting only about 10% of its original mass (Packet, 1981; Exercise 18.5). The star will then have to get rid of some of its angular momentum before further accretion can take place. This is known as the 'angular momentum problem' and it potentially puts a severe limit on the amount of mass the star can accrete, and thus on the efficiency of mass transfer by Roche-lobe overflow (i.e. the parameter  $\beta$  defined in Sec.17.1.2). Evidence that efficient spin-up by accretion indeed takes place comes from binaries such as  $\phi$  Per, discussed above, in which the secondary star is a rapidly rotating Be star that rotates very close to its critical velocity. The same process is responsible for the formation of the Be stars seen as companions in many high-mass X-ray binaries. At the same time, however, the wide orbit and small mass ratio of  $\phi$  Per are indicative of close-to-conservative mass transfer,  $\beta \sim 1$ , in contrast with the above angular momentum expectations.

Several processes may limit the severity of the 'angular momentum problem', or perhaps eliminate it altogether in some situations, and allow efficient mass transfer to take place. Tidal interaction with

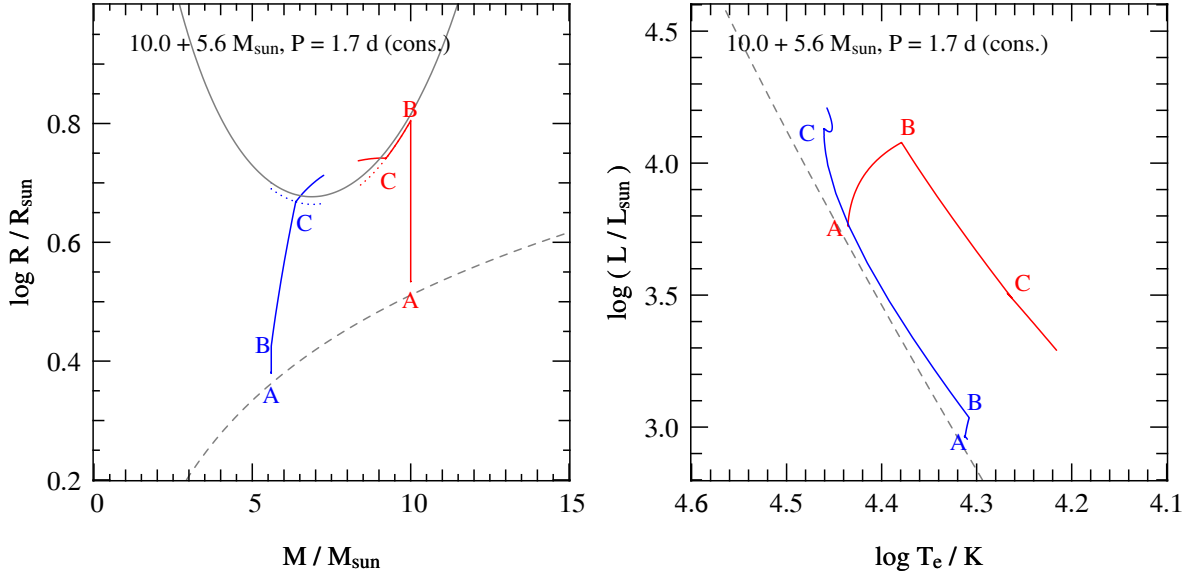


**Figure 18.4.** Similar to Fig 18.2, but for a binary with a more extreme initial mass ratio. The large difference in thermal timescales between the primary and secondary causes the secondary to become highly over-luminous and expand in response to accretion. As a result the secondary fills its Roche lobe during rapid mass transfer, after only a small amount of accretion, and a contact binary is formed at point C.

the companion (donor) star can slow down the rotation rate and transfer spin angular momentum back to the orbit, thus preventing the star from reaching critical rotation. However, this is effective only in very close binaries with periods less than a few days. It has also been argued that a star rotating at its break-up limit can still keep accreting mass from an accretion disk without accreting angular momentum as a result of viscous coupling in the disk and its boundary layer, which can transport angular momentum outward while mass flows inward. This may apply to mass transfer in wider binaries, such as that which led to the formation of  $\phi$  Per. Another way by which the accreting star may get rid of its angular momentum is by mass loss. In massive binaries at least, the (normally weak) stellar wind may be enhanced enormously when the star is rotating very close to critical; this enhanced wind then takes away the excess angular momentum. However, this process is less effective in removing angular momentum than tidal interaction or viscous coupling with the accretion disk and results in non-conservative mass transfer, with a relatively small value of  $\beta$ . This may, however, be relevant for the formation of some of the massive WR+O binaries in Table 18.2.

### Thermal readjustment and expansion

The accreting star has to adjust its structure to the extra mass that it receives. The main effect of mass accretion on the structure is the compression of interior layers by the added weight of the accreted gas, which releases gravitational energy. If the rate of gravitational energy release is larger than its luminosity, the star will be brought out of thermal equilibrium. This is the case if accretion takes place on a timescale shorter than the accretor's Kelvin-Helmholtz timescale. One may then expect the reverse of the effect of rapid mass loss on the donor star (Sec. 17.3): accretion onto a star with a convective envelope makes it shrink, while accretion onto a star with a radiative envelope causes it to expand. This is indeed borne out by detailed calculations.

During the first mass transfer phase the thermal timescale of the secondary is longer than that

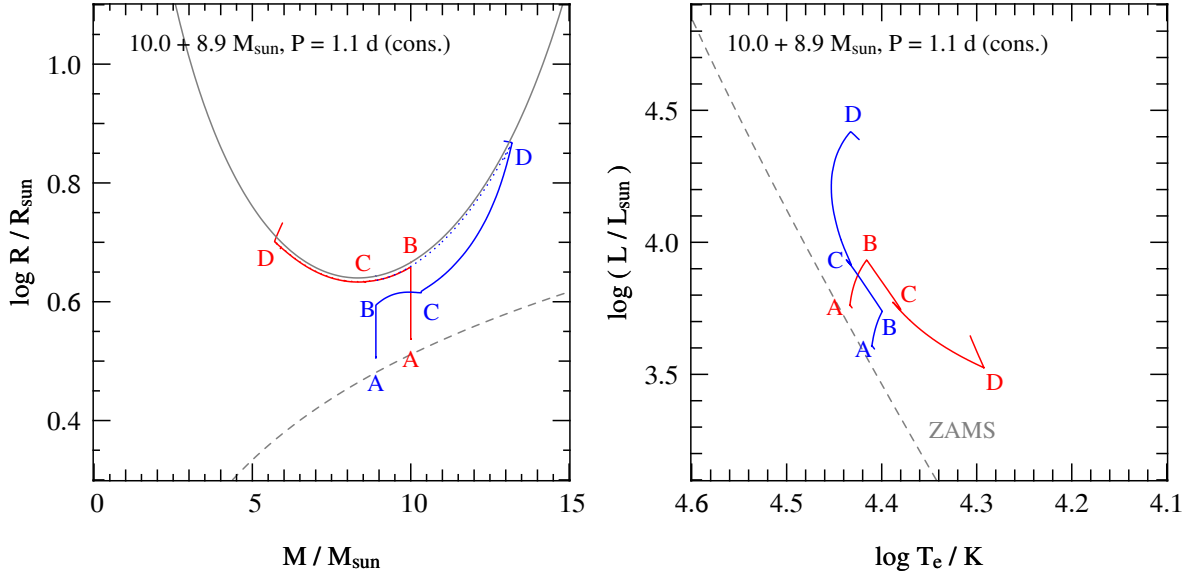


**Figure 18.5.** Similar to Fig 18.2, but for a binary with a smaller orbital period. During rapid mass transfer (BC) the secondary remains close to thermal equilibrium, but during the subsequent slow mass transfer (C-D) its evolution speeds up and eventually overtakes that of the primary. As a result a contact binary is formed at point D.

of the primary (the mass donor), which sets the timescale of mass transfer, so that the accretor will be brought out of thermal equilibrium. This makes it brighter than the main-sequence luminosity appropriate for its mass, and for sufficiently high accretion rates, also causes substantial expansion of the star compared to its main-sequence radius (e.g. see Fig. 18.3, point C on the evolution track of the secondary). As a consequence the secondary can fill its own Roche lobe and a contact binary may be formed during the first, rapid phase of mass transfer in a case A or case B binary. An example of this situation is given in Fig. 18.4.

### Rejuvenation

If mass transfer is indeed (close to) conservative then the mass of the secondary is increased significantly. This has two effects on its further evolution. First, the added mass causes its convective core to grow in mass, mixing in fresh fuel from outer layers into the nuclear-burning zone in the center. This process is called rejuvenation, since it has the effect of extending the main-sequence lifetime of the secondary.<sup>1</sup> This can be seen in Fig 18.3 where after mass transfer (point D) the secondary is closer to the ZAMS than when mass transfer started (point B). The rejuvenation effect is counteracted, however, by the fact that its nuclear timescale (which scales approximately with  $M^{-2.8}$ ) becomes much shorter. The combined result is that the secondary can overtake the evolution of the primary under some circumstances, i.e. it can be in a more advanced stage of evolution despite the fact that it started out with a smaller mass. An example of how this ‘overtaking’ can cause the secondary star to expand and fill its own Roche lobe during slow mass transfer in a case A binary is given in Fig. 18.5.

<sup>1</sup>Not all detailed evolution models of accreting stars show such rejuvenation, since this process depends on the uncertain mixing efficiency in semi-convective layers.

### 18.3.3 Evolution into contact

A number of studies have investigated for which binary parameters the secondary can evolve into contact (Pols, 1994; Nelson & Eggleton, 2001; Wellstein et al., 2001; de Mink et al., 2007). In these binary evolution calculations the potential ‘angular momentum problem’ caused by the spin-up of the secondary was neglected. The results indicate that contact can arise in three different circumstances:

1. During rapid (thermal timescale) RLOF, either in case A or early case B. This occurs for  $M_2/M_1 < q_{\text{cr}}$ , where  $q_{\text{cr}}$  is in the range 0.5 – 1 depending on primary mass. In this case the thermal timescale of the accretor is much longer than the accretion timescale, so that it swells up quickly and fills its Roche lobe after accreting only a small amount of mass (e.g. Fig. 18.4).
2. During the slow (nuclear timescale) phase of RLOF in case A after the mass ratio is reversed. For very short  $P_{\text{orb}}$  the nuclear evolution of the secondary can then overtake that of the primary (e.g. Fig. 18.5). The ensuing contact stage may be quite long-lived given that massive contact binaries are not uncommon, but the evolution of such systems is not well understood.
3. During the late phase of RLOF in case B for fairly long periods, when  $\dot{M}$  accelerates as the envelope of the donor becomes partly convective. In this case, a contact binary is formed after substantial mass accretion has already taken place.

Based on the above, regions in parameter space ( $q_0$  and  $P_0$ ) where contact is avoided can be identified. Examples of this can be found in the papers cited above.

Neglecting other effects, one might expect conservative mass transfer in those systems that avoid contact altogether, and up to the point where contact is reached in the other cases. However, the further evolution of contact binaries is highly uncertain, and how much mass and angular momentum these systems lose are still open questions. It seems likely that a case A contact binary must eventually merge to a single star, while in a case B situation the contact binary may quickly evolve into a common-envelope configuration (Sec. 20.1).

## Exercises

- 18.1** Consider the binary depicted in Fig. 18.1. Verify that the rapid mass-transfer phase (B–C) indeed takes place on the thermal timescale of the donor, and that the slow phase (C–D) takes place on the nuclear timescale of the donor. Assume typical values for a  $10 M_\odot$  main-sequence star.
- 18.2** We have seen that for case B mass transfer in intermediate-mass or massive binaries, almost the entire envelope of the donor star is transferred and the remnant is the almost bare helium core of the donor. For a binary system with masses  $4 + 3 M_\odot$ , see Exercise 15.5, calculate the masses of the components after conservative case B mass transfer. Subsequently calculate the range of final orbital periods after conservative case B mass transfer, taking into account for which systems you may reasonably expect the conservative assumption to hold.
- 18.3** Compare the outcome of case B mass transfer for a primary mass of  $4 M_\odot$  (previous exercise) with that of  $10 M_\odot$  and  $40 M_\odot$ , assuming the same initial mass ratio of 0.75, in terms of (a) the final mass ratio and (b) the ratio of final to initial orbital period.
- 18.4** Assuming the He-star + Be-star system  $\phi$  Persei (see Table 18.2) formed by conservative case B mass transfer, calculate the initial masses and orbital period of the binary. Is this consistent with the case B assumption?

- 18.5** Consider a star that is being spun up by accreting gas from the inner edge of a Keplerian accretion disk. Write the angular momentum of the star as  $J_* = r_g^2 MR^2\Omega$ . Assume that initially the star has  $\Omega = 0$ , and that the radius of the star  $R$  and the dimensionless structure parameter  $r_g^2 \approx 0.10$  do not change as the star accretes and spins up. Calculate by which factor the mass  $M$  can increase until the surface reaches break-up rotation ( $\Omega = \Omega_{\text{Kep}}$ ).

# Chapter 19

## Observed binaries with compact objects

As an intermezzo to our discussion of binary evolution, this chapter provides an overview of observed types of binaries in which one or both stars are compact objects (white dwarfs, neutron stars or black holes). In order to understand their properties additional, non-conservative evolution processes need to be considered besides the stable mass transfer discussed so far. These processes will be discussed in Chapter 20.

### 19.1 White dwarf binaries

Among observed main-sequence binaries with unseen companions, a sizable fraction is likely to contain a white dwarf that has cooled beyond detection. Here we discuss only those systems in which the white dwarf is observed directly, or its presence is revealed by current or past interaction with its companion. Binaries consisting of a white dwarf and a normal star can be divided into systems with close orbits ( $P \lesssim 10$  d) and those with relatively wide orbits ( $P \gtrsim 100$  d).

#### 19.1.1 Close detached white-dwarf binaries

**Detached main-sequence white-dwarf binaries** Several white dwarfs have been detected in a close detached orbit ( $P \lesssim 10$  d) around a low-mass main-sequence star. Some examples are given in Table 19.1. In these systems the orbits are much smaller than the size of the red-giant progenitor of the white dwarf, and their formation requires strong mass and angular momentum loss in the form of a common envelope phase and spiral-in (see Sec. 20.1).

Closely related are so-called double cores of planetary nebulae, in which the hot nucleus of the nebula which will later cool into a white dwarf is accompanied by a low-mass star in a close orbit. About 5 to 10 per cent of all planetary nebulae have such double cores. In these systems the nebula is probably the ejected common envelope that formed the close binary. These detached binaries may evolve, by means of either angular momentum loss from the orbit (see Sec. 20.2) or nuclear expansion of the main-sequence star, into one of the two types of semi-detached, interacting binaries discussed in Sec. 19.1.2.

**Double white dwarfs** Many short period binaries consisting of two white dwarfs have been discovered in recent years, see Table 19.1 for a few examples. Their orbital periods range from  $P \sim 0.06$ –30 d. In most cases the masses of the white dwarfs are low,  $\lesssim 0.45 M_{\odot}$ , which means that they must be composed of helium rather than carbon and oxygen. The masses of the two white dwarfs are often rather similar, which provides important clues for their formation. The closest systems among them are expected to merge within a Hubble time due to angular momentum loss by gravitational radiation.

**Table 19.1.** Some close white-dwarf binaries. Masses and radii are given in solar units. If no eccentricity is given the orbit is circular. Mass values in *italics* indicate the measured mass function, rather than the mass.

| name  | spectra      | $P$ (d) | $e$   | $M_1$ | $M_2$  | $R_1$ | $R_2$ |
|---|--------------|---------|-------|-------|--------|-------|-------|
| close binaries inside planetary nebulae     |              |         |       |       |        |       |       |
| KV Vel                                      | sdO + CIIIe  | 0.357   |       | 0.63  | 0.23   | 0.16  | 0.40  |
| UU Sge                                      | sdO + M?     | 0.465   |       | 0.63  | 0.29   | 0.33  | 0.54  |
| V477 Lyr                                    | sdO + M?     | 0.472   |       | 0.51  | 0.15   | 0.17  | 0.46  |
| BE UMa                                      | sdO + M?     | 2.29    |       | 0.7:  | 0.36:  | 0.08: | 0.7:  |
| V651 Mon                                    | sdO + A5Vm:  | 16.0    | 0.07: |       | 0.0073 |       |       |
| detached white dwarf-main sequence binaries |              |         |       |       |        |       |       |
| HR Cam                                      | WD + M       | 0.103   |       | 0.41  | 0.10   | 0.018 | 0.125 |
| 13471-128                                   | WD + M3.5/4  | 0.151   |       | 0.78  | 0.43   | 0.011 | 0.42  |
| NN Ser                                      | WD + M5-6    | 0.130   |       | 0.57  | 0.12   | 0.019 | 0.17  |
| CC Cet                                      | WDA2 + M4.5e | 0.284   |       | 0.39  | 0.18   |       | 0.21  |
| GK Vir                                      | WDAO + M3-5V | 0.344   |       | 0.51  | 0.10   |       | 0.15  |
| V471 Tau                                    | WD + K2V     | 0.521   |       | 0.84  | 0.93   | 0.011 | 0.96  |
| Feige 24                                    | WD + M1.5V   | 4.23    |       | 0.47  | 0.30   | 0.032 |       |
| double white dwarf binaries                 |              |         |       |       |        |       |       |
| 0957-666                                    | WDA + WDA    | 0.061   |       | 0.32  | 0.37   |       |       |
| 1101+364                                    | WDA3 + WDA   | 0.145   |       | 0.33  | 0.29   |       |       |
| 1704+481a                                   | WDA4 + WD    | 0.145   |       | 0.56  | 0.39   |       |       |
| HE 1414-0848                                | WD + WD      | 0.518   |       | 0.55  | 0.71   |       |       |
| 1399+144                                    | WD + WD      | 2.209   |       | 0.44  | 0.44   |       |       |

### 19.1.2 Cataclysmic variables and related systems

**Cataclysmic variables** The name of this group derives from their outbursting nature, they comprise the *classical novae* and related systems, see Table 19.2. They consist of a low-mass main-sequence star and a white dwarf, the MS star is filling its Roche lobe and transferring mass to the WD via an accretion disk. Orbital periods are typically  $0.05 \text{ d} \lesssim P \lesssim 0.5 \text{ d}$ , with a few exceptions. In between outbursts, the accretion disk is often the main source of light in the system. The white dwarf is more massive than its companion,  $q = M_{\text{MS}}/M_{\text{WD}} \lesssim 0.7$  so that Roche-lobe overflow is stable and occurs at a low rate ( $\dot{M} \sim 10^{-11}\text{--}10^{-9} M_{\odot}/\text{yr}$ ). The low accretion rate results in hydrogen piling up on the surface of the white dwarf, until it ignites in a flash when the pressure and temperature at the bottom of the accreted layer are high enough for fusion. The resulting thermonuclear runaway leads to the observed nova outbursts during which the visual luminosity increases by a factor  $10^4\text{--}10^6$ .

Probably all cataclysmic variables undergo nova outbursts, but only in a subset of them have they been observed. This is consistent with the expected time between thermonuclear flashes,  $\gtrsim 10^4$  years. Many other CVs, known as *dwarf novae*, show outbursts of a different kind, milder in nature (up to a factor  $10^2$  in luminosity) and occurring every few weeks. These are probably the result of an instability in the accretion disk, which builds up until the viscosity suddenly increases and the accumulated mass is rapidly dumped onto the white dwarf. In other systems, known as *polars*, the white dwarf is highly magnetized and dominates the accretion flow, either completely (magnetic polars, in which the accretion disk is absent and the white dwarf rotation is locked with the orbit) or partly (intermediate polars, which have small accretion disks truncated on the inside by the

**Table 19.2.** Some cataclysmic variables and supersoft X-ray sources. Masses and radii are given in solar units. Types: CN - classical nova; DN - dwarf nova; MP - magnetic polar; IP - intermediate polar; UCB - ultra-compact binary; SSX - supersoft X-ray source.

| name   | spectra      | type   | $P$ (d) | $M_1$ | $M_2$ | $R_1$ | $R_2$ |
|--------|--------------|--------|---------|-------|-------|-------|-------|
| AM CVn | He em        | UCB    | 0.012   |       | 0.04: |       |       |
| OY Car | sdBe + M7-8  | DN     | 0.063   | 0.685 | 0.07  |       | 0.127 |
| Z Cha  | sdBe + M5.5V | DN     | 0.075   | 0.84  | 0.125 |       | 0.17  |
| AM Her | sdBe + M4V   | MP     | 0.129   | 0.44  | 0.29  |       | 0.33  |
| U Gem  | sdBe + M4V   | DN     | 0.177   | 1.26  | 0.57  |       | 0.51  |
| DQ Her | sdBe + M3V   | CN, IP | 0.194   | 0.60  | 0.40  |       | 0.49  |
| BT Mon | sdBe + G8V   | CN     | 0.334   | 1.04  | 0.87  |       | 0.89  |
| GK Per | sdBe + K1IV  | CN, DN | 2.00    | 0.9:  | 0.5:  |       | 2.5:  |
| V Sge  | WN: + B8:    | SSX    | 0.514   | 0.9:  | 3.3:  |       | 2.1   |
| U Sco  | sdBe + F8V   | SSX    | 1.23    | 1.55: | 0.88  |       | 2.1   |

white-dwarf magnetosphere).

**Supersoft X-ray sources** The ROSAT mission, which was sensitive to X-ray photons with energies  $\lesssim 500$  eV, has led to the discovery in the 1990s of a class of X-ray sources that emits only at these low energies. Various types of objects could give rise to such very soft X-ray emission. The most luminous persistent sources, with  $L \sim 10^{36-38}$  erg/s and blackbody temperatures of several times  $10^5$  K, are white dwarfs undergoing steady nuclear burning of hydrogen on their surfaces. Theoretical accretion models show that this happens if a WD accretes at a steady rate of  $1-2 \times 10^{-7} M_\odot/\text{yr}$ . This is typically what is expected for thermal-timescale mass transfer from a main-sequence or subgiant donor of  $1.3-2.5 M_\odot$  to a less massive white dwarf. Their orbital periods typically range from 0.2 to 4 d, making SSXs the higher-mass analogues of CVs. The steady accretion rate may bring the white dwarf over the Chandrasekhar limit, and these systems are therefore considered as possible progenitors of Type Ia supernovae. (In contrast, in CVs the nova outbursts eject most or all of the previously accreted mass so that the white dwarf mass does not grow.)

### 19.1.3 Symbiotic binaries and related systems

Symbiotic stars (see Table 19.3) show the combined spectrum of a cool giant superimposed with emission lines of hydrogen and helium. The emission spectrum comes from a hot white dwarf that accretes matter from its red giant or AGB companion, either from the strong stellar wind of the giant or in some cases by Roche-lobe overflow. The accretion (at rates up to  $10^{-7} M_\odot/\text{yr}$ ) heats the white dwarf so that it competes in luminosity with the red giant ( $100-1000 L_\odot$ ) and becomes visible. The orbital periods of symbiotic binaries range from  $P \sim 10^2-10^4$  days. Several symbiotics show nova outbursts, often recurrent in nature (symbiotic novae) and some are also observed as supersoft X-ray sources. Hence the classes of symbiotic binaries and cataclysmic variables partly overlap.

Related to symbiotic binaries in their evolutionary history, but different in appearance, are the barium and CH stars. They are red giants or subgiants in binaries with similar periods ( $P \sim 10^2-10^4$  d) but the white dwarf is usually not directly observed. The presence of a white dwarf is inferred, apart from the radial velocity variations, from the abundance anomalies in the spectrum of the (sub)giant which is enhanced in carbon and heavy s-process elements, in particular barium. These elements

**Table 19.3.** Some symbiotic and barium-star binaries. The last column gives the mass function of the giant (secondary) component; radial velocity variations of the white dwarf are generally not measured.

| name                | spectra       | $P$ (d) | $e$  | $f(M_2)$ |
|---------------------|---------------|---------|------|----------|
| symbiotic binaries  |               |         |      |          |
| T CrB               | Be + M4III    | 227.7   | 0    | 0.32     |
| AG Dra              | sdOe + K3pII  | 549     | 0.13 | 0.008    |
| BD Cam              | WD + M3/S5    | 597     | 0.09 | 0.037    |
| barium star systems |               |         |      |          |
| HD 77247            | ? + G7IIBa    | 80.53   | 0.09 | 0.0050   |
| 105 Her             | ? + K3IIBa    | 486     | 0.36 | 0.135    |
| $\xi^1$ Cyg         | WD + G7IIIIBa | 1642    | 0    | 0.035    |
| $\zeta$ Cap         | WD + G5IbBa   | 2380    | 0.28 | 0.0042   |
| $\zeta$ Cyg         | WD + G8IIIIBa | 6489    | 0.22 | 0.0227   |

were produced by the progenitor of the white dwarf while it was an AGB star (see Chapter 11) and have been transferred to the lower-mass main-sequence companion, now seen as a giant.

## 19.2 Neutron-star and black-hole binaries

*This section is adapted from lecture notes on Binary Stars by F. Verbunt.*

Binaries containing a neutron star or a black hole can often be observed as strong sources of X-rays as a result of accretion onto the compact object (Sect. 18.3.1). Such binaries are known as X-ray binaries; some examples are given in Table 19.4. Investigation of the properties of the brightest X-ray sources showed that they can be divided in two clearly separate types. Some sources emit their X-rays partially pulsed, others only show irregular variations. Many systems in the latter category occasionally show sudden surges in the X-ray flux, known as X-ray bursts. In the absence of accretion, a neutron star (but not a black hole) in a binary can be observed as a binary radio pulsar (Sec. 19.2.4).

### 19.2.1 High-mass X-ray binaries

The model for X-ray pulsars is that they are neutron stars with a strong dipolar magnetic field, which focusses the accreting matter to the magnetic poles, where it is stopped and emits X-rays. As the poles rotate in and out of view, we observe pulses of X-rays. Signs of the magnetic fields are thought to have been detected in the form of cyclotron absorption lines in the X-ray spectra.

Many X-ray pulsars have been successfully identified at optical wavelengths, and their counterparts almost invariably are massive O or B stars. The X-ray pulse period varies due to the orbital motion of the neutron star around its companion; when the radial velocity curve of the O or B star can be measured as well, we have a double-lined spectroscopic binary. If in addition the neutron star is eclipsed by its companion, classical binary techniques can be employed to determine the masses of both stars. The neutron star masses cluster around  $1.4 M_\odot$ , as expected from theory.

Some X-ray sources with an O or B companion star do not show pulses. The X-ray source in these may or may not be a neutron star. In some cases, which include Cyg X-1 and LMC X-3, the orbital velocity of the O or B supergiant indicates a mass for the compact star in excess of the maximum

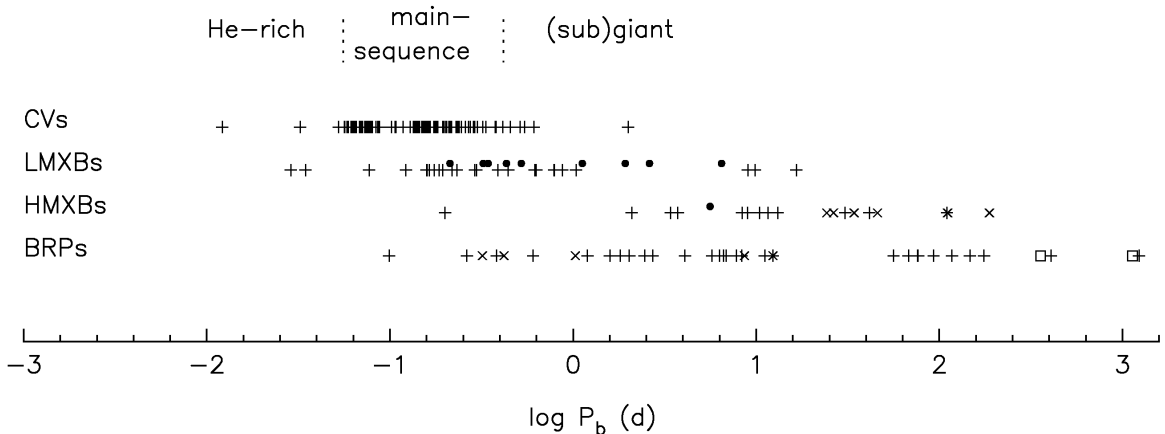


**Figure 19.1.** Orbital periods of cataclysmic variables, X-ray binaries and binary radio pulsars in our Galaxy. Each symbol indicates one system. For the X-ray binaries • indicates a system with a black hole, and × a Be donor star. For the binary radio pulsars + indicates a system with a low-mass white dwarf companion, × a system with a high-mass white dwarf or neutron star companion, and □ a main-sequence companion. Figure adapted from Verbunt (2013).

mass that is possible for a neutron star, and it is concluded that the compact star must be a black hole. The X-ray spectra of these black hole candidates contain more photons both at low energies ( $< 1 \text{ keV}$ ) and at high energies (up to  $> 100 \text{ keV}$ ) than the pulsar spectra.

Mass determinations are feasible in systems with relatively short orbital periods,  $P \lesssim 10 \text{ d}$ , in which the companion of the neutron star is an O or B supergiant. Many systems have rather longer orbital periods, up to more than a year. In these, the companion is usually a Be star, i.e. a rapidly rotating B star, and the X-ray emission is only detected occasionally. Taking selection effects against detection of such transient hard X-ray sources into account, we conclude that the Be-star + X-ray-pulsar binaries are in fact much more common (a few thousand in the Galaxy) than the supergiant + X-ray-pulsar systems (a dozen in the Galaxy). For both types of systems we find that the X-ray luminosity emitted near the neutron star is comparable to the optical luminosity of the O or B star.

The pulse periods of all X-ray pulsars vary, on time scales ranging from  $P/\dot{P} \approx 100 \text{ yr}$  to  $10^6 \text{ yr}$ . These short time scales indicate that the moments of inertia, and hence the radii, of these objects are very small, in agreement with the theoretical estimates for neutron-star radii of  $\sim 10 \text{ km}$ .

### 19.2.2 Low-mass X-ray binaries

Soon after the discovery of the X-ray bursts, it was realized that these are caused by the sudden fusion into carbon of a helium layer on a neutron star, deposited there by the accretion of hydrogen which fuses immediately into helium. Thus, a burst is the neutron-star analogue of a nova outburst for a white dwarf. The X-ray spectra of the X-ray bursts have characteristic temperatures of  $kT \lesssim 5 \text{ keV}$ . The steady X-ray spectrum of the luminous burst sources is soft; less luminous sources have power-law spectra. The spectra of sources of variable luminosity change accordingly.

Orbital periods for X-ray binaries without pulses can be inferred from flux variations in X-rays and/or optical photometry. The orbital periods span the same range as those of the cataclysmic variables (Fig. 19.1), which by analogy is taken to suggest that the companion to the neutron star is a low-mass star, close to the main sequence. These X-ray sources are therefore called *low-mass X-ray binaries*. Direct measurements of the properties of the donor star are hard to obtain, because the optical luminosity is dominated by reprocessing into the optical of X-rays that impinge on the

**Table 19.4.** Name, position, pulse period, X-ray luminosity, orbital period and eccentricity, and (for high-mass systems) the spectral type of the donor, for representative X-ray binaries. Binaries containing a black hole, and transients are indicated with B and T, respectively. For transients, the luminosity is the luminosity at outburst maximum. It should be noted that luminosities are uncertain due to uncertain distances for many sources.

| name                     | position  | $P_{\text{pulse}}$<br>(s) | $\log L_X$<br>(erg/s) | $P$<br>(d) | $e$      | sp.type |
|--------------------------|-----------|---------------------------|-----------------------|------------|----------|---------|
| high-mass X-ray binaries |           |                           |                       |            |          |         |
| LMC X-4                  | 0532 – 66 | 13.5                      | 38.6                  | 1.4        | 0.011    | O7III   |
| LMC X-3                  | 0538 – 64 | -                         | B                     | 38.5       | 1.7      | ~0      |
| Cen X-3                  | 1119 – 60 | 4.8                       | 37.9                  | 2.1        | 0.0007   | O6.5II  |
| SMC X-1                  | 0115 – 74 | 0.7                       | 38.8                  | 3.9        | <0.0008  | B0I     |
| Cyg X-1                  | 1956 + 35 | -                         | B                     | 37.3       | 5.6      | ~0      |
| Vela X-1                 | 0900 – 40 | 283                       |                       | 36.8       | 9.0      | B0.5I   |
| LMC tran                 | 0535 – 67 | 0.069                     |                       | T 39.0     | 16.7     | ~0.7    |
| V635 Cas                 | 0115 + 63 | 3.6                       |                       | T 36.9     | 24.3     | Be      |
| BQ Cam                   | 0331 + 53 | 4.4                       |                       | T 35.8     | 34.3     | Be      |
| GX301-2                  | 1223 – 62 | 696                       |                       | 37.0       | 41.5     | B1-1.5  |
| V725 Tau                 | 0535 + 26 | 104                       |                       | T 37.3     | 111.0    | Be      |
| low-mass X-ray binaries  |           |                           |                       |            |          |         |
| KZ TrA                   | 1627 – 67 | 7.7                       | 36.8                  | 0.029      |          |         |
| V1405 Aql                | 1916 – 05 |                           | 36.9                  | 0.035      |          |         |
| UY Vol                   | 0748 – 68 |                           | T 37.0                | 0.159      |          |         |
| V4134 Sgr                | 1755 – 34 |                           | 36.8                  | 0.186      |          |         |
| V616 Mon                 | 0620 – 00 |                           | B                     | T 38.3     | 0.323    |         |
| N Mus 1991               | 1124 – 68 |                           | B                     | T 37.6     | 0.427    |         |
| Cen X-4                  | 1455 – 31 |                           |                       | T 38.0     | 0.629    |         |
| Sco X-1                  | 1617 – 16 |                           |                       | 37.5       | 0.787    |         |
| V404 Cyg                 | 2023 + 33 |                           | B                     | T 38.4     | 6.500    |         |
| peculiar systems         |           |                           |                       |            |          |         |
| Her X-1                  | 1656 + 35 | 1.2                       | 36.8                  | 1.7        | < 0.0003 | A9-B    |
| Cyg X-2                  | 2142 + 38 |                           | 38.0                  | 9.843      |          | A9      |
| Cyg X-3                  | 2030 + 41 |                           | 38.0                  | 0.2        |          | WN      |
| Cir X-1                  | 1516 – 57 |                           | T 38.9                | 16.6       |          |         |
| SS433                    | 1909 + 05 |                           | 35.8                  | 13.2       |          |         |

accretion disk around the neutron star. The optical luminosity of these systems is much less than the X-ray luminosity, typically  $L_{\text{opt}} \lesssim 0.01L_X$ , and their low visual brightness impedes easy optical identification.

The thick accretion disk is also responsible for the paucity of eclipsing low-mass X-ray binaries: when the inclination is high enough for the neutron star to be eclipsed by its companion, the probability is high that it is hidden altogether by the accretion disk.

Some low-mass X-ray binaries are transient sources. In these, the optical flux from the disk disappears with the X-ray flux, and the companion becomes optically detectable. The radial velocity curve of the companion can then be measured. The companions in transients indeed appear to be low-mass stars, i.e. with spectral type G or K. In many such transients the mass function indicates that the compact accreting star is a black hole. The X-ray spectra of transients with a black hole

**Table 19.5.** Position, pulse period, characteristic age ( $\tau_c \equiv P/(2\dot{P})$ ), magnetic field strength, orbital period and eccentricity, and companion mass, for representative radio pulsar binaries. The companion masses marked \* were calculated for an assumed inclination of 60°.

| position                                | $P_{\text{pulse}}$<br>(ms) | $\log \tau_c$<br>(yr) | $\log B$<br>(G) | $P$<br>(d) | $e$      | $M_c$<br>( $M_\odot$ ) |
|---|----------------------------|-----------------------|-----------------|------------|----------|------------------------|
| high-mass binary radio pulsars          |                            |                       |                 |            |          |                        |
| 1913 + 16                               | 59.0                       | 8.0                   | 10.4            | 0.32       | 0.6171   | 1.39                   |
| 1534 + 12                               | 37.9                       | 8.4                   | 10.0            | 0.42       | 0.2737   | 1.36                   |
| 0655 + 64                               | 195.6                      | 9.7                   | 10.1            | 1.03       | <0.00005 | >0.7                   |
| 2303 + 46                               | 1066.4                     | 7.5                   | 11.9            | 12.34      | 0.6584   | 1.5                    |
| low-mass binary radio pulsars           |                            |                       |                 |            |          |                        |
| 1957 + 20                               | 1.6                        | 9.2                   | 8.2             | 0.38       | <0.001   | 0.02                   |
| 1831 – 00                               | 521.0                      | 8.8                   | 10.9            | 1.81       | <0.005   | 0.07*                  |
| J0437 – 47                              | 5.8                        | 8.9                   | 8.9             | 5.74       | 0.000018 | 0.17*                  |
| 1855 + 09                               | 5.4                        | 9.7                   | 8.5             | 12.33      | 0.000021 | 0.23                   |
| 1953 + 29                               | 6.1                        | 9.5                   | 8.6             | 117.35     | 0.00033  | 0.22*                  |
| 0820 + 02                               | 864.9                      | 8.1                   | 11.5            | 1232.40    | 0.0119   | 0.23*                  |
| antediluvian <sup>a</sup> radio pulsars |                            |                       |                 |            |          |                        |
| 1259 – 63                               | 47.8                       |                       |                 | 1236.8     | 0.870    | Be                     |
| 1820 – 11 <sup>b</sup>                  | 279.8                      | 6.5                   | 11.8            | 357.8      | 0.795    | 0.8*                   |

<sup>a</sup>i.e. in an evolutionary stage preceding mass transfer

<sup>b</sup>this pulsar is tentatively listed as antediluvian; alternatively, this system may be a high-mass binary radio pulsar

are remarkably similar to those of transients with a neutron star; the difference being that at the brightest levels they have (relatively) more soft as well as more hard photons. The case of Cyg X-3 (see Sec. 19.2.3) illustrates that the assumption of a low-mass donor remains insecure for most of the low-mass X-ray binaries.

### 19.2.3 Peculiar X-ray binaries

**Pulsars with low-mass donors** Whereas most X-ray pulsars have O or B star companions, some have low- or intermediate-mass companions. The best known of these is Her X-1, which has a  $\approx 2 M_\odot$  companion, which is slightly evolved. Its age is therefore in excess of  $\approx 5 \times 10^8$  yr, and Her X-1 is an excellent example of an old neutron star with a strong magnetic field. The binary is also striking in being removed from the Galactic Plane, at  $|z| \approx 3$  kpc. The X-ray pulsar 4U1626-67 has a companion in a  $\approx 40$  min orbit, whose mass must be less than  $0.1 M_\odot$ . For some other pulsars, including 1E2259+59, there is no sign of any companion. It has been suggested that these are single, accreting from a disk; or that they do not accrete, but have very high magnetic fields.

**Radio sources** The X-ray source 3A1909+05, with optical counterpart SS 433, is located in a shell of radio emission. The optical and X-ray spectra of this source show emission lines from a jet with velocity  $v \approx 0.26c$ , which precesses in about 165 days. The jet is detected directly in Very Long Baseline Interferometry radio observations. It is not clear whether the X-ray source is a neutron star

or a black hole. Cyg X-3 has a 4.8 hr orbital period and was classified as a low-mass X-ray binary, until an infrared spectrum was obtained which shows the strong and broad Balmer emission lines characteristic of a Wolf Rayet star. Cyg X-3 has a double radio jet. Cir X-1 is another X-ray source with a radio jet, and is remarkable for the sudden, extreme surges of the X-ray flux, possibly related to the periastron passage of the donor star.

#### 19.2.4 Binary radio pulsars

Since 1975, an increasing number of radio pulsars have been discovered in binaries. Two of these pulsars have a companion which is a massive O or B star. Most of the others have a companion believed to be a neutron star or a white dwarf. The pulsars in these other binaries are called recycled radio pulsars, and are generally characterized by short pulse periods,  $P \gtrsim 1.5$  ms, and very low period derivatives,  $P/\dot{P} \gtrsim 10^8$  yr, as compared to the pulse periods and period derivatives of ordinary radio pulsars, which have  $P \sim 1$  s and  $P/\dot{P} \lesssim 10^7$  yr.

The pulse periods of binary radio pulsars vary with the orbital motion, which provides an indication of the mass of its companion. In six close binaries with two neutron stars, and one binary with a white dwarf and a neutron star, general relativistic effects allow accurate mass determinations. In some binaries, the companion to the recycled pulsar has a mass  $M_c \gtrsim 1 M_\odot$ , and – with one exception – these orbits are eccentric. In the other binaries the mass of the companion is lower,  $M_c \sim 0.2 M_\odot$ , and the orbits are (almost perfectly) circular. As we will see, the first are thought to have evolved from high-mass X-ray binaries, the latter from low-mass X-ray binaries.

# Chapter 20

## Non-conservative evolution processes

The existence of white dwarfs and neutron stars in very close binaries, with orbital periods often much less than a day, cannot be understood in the context of the mass transfer processes discussed so far. The formation of such *compact binaries* requires the initial orbit to be wide enough for the progenitor of the compact object to expand to red giant dimensions, so the orbit must have shrunk considerably, by one or two orders of magnitudes. This requires a very substantial loss of orbital energy and angular momentum. The process presumably responsible for this is known as *common-envelope evolution*, and was originally proposed in 1976 by B. Paczyński as an explanation for the existence of white dwarfs in very short-period binaries, such as the cataclysmic variables and related binaries (Sect. 19.1).

Once a very close binary is formed, further angular momentum loss from the orbit can occur by the processes of gravitational radiation and magnetic braking. This can bring a detached compact binary into a semi-detached or contact state, and also drive mass transfer in these systems.

### 20.1 Common-envelope evolution

Two different circumstances can cause the companion of an evolved donor star to find itself engulfed by the envelope of the donor. The first situation arises from the Darwin instability of tidal interaction discussed in Sect. 16.1. As the donor star evolves and expands, if at the same time its rotation is locked to the orbit by tidal friction, it needs to spin up by extracting angular momentum from the orbit. When the spin angular momentum of the donor exceeds  $\frac{1}{3}$  times the orbital angular momentum, a stable binary orbit is no longer possible and the stars spiral towards each other by tidal forces until the companion plunges into the donor's envelope. For the instability to take effect the condition  $J_{\text{rot}} > \frac{1}{3}J_{\text{orb}}$  must be met before the donor star fills its Roche lobe. This requires a large mass ratio  $M_d/M_a$  of donor mass to companion mass. Assuming co-rotation to be maintained until the instability starts, and writing the moment of inertia of the donor as  $I = r_g^2 M_d R_d^2$ , the condition translates into (see Exercise 20.1):

$$(1 + q) r_{L,d}^2(q) > \frac{1}{3r_g^2} \quad \text{with } q = M_d/M_a \quad (20.1)$$

where  $r_{L,d} = R_L/a$  is the relative Roche-lobe size of the donor (eq. 15.17). For a typical value  $r_g^2 \approx 0.1$  this implies the instability occurs for  $M_d/M_a \gtrsim 9$ .

The second circumstance is dynamically unstable Roche-lobe overflow, which ensues when the donor cannot shrink fast enough to stay within its Roche lobe (mode 3 in Sect. 17.3). This is expected for a large range of binary parameter space. When the donor star has a deep convective envelope (i.e.

it is on the giant branch, late case B and case C), mass transfer will be dynamically unstable unless the donor has already lost enough mass to become less massive than its companion. When the donor still has a radiative envelope (it is in the Hertzsprung gap, early case B) dynamically unstable mass can be expected if the donor is more massive than its companion by a factor  $\gtrsim 4$ . The ensuing common envelope phase should therefore be a very common occurrence in binary evolution.

Once the companion is inside the donor's envelope, the friction between the motion of the companion and the envelope removes angular momentum from the orbital motion, and releases energy. Thus, the orbit shrinks, and the envelope is brought into rotation and heated. This process continues until enough energy is added to the envelope to expel it. Alternatively, the companion star may spiral-in until it merges with the core of the mass donor. Because observational counterparts are very rare, the common envelope must be a transient phase with a short lifetime,  $\lesssim 10^3$  years. The short timescale implies that the companion is unlikely to accrete a significant amount of mass from the envelope, and usually the companion mass is assumed to remain constant.

The outcome of a common envelope is often estimated based on the picture of conversion of orbital energy into binding energy of the envelope, which may or may not be thrown off eventually depending on how much orbital energy is available. We can measure the efficiency of the CE process as

$$\alpha_{\text{CE}} = \frac{\Delta E_{\text{bind}}}{\Delta E_{\text{orb}}} \quad (20.2)$$

where

$$\Delta E_{\text{orb}} = \frac{GM_a M_{c,d}}{2a_f} - \frac{GM_a M_d}{2a_i}, \quad (20.3)$$

where  $a_i$  and  $a_f$  are the initial and final semi-major axis and  $M_{c,d}$  is the core mass of the donor.  $\Delta E_{\text{bind}}$  is estimated as the binding energy of the envelope at the start of the CE process, i.e. as the binding energy of the donor envelope when it first fills its Roche lobe<sup>1</sup>:

$$\Delta E_{\text{bind}} = \int_{M_{c,d}}^{M_d} \left( \frac{Gm}{r} - u \right) dm \quad (20.4)$$

$$\equiv \frac{GM_d M_{\text{env},d}}{\lambda R_{L,d}}, \quad (20.5)$$

with  $M_{\text{env},d} = M_d - M_{c,d}$ . The last equality defines the dimensionless parameter  $\lambda$ , which is a measure of the relative density distribution within the envelope, and of the contribution of internal energy ( $u$  is the internal energy per unit mass) to the binding energy. We can then formally compute the ratio of final to initial separation as

$$\frac{a_f}{a_i} = \frac{M_{c,d}}{M_d} \frac{M_a}{M_a + 2M_{\text{env},d}/(\alpha_{\text{CE}}\lambda r_{L,d})} \quad (20.6)$$

where  $r_{L,d} = R_{L,d}/a_i$  is the relative Roche-lobe size of the the donor at the start of the CE, which depends on the mass ratio  $M_d/M_a$ . In most situations the second term in the denominator of eq. (20.6) dominates over the first term, in which case we can simplify the equation to

$$\frac{a_f}{a_i} \approx \frac{1}{2}\alpha_{\text{CE}}\lambda r_{L,d} \frac{M_{c,d}M_a}{M_d M_{\text{env},d}}. \quad (20.7)$$

The outcome of the common envelope phase is seen to depend on the product  $\alpha_{\text{CE}}\lambda$ . The parameter  $\lambda$  can be calculated from a stellar structure model of the star at the moment it fills its Roche lobe.

---

<sup>1</sup>Note that some authors, e.g. Iben & Livio (1993), assume that the envelope has already expanded to a radius of  $2a_i$  when the CE phase starts.

This can be done with reasonable accuracy, the main uncertainty being the exact boundary between the core and the envelope that will be ejected.

Two approaches have been taken to determine the efficiency parameter  $\alpha_{\text{CE}}$  of the common envelope process. Theoretically,  $\alpha_{\text{CE}}$  can be calculated from a three-dimensional hydrodynamic calculation of the spiral-in process. Much effort has gone into such calculations, which are very challenging owing to the enormous range of spatial and temporal scales involved, especially in the late phase of a common envelope. Realistic calculations must also include the effects of turbulence and radiative transfer, which is not yet feasible. The limited 3D hydrodynamical calculations done so far (which do not include the entire process from start to end) indicate values of  $\alpha_{\text{CE}} < 1$ . These results should not be taken too literally yet. In particular the calculations do not take into account that, once the envelope has been spun up and the spiral-in has slowed down sufficiently, additional energy sources may aid in ejecting the envelope, such as nuclear power, accretion power or dynamical energy in envelope pulsations.

Another approach is to determine  $\alpha_{\text{CE}}$  observationally. Central binaries of planetary nebulae are very good objects for such a study, because the 'smoking gun' of the nebula shows that such binaries have only just emerged from a common envelope, i.e. they represent the conditions immediately following the spiral-in. The determination goes as follows. If the white dwarf is of low mass,  $\lesssim 0.45 M_{\odot}$ , it must have formed as the helium core of a low-mass star on the red giant branch, which obeys a core-mass radius relation (Sect. 15.2.3). The relation between the donor mass and its core mass can be roughly approximated by a power law for  $M_{\text{c,d}} \lesssim 0.45 M_{\odot}$ ,

$$\frac{R_d}{R_{\odot}} \approx 3500 \left( \frac{M_{\text{c,d}}}{M_{\odot}} \right)^4. \quad (20.8)$$

The mass of the white dwarf thus more or less fixes the size of the Roche lobe at the onset of the common envelope, such that the ratio  $a_f/a_i$  can be determined from observed quantities. Applying eq. (20.6) to systems with a low-mass white dwarf and a main-sequence or other white-dwarf companion shows that  $\alpha_{\text{CE}}$  is in the range 0.2 to 1.

However, it has become clear that not all binaries for which dynamically unstable mass transfer is expected undergo spiral-in. Several symbiotic binaries and barium-star binaries have periods of a few hundred days, too short to have avoided unstable Roche-lobe overflow but too long to have experienced strong spiral-in. Furthermore, if one applies the technique described above in combination with eq. (20.6) to the first white dwarf formed in a double white-dwarf binary, one often finds *negative* values of  $\alpha_{\text{CE}}$ ! The masses of the white dwarfs in such systems are often very similar, which means (again applying the core-mass radius relation) that the separation did not change drastically between the formation of the first and the second white dwarf (Nelemans et al., 2000). This is not expected from either stable conservative mass transfer (which expands the orbit) or spiral-in. It appears that some binaries for which a common envelope is expected are capable of ejecting the envelope without strong orbital energy and angular momentum losses. How this process works is not understood. Additional energy sources are needed, such as nuclear energy, but this requires much longer timescales than the  $\lesssim 10^3$  years normally associated with a common envelope.

## 20.2 Orbital angular momentum loss in close binaries

In short-period binaries, either primordial (in the case of two low-mass main-sequence stars) or formed after a common-envelope phase (with one of the stars a compact object), angular momentum loss from the orbit can bring the stars even closer together. Two important processes contribute to such angular momentum loss, which can cause a detached binary to evolve into a semi-detached or contact binary, and also drive mass transfer in these systems.

### 20.2.1 Gravitational radiation

According to general relativity, the changing quadrupole moment of the orbiting bodies in a binary system produces gravitational waves that carry energy and angular momentum. It is thus inevitable that a binary loses energy and angular momentum due to gravitational radiation, and this process can become significant if the orbit is sufficiently close. Defining

$$\tau_{\text{GR}} \equiv \frac{5c^5}{32G^3} \frac{a^4}{M_1 M_2 (M_1 + M_2)}, \quad (20.9)$$

the loss of orbital angular momentum and orbital energy via gravitational radiation, averaged over the orbit, may be written as

$$\frac{\dot{J}}{J} = -\frac{1}{\tau_{\text{GR}}} \frac{1 + \frac{7}{8}e^2}{(1 - e^2)^{5/2}}, \quad (20.10)$$

$$\frac{\dot{E}}{E} = \frac{2}{\tau_{\text{GR}}} \frac{1 + \frac{73}{24}e^2 + \frac{37}{96}e^4}{(1 - e^2)^{7/2}}. \quad (20.11)$$

(Note that  $\dot{E}$  is negative because  $E < 0$ .) In a detached binary, where the masses are constant, (20.11) directly yields the change in semi-major axis; (20.10) then gives the change in eccentricity:

$$\frac{\dot{a}}{a} = -\frac{\dot{E}}{E} \quad \text{and} \quad \frac{\dot{e}}{e} = -\frac{1}{\tau_{\text{GR}}} \frac{\frac{19}{6} + \frac{121}{96}e^2}{(1 - e^2)^{5/2}}. \quad (20.12)$$

Thus, gravitational radiation tends to circularize the orbit on roughly the same timescale as it causes the orbit to shrink.

We see that  $\tau_{\text{GR}}$  is the typical timescale of angular momentum loss for (nearly) circular orbits, in which case the  $e$ -dependent factors in (20.10) and (20.11) become unity. Using Kepler's third law (20.9) can also be written as

$$\tau_{\text{GR}} = 376.8 \frac{(1+q)^2}{q} \left(\frac{P}{d}\right)^{8/3} \left(\frac{M_1 + M_2}{M_\odot}\right)^{-5/3} \text{Gyr}. \quad (20.13)$$

The strong dependence on the size of the orbit ( $\tau_{\text{GR}} \propto a^4$  or  $P^{8/3}$ ) means that this process is only effective in very close binaries: for approximately solar-mass stars,  $\tau_{\text{GR}}$  becomes comparable or shorter than the Hubble time if  $a \lesssim 2R_\odot$ , or  $P \lesssim 0.3$  d. This is the case for many of the compact-object binaries discussed, for example, in Sec. 19.1. For a circular orbit with initial period  $P_0$ , the period decreases to zero in a time  $\tau_{\text{GR}}(P_0)/8$ . This is the timescale on which a detached binary consisting of two compact objects (with  $R \ll a$ ) will merge. If the orbit is quite eccentric, the timescale for gravitational radiation can be substantially shorter than (20.13), as the  $e$ -dependent factors in (20.10)–(20.12) are then  $> 1$ . Therefore also the time it takes for a binary with a certain  $P$  to merge is shorter in an eccentric orbit, e.g. for  $e = 0.7$  the merger timescale is only about 10% of the value at  $e = 0$ .

### 20.2.2 Magnetic braking

As discussed in Sec. 14.5.2, low-mass single stars show signs of magnetic activity, and their rotation is observed to slow down with age. This is interpreted as loss of angular momentum via *magnetic braking*. If an (almost) Roche-lobe filling star in a close binary loses angular momentum in this way, it will not be able to rotate slower, as it is kept in co-rotation with the orbit by tidal forces. Thus loss of angular momentum is transferred from the donor rotation to the orbital revolution, i.e. the binary as a whole loses angular momentum.

Based on the Skumanich relation between rotation velocity and age of solar-type stars, we found in Sec. 14.5.2 that the angular-momentum loss of such a star should be (Eq. 14.31):

$$\dot{J} \approx -4 \times 10^{-29} \text{ s/cm}^2 \times r_g^2 M R^4 \Omega^3 \quad (\text{in cgs units}), \quad (20.14)$$

with  $\Omega$  the rotational angular velocity. In a tidally locked binary,  $\Omega$  equals the orbital angular frequency  $\omega = 2\pi/P$ . Using (20.14) and Kepler's third law we can then write the *orbital* angular momentum loss due to magnetic braking from star 1 as

$$\frac{\dot{J}}{J} \approx -4 \times 10^{-29} \text{ s/cm}^2 \times r_g^2 \frac{G(M_1 + M_2)^2}{M_2} \frac{R_1^4}{a^5}. \quad (20.15)$$

The angular momentum loss due to magnetic braking can thus be seen to increase with decreasing separation, due to its dependence on the stellar rotation rate. In a semi-detached binary where  $R_1 = R_{L,1} \propto a$ , this formula predicts a timescale for angular momentum loss by magnetic braking  $\tau_{\text{MB}} = -J/\dot{J} \propto a$ ; a much weaker dependence on  $a$  than for the timescale for gravitational radiation (20.9). Thus, in close binaries containing low-mass main-sequence stars, magnetic braking may dominate at relatively large separations, whereas gravitational radiation may dominate in the closest orbits.

Note, however, that the Skumanich relation on which (14.31) and (20.15) are based was derived for slowly rotating, solar-like stars. It is not clear if stars with different masses and radii follow the same relation. Therefore, the dependence on  $M$  and  $R$  of the angular-momentum loss rate is very uncertain. Different magnetic braking laws have been considered in the literature, either empirical or based on more physical considerations of stellar dynamos and magnetic winds, in which the mass and radius dependence varies between  $M^{-0.5\dots 1}$  and  $R^{0\dots 4}$ . When applied to binaries containing low-mass stars, these give angular-momentum loss rates that can differ by orders of magnitude. Moreover, (20.14) relies on extrapolating the Skumanich relation to much faster rotation rates than it has been measured for (up to about 30 km/s). Recent indications are that the magnetic field generated by stellar dynamos saturates at  $\Omega \gtrsim 10\Omega_\odot$ , and therefore magnetic braking could be (much) weaker at the rotation rates found in close binaries than implied by (20.15).

### 20.3 Evolution of compact binaries

By combining Kepler's law (15.14) with an expression for the Roche-lobe radius (15.18), we get an approximate relation between the orbital period and the mass and radius of the Roche-lobe-filling star (see Exercise 15.4):

$$P_{\text{orb}} \approx 0.35 \text{ d} \left( \frac{R_d}{R_\odot} \right)^{3/2} \left( \frac{M_d}{M_\odot} \right)^{-1/2} \left( \frac{2}{1+q} \right)^{0.2} \approx 9.6 \text{ hr} \left( \frac{R_d}{R_\odot} \right)^{3/2} \left( \frac{M_d}{M_\odot} \right)^{-1/2} (1+q)^{-0.2} \quad (20.16)$$

For low-mass donors, when  $q = M_a/M_d \lesssim 0.7$ , we can ignore the weak dependence on the mass ratio. Thus, by assuming a mass-radius relation for the donor star, we may determine its mass from the observed orbital period, as summarized in Table 20.1 for different types of donor.

Cataclysmic variables and low-mass X-ray binaries (see Ch. 19) with orbital periods between 80 min and 10 h may have main-sequence donors with masses between  $0.1M_\odot$  and  $1.0M_\odot$ , according to Table 20.1. The evolutionary time scales of such low-mass stars are very long. Since these donor masses are smaller than the mass of the accreting compact object, the orbit of such a binary expands when mass is transferred conservatively from the donor (see eq. 17.3). Unless the donor star expands more than its Roche lobe, this expansion will put an end to the mass transfer. Therefore, angular momentum must be lost from the binary to keep mass transfer going, by one or both of the processes discussed in Sect. 20.2.

In stable mass transfer, the radius of the donor equals the radius of the Roche lobe at all times in this process, so that  $R_L = R_d$  and  $\dot{R}_L = \dot{R}_d$ . Treating both  $R_d$  and  $R_L$  as dependent on the variables  $M_d$  and  $t$ , we can write the logarithmic rate of change  $d \ln R/dt = \dot{R}/R$  of these radii as

$$\frac{\dot{R}_d}{R_d} = \left( \frac{\partial \ln R_d}{\partial t} \right)_{M_d} + \zeta_d \frac{\dot{M}_d}{M_d} \quad \text{and} \quad \frac{\dot{R}_L}{R_L} = \left( \frac{\partial \ln R_d}{\partial t} \right)_{M_d} + \zeta_L \frac{\dot{M}_d}{M_d}. \quad (20.17)$$

The first term in both equations expresses the intrinsic change in radius, due internal evolution (in case of the donor star) or due to the loss of orbital angular momentum (in case of the Roche radius). The second term represents the radius change resulting from mass-transfer, where we have used the mass-radius exponents defined in Sect. 17.3. If the donor remains in thermal equilibrium during mass transfer, then  $\zeta_d = \zeta_{\text{eq}}$ . The term  $(\partial \ln R_L/\partial t)_{M_d} = \dot{a}/a = 2\dot{J}/J$ , according to eq. (17.2) in the absence of mass transfer. Thus we can derive the mass transfer rate  $\dot{M}_d$  as (remembering that  $\dot{M}_d$  is negative)

$$\frac{\dot{M}_d}{M_d} = -\frac{1}{\zeta_d - \zeta_L} \left[ \left( \frac{\dot{R}_d}{R_d} \right)_{M_d} - 2 \frac{\dot{J}}{J} \right] \quad (20.18)$$

This equation shows that mass transfer may be driven by loss of angular momentum from the binary ( $\dot{J} < 0$ ), or by expansion of the donor star ( $\dot{R}_d > 0$ ) due to, for example, the ascent of the donor on the (sub)giant branch, or due to irradiation of the donor. Here we discuss the first possibility, which applies in particular to cataclysmic variables.

By equating the loss of angular momentum with that expected from gravitational radiation (20.10) or from magnetic braking (e.g. 20.15), we may use eq. (20.18) to calculate the evolution of a cataclysmic variable or a low-mass X-ray binary. Mass-transfer rates can be calculated in this way for main-sequence stars, with  $\zeta_{\text{eq}} = 1$ , and for white-dwarf donor stars, with  $\zeta_{\text{eq}} = -1/3$ . If we assume the total mass of the binary to be conserved, then  $\zeta_L$  is given by (17.22). The results are shown in Figure 20.1, for angular momentum loss due to the emission of gravitational radiation only (eq. 20.10), and for the four types of donors given in Table 20.1, i.e. stars on the main sequence, stars on the helium main sequence, and both H-rich and H-free degenerate (white dwarf) donors.

For stars on the main sequence, the mass-transfer rate is about  $\dot{M} \approx 10^{-10} M_\odot/\text{yr}$ , for donor masses between 0.2 and 1  $M_\odot$ . The mass-transfer rate depends only weakly on the mass of the accreting star. Stars on the helium main sequence are smaller, and fill their Roche lobes in more compact binaries, leading to higher mass-transfer rates. Consider a main-sequence donor star. The mass transfer causes this star to become less massive, and the binary thus evolves towards shorter periods. At some point, the mass of the donor becomes too small to sustain significant hydrogen burning, and the core becomes degenerate. At this point, which is reached for a donor mass of about  $0.08M_\odot$ , further mass loss of the donor causes it to expand. The orbit expands with it, according to

**Table 20.1.** Mass-radius relations and derived mass-orbital-period relations for semi-detached compact binaries. Valid for donors in thermal equilibrium.

| donor                     | mass-radius relation                              | $\zeta_{\text{eq}}$ | period-mass relation   |
|---------------------------|---|---------------------|--|
| low-mass MS star          | $R_d/M_\odot \approx M_d/M_\odot$                 | $\approx 1$         | $P_{\text{orb}} \approx 9.6 \text{ hr} (M_d/M_\odot)$        |
| low-mass He-MS star       | $R_d/M_\odot \approx 0.2 (M_d/M_\odot)$           | $\approx 1$         | $P_{\text{orb}} \approx 0.86 \text{ hr} (M_d/M_\odot)$       |
| low-mass WD ( $X = 0.7$ ) | $R_d/M_\odot \approx 0.028 (M_d/M_\odot)^{-1/3}$  | $-\frac{1}{3}$      | $P_{\text{orb}} \approx 2.7 \text{ min} (M_d/M_\odot)^{-1}$  |
| low-mass WD ( $X = 0$ )   | $R_d/M_\odot \approx 0.0115 (M_d/M_\odot)^{-1/3}$ | $-\frac{1}{3}$      | $P_{\text{orb}} \approx 0.72 \text{ min} (M_d/M_\odot)^{-1}$ |

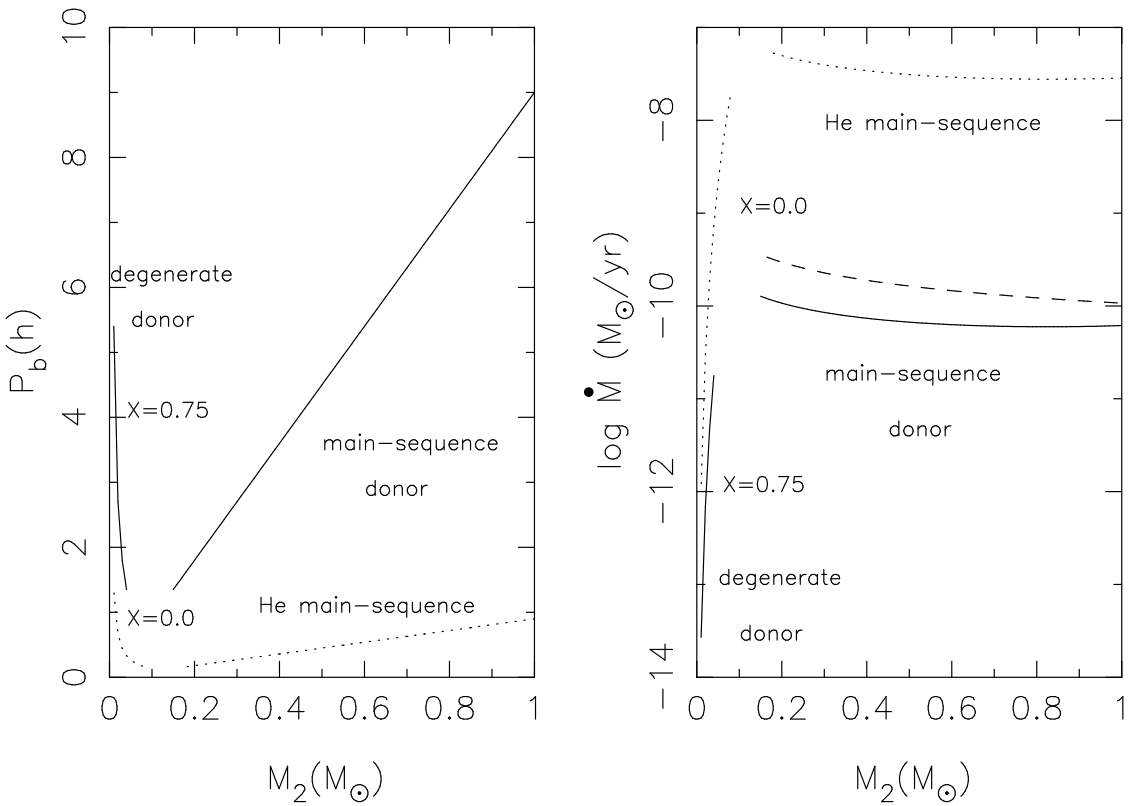


**Figure 20.1.** Orbital period and mass-transfer rate as a function of donor mass  $M_2$ , for binary evolution driven by loss of angular momentum via gravitational radiation. For main-sequence donors (shown for  $M_2 > 0.15 M_\odot$ ; solid and dashed line for stars on the hydrogen and helium main sequence, respectively) the orbital period decreases and the mass-transfer rate hardly changes, as the donor mass decreases. For degenerate donors (shown for  $M_2 < 0.1 M_\odot$ ; solid and dashed lines for the indicated values of the hydrogen abundance) the orbital period increases and the mass-transfer rate drops precipitously, as the donor mass decreases. The mass-transfer rates shown all assume  $M_1 = 1.4 M_\odot$ , except for the dashed line, which assumes that the mass receiver is a  $7 M_\odot$  black hole. Figure from Verbunt (2013).

(20.16). Thus, the evolution of the orbital period passes through a minimum. Detailed calculations show that this minimum may be identified with the cutoff at around 80 min observed in the period distribution of cataclysmic variables. A similar line of reasoning shows that binaries with donors that initially burn helium must also show a minimum period, which detailed calculations put at around 10 min.

Many cataclysmic variables with orbital periods of a few hours have inferred mass-transfer rates of the order of  $10^{-9} M_\odot/\text{yr}$ , much higher than expected from a main-sequence donor if angular-momentum loss occurs by gravitational radiation alone (Fig. 20.1). As suggested by eq. (20.18), any additional mechanism of angular-momentum loss increases the mass-transfer rate, and this has been one of the main reasons to investigate mechanisms such as magnetic braking. The rate of angular momentum loss implied by eq. (20.15) is sufficiently high to explain the high observed values for mass-transfer rates in cataclysmic variables and low-mass X-ray binaries. Magnetic braking has also been invoked to explain the so-called *period gap* in the cataclysmic variable period distribution: the relative paucity of systems with orbital periods between about 2 and 3 hours. These period values correspond roughly to the mass at which a main-sequence star changes its structure from being completely convective ( $M \lesssim 0.3 M_\odot$ ) to having a convective envelope and a radiative core (at larger

masses). The high mass-transfer rate driven by magnetic braking at  $P > 3$  hr removes mass fast enough for the donor to be out of thermal equilibrium and thus to have a radius larger than its equilibrium main-sequence radius. The idea is that when the mass is reduced so much that the radiative core disappears and the donor becomes completely convective, magnetic braking stops operating or is strongly reduced in strength. The rate of mass transfer then drops, and the star shrinks back to its equilibrium radius. The binary remains detached until gravitational radiation has shrunk the orbit such that the donor again fills its Roche lobe, at  $P \approx 2$  hr. Mass transfer then resumes and the binary reappears as a cataclysmic variable.

While magnetic braking is an attractive possibility to explain the mass-transfer rates and the period gap in cataclysmic variables with main-sequence-like donor stars, the details and actual efficiency of this process are not well understood. Therefore, the importance of magnetic braking in driving mass transfer in compact binaries has not been well-established.

## Exercises

- 20.1** Derive the condition on the mass ratio (20.1) for the Darwin instability to occur before the donor star fills its Roche lobe. Estimate the value of the critical mass ratio for polytropic stellar models with  $n = 3$ , with  $r_g^2 = 0.076$ ; and  $n = 1.5$ , with  $r_g^2 = 0.21$ .

## Chapter 21

# Origin and evolution of neutron-star and black-hole binaries

The formation of a neutron star or black hole in a binary requires the explosion of a massive star in a supernova. This causes sudden mass loss from the binary and likely also imparts a kick velocity to the remaining compact object. We will therefore start this chapter by examining the effect of a SN explosion on the orbit. The possibility of supernova kicks introduces a major uncertainty in the evolution of binaries containing neutron stars and black holes.

*N.B. Most of this chapter is adapted from lecture notes on Binary Stars by F. Verbunt.*

### 21.1 Mass loss in a supernova explosion

During a supernova the envelope of the exploding star is expelled with a velocity of order  $10^4$  km/s. The sudden loss of the envelope mass,  $\Delta M$ , changes the binary parameters. To estimate this effect in a simple way, it is often assumed that the explosion is instantaneous, and that the position and velocities of the stars are the same after the explosion as before the explosion. If the explosion occurs in a circular orbit, this implies that the distance  $a_i$  between the two stars before the explosion is the periastron distance after the explosion

$$a_i = (1 - e)a_f \quad (21.1)$$

and that the periastron velocity of the new orbit (15.13) is the same as the orbital velocity in the pre-supernova orbit:

$$\frac{G(M_1 + M_2)}{a_i} = \frac{G(M_1 + M_2 - \Delta M)}{a_f} \frac{1 + e}{1 - e} \quad (21.2)$$

Substituting (21.1) in (21.2) gives the eccentricity of the post-supernova orbit:

$$e = \frac{\Delta M}{M_1 + M_2 - \Delta M} \quad (21.3)$$

We see that the binary is disrupted ( $e > 1$ ) when more than half of the total mass is lost in the explosion, i.e. when  $\Delta M > (M_1 + M_2)/2$ .

Because of the mass loss, the velocity of the center of mass of the binary changes by  $v_{CM}$ , given by

$$v_{CM} = \frac{M_2 v_2 - (M_1 - \Delta M) v_1}{M_1 + M_2 - \Delta M} = e v_1 \quad (21.4)$$

where  $v_i$  is the orbital velocity of the star with mass  $M_i$  before the explosion. Massive binaries initially have small velocities; thus  $v_{\text{CM}}$  is a good estimate for the system velocity of the binary after the supernova explosion.

If the orbit after the explosion is sufficiently small, it may be circularized by tidal interaction. From conservation of angular momentum, the radius  $a_c$  of the circular orbit can be written in terms of the semi-major axis of the eccentric orbit, or of the radius of the pre-supernova orbit

$$a_c = (1 - e^2)a_f = (1 + e)a_i \quad (21.5)$$

In reality, the correctness of the assumptions made to derive eqs. (21.1–21.5) is rather doubtful. Wide binaries are expected to have initially eccentric orbits. And from measurements of velocities of single radio pulsars, it appears that a single neutron star may receive an appreciable kick velocity at its birth, of several hundred km/s. It may be expected that a neutron star formed in a binary will also obtain a kick velocity at birth. This velocity can have an arbitrary direction and its effect on the orbit is therefore unpredictable. The presence of kick velocities introduces a major uncertainty in the evolution of a binary in which one star undergoes a supernova explosion.

### 21.1.1 Supernova explosion in an eccentric orbit

In an eccentric orbit, the relative velocity of the two stars when their distance to one another is  $r$  is given by (15.12):

$$v^2 = G(M_1 + M_2) \left( \frac{2}{r} - \frac{1}{a} \right) \quad (21.6)$$

Denote the supernova progenitor mass with  $M_1$ , and the pre-explosion semi-major axis with  $a$ , and combine eq. (21.6) with a similar equation for the post-explosion orbit, with a compact star of mass  $M_{1f} = M_1 - \Delta M$  and semi-major axis  $a_f$ . The instantaneous position  $r$  is not changed by the explosion, so we may write the ratio  $a/a_f$  as

$$\frac{a}{a_f} = \frac{2a}{r} - \left( \frac{v_f}{v} \right)^2 \frac{M_1 + M_2}{M_{1f} + M_2} \left( \frac{2a}{r} - 1 \right) \quad (21.7)$$

where  $v_f$  is the relative velocity between the two stars immediately after explosion.

The binary will be disrupted if the right hand side of eq. (21.7) is zero, which is the case for

$$\frac{r_d}{2a} = 1 - \left( \frac{v}{v_f} \right)^2 \frac{M_{1f} + M_2}{M_1 + M_2}. \quad (21.8)$$

$r$  must be on the pre-explosion orbit, i.e.  $1 - e < r/a < 1 + e$ , with  $e$  the eccentricity of the pre-explosion orbit. Therefore, if the value for  $r_d/a$  found with eq. (21.8) is less than  $1 - e$ , e.g. when virtually no mass is lost, then the binary remains bound at all pre-explosion radii. If it is larger than  $1 + e$ , e.g. when virtually all mass is lost, then the binary is disrupted at all radii.

For intermediate values of  $r_d/a$ , the binary will be disrupted at all  $r < r_d$ , and thus the probability that this will happen is given by the fraction of the time that  $r < r_d$  in the binary orbit. We calculate this fraction by writing  $r$  in terms of the eccentric anomaly  $\mathcal{E}$  (e.g. see Verbunt, 2013, Sec. 2.2.2)

$$r = a(1 - e \cos \mathcal{E}) \quad (21.9)$$

The eccentric anomaly may be related to the mean anomaly  $\mathcal{M}$ , which progresses linearly with time, via the equation of Kepler

$$\mathcal{M} = \mathcal{E} - e \sin \mathcal{E} \quad (21.10)$$

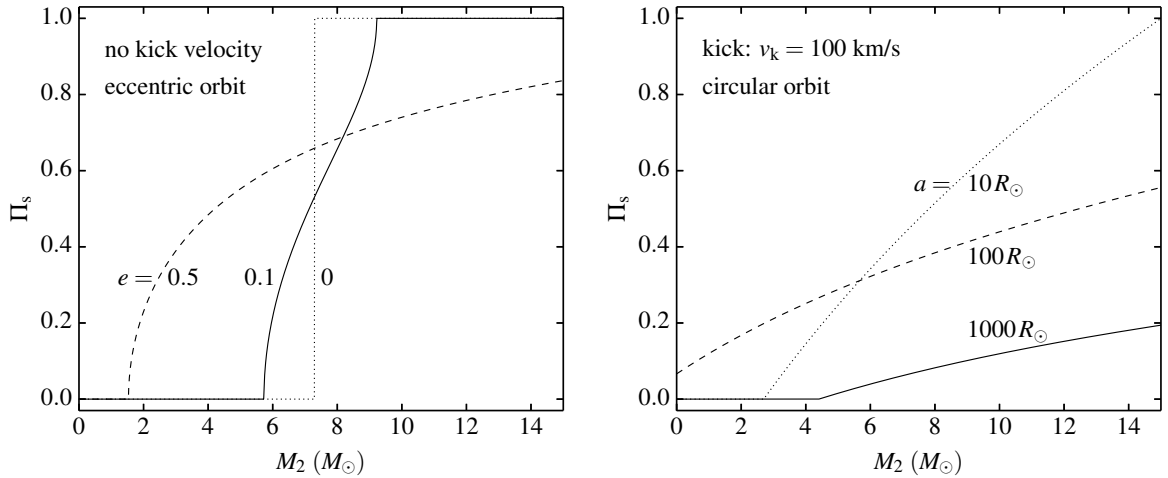


**Figure 21.1.** The probability  $\Pi_s$ , as a function of the mass  $M_2$  of the non-exploding star, that a binary system remains bound after a supernova explosion in which a  $10 M_\odot$  star leaves a  $1.35 M_\odot$  neutron star. (*left*) Symmetric explosion in an eccentric orbit with  $e = 0.5$  (dashed line),  $e = 0.1$  (solid line) and  $e = 0$  (circular, dotted line). (*right*) The neutron star receives a kick velocity of  $v_k = 100 \text{ km/s}$  in a circular orbit, with  $a = 10 R_\odot$  (dotted line),  $100 R_\odot$  (dashed line) and  $1000 R_\odot$  (solid line).

To calculate the probability that the supernova will dissolve the binary, we start by calculating  $r_d/a$  with eq. (21.8), and check whether  $1 - e < r_d/a < 1 + e$ . If so, we continue by calculating the eccentric anomaly  $\mathcal{E}_d$  corresponding to  $r_d$  with eq. (21.9), and find the probability that the binary will be disrupted as the probability that the two stars are found at an  $r$  between periastron and  $r_d$  from eq. (21.10) as

$$\Pi_d = \frac{\mathcal{E}_d - e \sin \mathcal{E}_d}{\pi} \quad (21.11)$$

In Fig. 21.1 the probability of survival,  $\Pi_s \equiv 1 - \Pi_d$  is illustrated for a binary in which a  $10 M_\odot$  star explodes to leave a  $1.35 M_\odot$  neutron star, and where the velocity is unchanged:  $v_f = v$ , as a function of the companion mass  $M_2$ . For an initially circular orbit, eq. (21.9) shows that the binary is always disrupted for  $M_2 < M_{2\text{crit}} = 7.32 M_\odot$ , and always remains bound for  $M_2 > M_{2\text{crit}}$  (dotted line). For an initial orbit with eccentricity  $e = 0.5$ , we find that there is a finite probability that the binary survives down to very low companion masses, or that it is disrupted up to relatively high companion masses. The lowest possible companion mass for which the binary can remain bound is found by equating the pre-explosion velocity at apastron (eq. 15.13) to the escape velocity after the explosion, at the same position:

$$v^2 = \frac{G(M_1 + M_2)(1 - e)}{a(1 + e)} = \frac{2G(M_{1f} + M_2)}{a(1 + e)} \quad \Rightarrow \quad M_2 = \frac{(1 - e)M_1 - 2M_{1f}}{1 + e} \quad (21.12)$$

For the example shown in Fig. 21.1 this minimum mass is  $M_2 = 1.53 M_\odot$ . Thus, in the absence of velocity kicks, even very low-mass stars have a finite probability of surviving the supernova explosion of their companion – after all, in an eccentric orbit more time is spent near apastron than near periastron. Note that these results are independent of the initial semi-major axis  $a$  of the binary.

### 21.1.2 Supernova with velocity kick

The calculations that we just discussed would lead to the conclusion that there could be many wide binaries in which a neutron star is accompanied by a low-mass companion, i.e. many radio pulsars

would have an optical counterpart. As this appears not to be the case, we must conclude that most neutron stars acquire a kick velocity  $v_k$  at birth, which is added to the pre-explosion orbital velocity:

$$v_f^2 = v^2 + v_k^2 + 2vv_k \cos \theta \equiv (1 + f^2 + 2f \cos \theta)v^2 \quad (21.13)$$

where  $\theta$  is the angle between the kick velocity and the orbital velocity before explosion, and where we have written the kick velocity in units of the pre-explosion velocity,  $v_k \equiv fv$ . This equation may be entered into eq. (21.8) to check whether the supernova explosion dissolves the binary in the presence of a kick.

To illustrate the effect of a kick we consider an explosion in a circular orbit. The binary remains bound if the post-explosion velocity is less than the escape velocity:

$$(1 + f^2 + 2f \cos \theta) \frac{G(M_1 + M_2)}{a} \leq \frac{2G(M_{1f} + M_2)}{a} \Rightarrow \quad (21.14)$$

$$\cos \theta \leq \cos \theta_{\text{crit}} \equiv \frac{1}{2f} \left[ \frac{2(M_{1f} + M_2)}{M_1 + M_2} - 1 - f^2 \right] \quad (21.15)$$

The probability for this to happen is given by the probability that  $\theta \geq \theta_{\text{crit}}$ , which for arbitrary direction of the kick is given by

$$\Pi_s = \frac{\int_{\theta_{\text{crit}}}^{\pi} \sin \theta d\theta}{\int_0^{\pi} \sin \theta d\theta} = \frac{1 + \cos \theta_{\text{crit}}}{2} \quad (21.16)$$

and may be found directly from eq. (21.15).

Fig. 21.1 shows the effect of a kick velocity  $v_k = 100$  km/s in circular orbits of increasing size. In tight orbits with  $v \gg v_k$ , the supernova kick has relatively little effect and binaries with low-mass companions will always be disrupted. In orbits with  $v \sim v_k$ , however, a kick directed opposite to the orbital motion can keep a very low-mass companion bound. In wide orbits, the kick will again disrupt all binaries with low-mass companions, and results in a lower survival probability for all companion masses.

## 21.2 Formation and evolution of high-mass X-ray binaries

The observed presence of a neutron star in a binary poses the following problem. According to the theory of stellar evolution, it is always the more massive star in a binary that explodes first as a supernova. According to eq. (21.3) this means that the binary is disrupted ( $e > 1$ ) by the supernova explosion, unless the masses of the two stars are very close to one another (more specifically:  $M_1 > M_2 > M_1 - 2M_{\text{NS}}$ , where  $M_{\text{NS}}$  is the mass of the compact remnant, i.e. the neutron star). One therefore does not expect to find (many) binaries with a neutron star. Two possible solutions have already been discussed in Sect. 21.1: the supernova can occur at apastron of an eccentric orbit (eq. 21.12) and the new neutron star may be born with a kick velocity (eq. 21.15). Most important, however, is the possibility that the more massive star becomes the less massive star before it explodes as a result of mass transfer. We discuss three scenarios for this.

### 21.2.1 Origin of the Be X-ray binaries: pre-supernova case B mass transfer

The evolution of a massive binary into a Be/X-ray binary is illustrated in Figure 21.2. In this example a binary starts out with  $12$  and  $8 M_{\odot}$ , and an orbital period  $P_{\text{orb}} = 50$  days. The  $12 M_{\odot}$  star evolves first and expands after it exhausts its hydrogen, filling its Roche lobe when it crosses the Hertzsprung gap

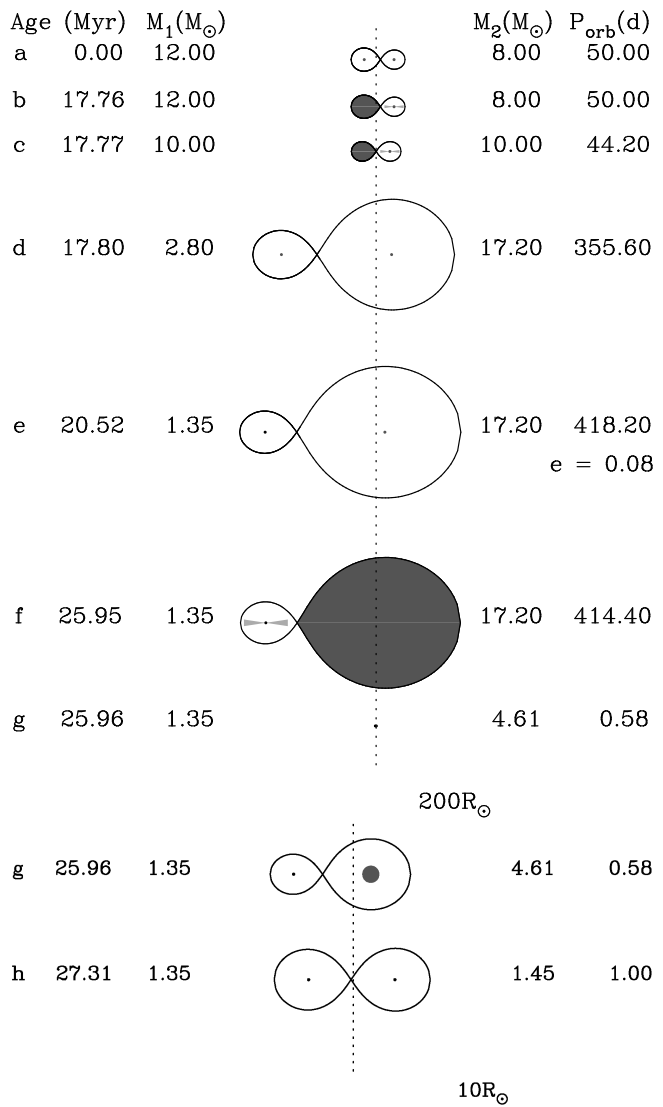


**Figure 21.2.** Conservative evolution of high-mass binary into a Be X-ray binary, and then into a binary radio pulsar. For explanation see text. Note the change of scale at phase g.

(Fig 21.2b). The binary thus evolves according to Case B, see Sect. 18.2. Since the more massive star still has a radiative envelope at this point, and the mass ratio is not far from unity, mass transfer may be conservative as has been assumed in this example. The orbital period decreases until the masses are equal (Fig 21.2c) after which the orbit expands. Mass transfer occurs on the thermal timescale of the donor star until almost the entire envelope has been transferred to the companion star; only then does the equilibrium radius of the donor star become smaller than its Roche lobe (Sect. 18.2). The  $8 M_\odot$  star has gained appreciably in mass, and rotates rapidly, due to the accretion of angular momentum with the mass. The result of the first phase of mass transfer is a binary in which the almost naked helium core of the initially more massive star is in a wide orbit around an Oe or Be star companion.

The core continues its evolution, and after a short time explodes as a supernova, leaving a neutron star of  $1.35 M_\odot$  (Fig. 21.2e). The sudden mass loss leads to an eccentricity of  $e = 0.08$  and a velocity of the center of mass of the new binary of  $v_s = 5.9 \text{ km/s}$  for an assumed symmetric explosion, according to eqs. (21.3–21.4). The neutron star may catch matter from the dense equatorial wind of the Be star and appear as an X-ray source. The wind of the Be star, too, often is transient; thus the binary is often a transient source of hard X-rays. The Be stars in Be X-ray binaries have inferred masses between  $8$  and  $20 M_\odot$ . The upper limit is thought to be due to a selection effect: more massive

stars have such strong winds that their rotation slows down quickly, and they cease having the strong equatorial outflows characteristic of Be stars. Accretion from the fast and tenuous winds of O stars is much less efficient, and does not produce a strong X-ray source unless the orbital period is  $\lesssim 10$  days.

In early computations of binary evolution it has mostly been assumed that the helium core unwrapped by mass transfer evolves pretty much in the same way as it would have done inside the whole star. By computing the evolution of unwrapped cores explicitly several authors have shown that this assumption is not correct. In particular, even the cores of very massive stars, which would have evolved into a black hole inside the full star, can evolve into a neutron star instead when the star loses its envelope at an early evolutionary stage, due to the strong Wolf-Rayet mass loss of such exposed cores. This explains why no Be X-ray binary (formed via case B mass transfer) contains a black hole. An important consequence is that one can no longer transfer conclusions about the progenitor mass of a black hole from single-star evolution to binary evolution or vice versa.

**Evolution into high-mass binary pulsars** Overflow via the inner Lagrangian point starts when the companion reaches its Roche lobe (Fig 21.2f). The extreme mass ratio ( $M_d/M_a \gtrsim 10$ ) will have caused tidal interaction to become unstable (the Darwin instability, eq. 20.1) even before Roche-lobe overflow starts, so that the neutron star will plunge into the envelope of its companion. In the case shown in Figure 21.2, the spiral-in leads to a very close binary consisting of the neutron star and the core of the Be star (Fig. 21.2g). If the helium core has too low a mass to evolve into a supernova, it will cool into a white dwarf, and the resulting binary looks like the one in which PSR 0655 + 64 is accompanied by a relatively massive white dwarf. In that case, the orbit retains the circular shape it obtained during spiral-in. Alternatively (as shown in Fig. 21.2h), continued evolution of the core leads to a second supernova explosion, which may lead to the formation of a high-mass radio pulsar binary like PSR 1913 + 16, consisting of two neutron stars in an eccentric orbit; or which may disrupt the binary. In the example shown, a symmetric explosion would disrupt the binary and a suitably aimed kick velocity is needed to produce a binary pulsar.

### 21.2.2 Origin of the supergiant X-ray binaries: case A mass transfer or spiral-in

Two very different scenarios have been discussed to explain the existence of the ‘standard’ high-mass X-ray binaries with a supergiant companion in a close orbit. The first scenario is similar to the one sketched above for the Be/X-ray binaries, involving (quasi)conservative mass transfer. The much shorter orbital periods compared to those of Be/X-ray binaries are partly due to a selection effect, as blue supergiants have faster and more tenuous winds than the equatorial outflows of Be stars (see also Sec. 21.2.1). However, also three physical effects conspire to keep the orbital periods shorter than in Be/X-ray binaries. First, the ratio of core mass to envelope mass increases with stellar mass (according to eq. 18.1) so that in a more massive binary relatively less mass is transferred, which results in less orbital expansion after conservative mass transfer (see Exercise 18.3). Second, many supergiant X-ray binaries are thought to originate from case A instead of case B, with initially very close orbits. This also explains that a neutron star can be accompanied by a very massive donor, as in the case of the binary Wray 977, in which a  $48 M_\odot$  star transfers mass to a neutron star: such a binary can form by conservative case A mass transfer even if the progenitor of the neutron star had an initial mass as low as  $25 M_\odot$ . Third, and in contrast, substantial loss of mass and angular momentum during case A mass transfer is needed to explain the properties of some neutron-star supergiant binaries with  $P_{\text{orb}} < 10$  days.

The alternative scenario involves a massive and initially very wide binary that undergoes dynamically unstable case C mass transfer. This brings the mass-receiving star inside the envelope of the donor star and initiates a common envelope event (Sect. 20.1). Friction then transfers angular mo-

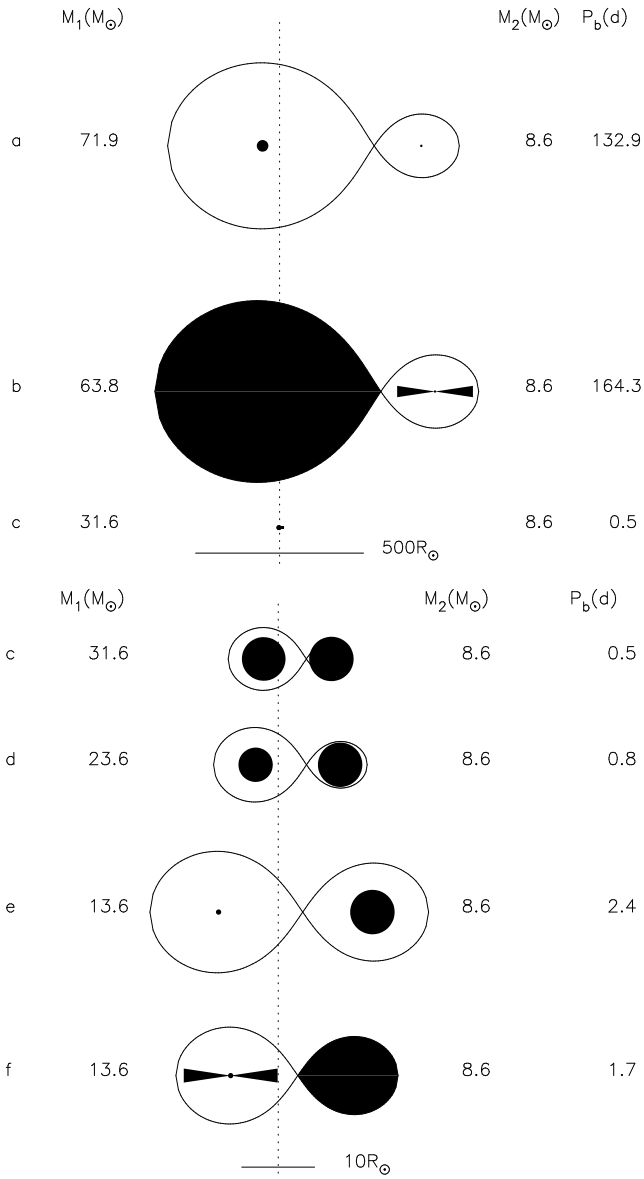


**Figure 21.3.** Drawing – to scale – of the evolution of a high-mass binary with a close initial orbit. For explanation see text; note the change in scale at phase c. The  $8.6 M_\odot$  star in phase c only barely fits in its Roche lobe. The final binary is modelled on LMC X-3.

mentum and energy from the orbital motion to the envelope of the mass donor. As a result, the orbit shrinks dramatically, until the envelope is heated so much that it escapes, leaving the core of the donor in orbit around the mass-receiver, or until both stars merge completely. This spiral-in process happens so rapidly, that the mass receiving star accretes only a tiny fraction of the envelope of the donor.

This scenario is discussed especially to explain the formation of black-hole high-mass X-ray binaries such as LMC X-3, as illustrated in Fig. 21.3. The more massive star of the binary loses some mass in a stellar wind before it fills its Roche lobe. The mass transfer is unstable, and a spiral-in ensues, bringing the core of the donor in close orbit around the virtually unchanged receiver (see eq. 20.6; phases b-c in Fig. 21.3). The donor only fits inside its Roche lobe because stars in the LMC, due to their lower metallicity, are smaller at the same mass than stars in our Galaxy. The core loses some more mass in stellar wind as it evolves to a supernova, and forms a black hole (Fig. 21.3c-e).

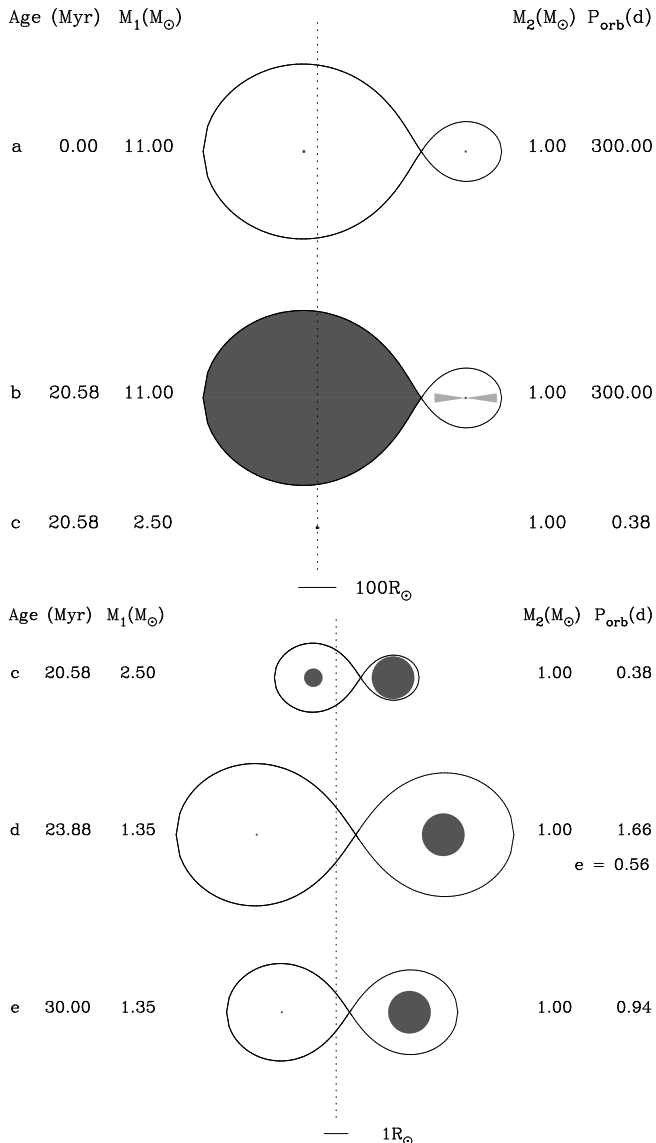


**Figure 21.4.** Evolution of a massive binary with an extreme mass ratio into a low-mass X-ray binary via a common envelope phase resulting in spiral-in, followed by the supernova explosion of the helium core of the massive star. For explanation see text. Note the change of scale at stage c.

## 21.3 Formation and evolution of low-mass X-ray binaries

The problem in producing a high-mass X-ray binary, i.e. avoiding a disruption of the binary during the supernova event, holds even more for the low-mass X-ray binaries. Mass loss via a wind of a massive star will not bring its mass below the  $1M_\odot$  of a low-mass companion. In order to keep the binary intact, one may have to invoke both a common-envelope phase and a rightly aimed kick velocity of the newly born compact star. An alternative possibility is a quiet supernova explosion, when a white dwarf is pushed over the Chandrasekhar limit and implodes. Yet another alternative is evolution of a multiple system of three or more stars.

### 21.3.1 Origin of low-mass X-ray binaries via spiral-in

The spiral-in scenario was suggested first by van den Heuvel in 1983. Eqs. (20.6,20.7) show that the initial binary must have been rather wide if a merger is to be avoided. This allows both late case B (i.e. mass transfer starting when the donor is already a red giant with a convective envelope) or case C. To

avoid a merger, case C mass transfer is preferred above case B, as the core mass will be higher and the envelope mass smaller. Consider for example a star just massive enough to evolve into a neutron star, with an initial mass of  $11 M_{\odot}$  which evolves a helium core of  $2.5 M_{\odot}$  on the giant branch (Fig. 21.4). A  $1 M_{\odot}$  companion to this core fits within its Roche lobe provided the semimajor axis is larger than  $3.3 R_{\odot}$  (Fig. 21.4c). With eq. (20.6) and assuming  $\alpha_{\text{CE}}\lambda = 1$ , we find that this requires a semimajor axis before spiral-in that is  $430 R_{\odot}$ . An  $11 M_{\odot}$  star indeed expands to fill its Roche lobe in this binary during the first giant ascent before helium ignition, i.e. mass transfer is case B. The main-sequence star is hardly affected by the spiral-in process, and emerges pretty much as it entered.

The supernova explosion of the  $2.5 M_{\odot}$  helium core causes an eccentricity  $e = 0.56$ , if a  $1.35 M_{\odot}$  neutron star is formed without a kick velocity (Fig. 21.4d). Tides quickly circularize the binary so that it ends up with the low-mass star underfilling its Roche lobe by about a factor 2 (Fig. 21.4e). Angular momentum losses may then bring the  $1 M_{\odot}$  star in contact with its Roche lobe, provided the post-supernova orbit is not too wide (see Sect. 21.3.3). In a system with a longer orbital period, mass transfer can start only after the  $1 M_{\odot}$  star evolves away from the main sequence, and expands into a (sub)giant. The boundary between these two cases depends on the mechanism for loss of angular momentum.

Thus, the spiral-in scenario does allow the formation of low-mass X-ray binaries. However in reality the scenario is more complicated than sketched above. The crucial moment in the evolution is the moment of the supernova explosion. If the binary is to remain bound, not too much mass must be lost from the system with the explosion (see eq. 21.3). This may be the case if the core of the neutron star progenitor is not too massive, i.e. if the progenitor itself is not too massive, as in the example just described. However, such relatively low-mass helium stars expand and fill their Roche lobes again after exhausting helium in their centre, leading to a renewed phase of (unstable) mass transfer to the companion. Therefore either the initial orbit must be even wider, allowing two consecutive spiral-in phases, or the neutron-star progenitor must be more massive. In that case, a well-directed kick may help to keep the binary bound. Interestingly, collapse of a massive evolved core into a black hole may also make it easier for the binary to remain bound, as a smaller fraction of the mass is expelled in that case.

PSR 1820 – 11 (see Table 19.5) is possible high-mass radio pulsar binary. The available observations also allow the companion to the pulsar to be a low-mass main-sequence star; if so, the binary would be a progenitor of a low-mass X-ray binary, along the scenario just sketched.

### 21.3.2 Origin via accretion-induced collapse

Accretion-induced collapse of a massive white dwarf as a mechanism for the formation of a neutron star was first suggested by Whelan & Iben in 1973. The progenitor of a massive white dwarf must have a mass close to those of direct progenitors of neutron stars. The close binary is therefore formed through a spiral-in, very similar to the spiral-in just described: however, the core that emerges from the spiral in now evolves into a massive white dwarf, and avoids the supernova explosion. When mass transfer is initiated, either by loss of angular momentum or by expansion of the secondary into a (sub)giant, the white dwarf accretes mass until it transgresses the Chandrasekhar limit, at which point it implodes. Little mass is lost in the implosion; most of the loss in fact may come from the change in binding energy, which is roughly:

$$\Delta M \approx \frac{3GM_{\text{WD}}^2}{5R_{\text{NS}}c^2} \approx 0.2M_{\odot} \quad (21.17)$$

where  $M_{\text{WD}}$  is the mass of the white dwarf and  $R_{\text{NS}}$  the radius of the neutron star. The smaller mass loss makes it easier for the binary to survive the supernova explosion. It is often implicitly assumed

that the kick velocity is also less for a neutron star formed by white dwarf collapse. As long as the mechanism causing the kick velocity is not known, however, there is no good reason for such an assumption.

Accretion-induced collapse as a mechanism to form a neutron star gained widespread recognition once it was realized that the magnetic field of the radio pulsar in old binaries was still in excess of  $10^8$  G. Combined with the view that the magnetic field of a neutron star decays on a time scale of a few million years, this meant that there must be young neutron stars in old binaries: accretion-induced collapse can achieve this. However, it is not clear that the magnetic field of neutron stars does indeed decay so rapidly. In the absence of rapid decay of the magnetic field of neutron stars, there is no strong case for accretion-induced collapse in the formation of low-mass X-ray binaries.

### 21.3.3 Evolution of low-mass X-ray binaries

The evolution of a low-mass X-ray binary can be described by the same methods that we discussed for other compact binaries in Sect. 20.3. The low-mass X-ray binaries with orbital periods less than about 10 hours are in many ways analogous to cataclysmic variables, and their evolution is also governed by orbital angular-momentum loss, of which an example was given in Fig. 20.1. However, the larger mass of the compact object in low-mass X-ray binaries (about  $1.4 M_\odot$  in case of a neutron star, and even larger in the case of a black hole) also allows more massive donor stars, with evolution timescales shorter than the age of the Universe. This allows the possibility of stable mass transfer in much wider orbits, driven by nuclear expansion of the donor star.

#### Evolution via donor expansion

A number of low-mass X-ray binaries, including the well-known systems Sco X-1 and Cyg X-2, have orbital periods in excess of 0.5 days, indicating that their donor stars are (sub)giants (see Fig. 19.1). In these systems, mass transfer is driven by the evolutionary expansion of the donor star. The radius and luminosity of a low-mass giant are determined mainly by its core mass (see Fig. 15.4). Results of detailed calculations can be approximated by the core-mass radius relation (20.8), or more accurately with simple polynomial relations in  $y \equiv \ln M_c/0.25M_\odot$ :

$$\ln(R_d/R_\odot) = a_0 + a_1y + a_2y^2 + a_3y^3 \quad (21.18)$$

$$\ln(L_d/L_\odot) = b_0 + b_1y + b_2y^2 + b_3y^3 \quad (21.19)$$

The values of the fitting constants  $a_i, b_i$  depend on the metallicity of the star, and are given for two metallicities, for stars in the Galactic disk, and for stars in low-metallicity globular clusters, in Table 21.1.

**Table 21.1.** Constants for the fits to the core-mass - radius and core-mass - luminosity relations for low-mass giants, according to Webbink, Rappaport, & Savonije (1983).

|              | $a_0$ | $a_1$ | $a_2$ | $a_3$ | $b_0$ | $b_1$ | $b_2$ | $b_3$ | mass range                  |
|--------------|-------|-------|-------|-------|-------|-------|-------|-------|-----------------------------|
| $Z = 0.02$   | 2.53  | 5.10  | -0.05 | -1.71 | 3.50  | 8.11  | -0.61 | -2.13 | $0.16 < M_c/M_\odot < 0.45$ |
| $Z = 0.0001$ | 2.02  | 2.94  | 2.39  | -3.89 | 3.27  | 5.15  | 4.03  | -7.06 | $0.20 < M_c/M_\odot < 0.37$ |

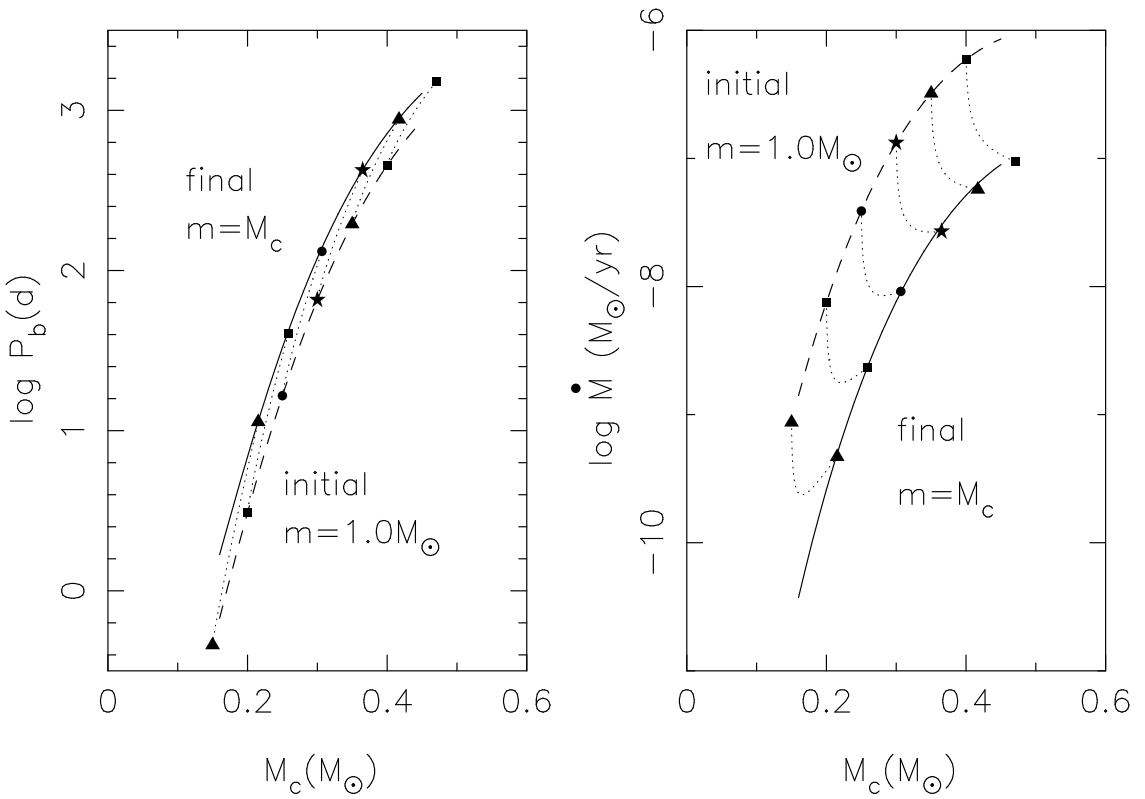


**Figure 21.5.** Orbital period and mass-transfer rate as a function of the mass of the donor core  $M_c$ , for binary evolution driven by expansion of a giant donor star. The mass-transfer rates shown all assume  $M_1 = 1.4M_\odot$  and  $\dot{M}_1 = -\dot{M}_2$ . Figure from Verbunt (2013).

The luminosity on the giant branch is almost completely due to hydrogen shell burning, and is related to the core mass  $M_c$  by

$$\dot{M}_c \approx 1.37 \times 10^{-11} \left( \frac{L}{L_\odot} \right) M_\odot / \text{yr} \quad (21.20)$$

Combining eqs. (21.18) and (21.20) gives the relation between the change in radius and the change in core mass:

$$\frac{\dot{R}_d}{R_d} = [a_1 + 2a_2y + 3a_3y^2] \frac{\dot{M}_c}{M_c} \quad (21.21)$$

In the absence of loss of angular momentum, eq. (20.18) may be rewritten

$$-\frac{\dot{M}_d}{M_d} = \frac{1}{\zeta_{\text{eq}} - \zeta_L} \left( \frac{\dot{R}_d}{R_d} \right)_{\text{ev}} \quad (21.22)$$

which completes the set of equations required to calculate the binary evolution. The orbital period and the two masses determine the radius of the giant via eq. (20.16) and hence its core mass via eq. (21.18); the core mass determines the rate of radius expansion via eq. (21.21), and with this the mass-transfer rate via eq. (21.22). Thus the evolution can be calculated without resort to detailed stellar evolution codes.

The results are shown in Figure 21.5 for  $Z = 0.02$ , the metallicity of ordinary Galactic-disk stars. It is seen that there is a strong correlation between orbital period and mass-transfer rate: in a binary

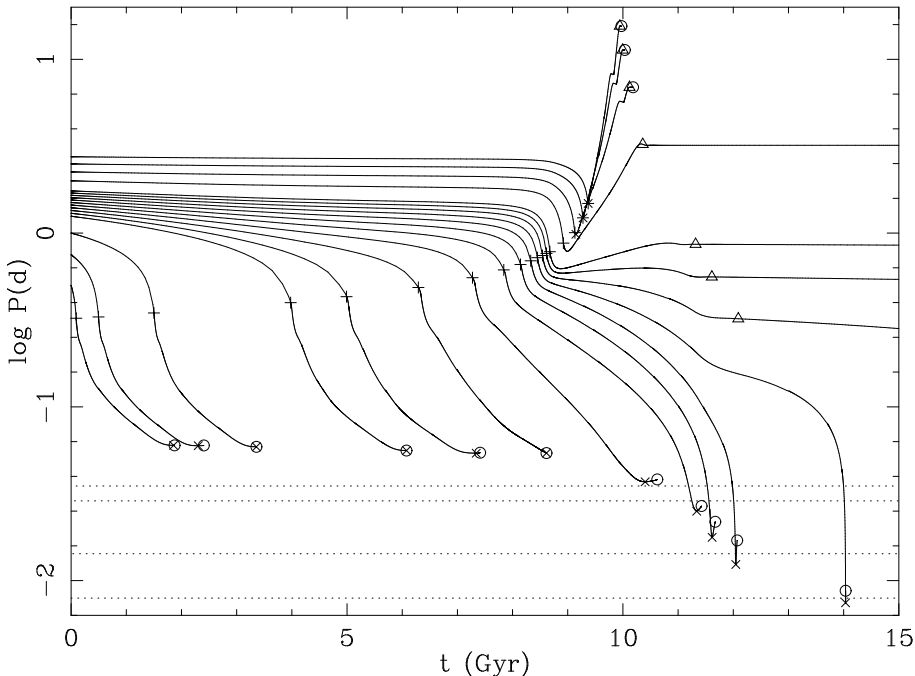


**Figure 21.6.** Evolution of the orbital periods of low-mass X-ray binaries with an initial donor mass of  $1.0 M_{\odot}$  and selected initial periods between 0.5 and 2.75 days. The curves show the results of detailed evolution calculations including angular momentum loss by gravitational radiation (eq. 20.10) as well as magnetic braking (eq. 20.14). The initial composition has  $Z = 0.01$ . The symbols mark special points in the evolution: + marks the start of Roche-lobe overflow (RLOF),  $\times$  the minimum period,  $\triangle$  the end of RLOF and  $\circ$  marks the end of the calculation. The four dotted horizontal lines show the orbital periods of the closest observed LMXBs in globular clusters: 11.4 and 20.6, and in the galactic disk: 41 and 50 minutes.

Systems with initial periods below the bifurcation period of about 1.5 days evolve to smaller orbital periods due to angular momentum loss (dominated by magnetic braking in this case) and mostly reach a minimum period of  $\approx 70$  min. Initially wider systems are dominated by nuclear expansion after the main sequence and evolve to longer periods. Systems with periods just below the bifurcation period develop helium-rich cores and can reach a minimum period as short as 10 min; however this requires strong fine-tuning of the initial period.

with a long orbital period, only a large giant fills its Roche lobe, and a large giant evolves more rapidly.

The simple calculations hold for stars beyond the subgiant branch; for subgiants, eq. (21.20) does not apply. Eqs. (21.18) and (21.19) are valid for red giants in thermal equilibrium. Detailed calculations show that this is a good approximation until the donor envelope has been almost fully exhausted.

#### 21.3.4 Origin of low-mass binary radio pulsars

The evolutionary scenario for low-mass X-ray binaries with (sub)giant donors received strong confirmation with the discovery of radio pulsars in circular orbits with a very low mass-function, and hence a probable companion mass of  $0.2 - 0.4 M_{\odot}$  listed as low-mass binary radio pulsars in Table 19.5. The scenario discussed in the previous subsection automatically leads to such a binary: once the envelope of the giant donor is exhausted, the giant's core remains and cools into a white dwarf. The orbital period of the current binary sets the radius of the giant immediately prior to the end of mass transfer, and thus its core mass. Thus, the orbital period  $P_{\text{orb}}$  of the radio pulsar should be correlated to the

mass  $M_{wd}$  of its white-dwarf companion. Approximately (from Table 20.1):

$$P_{\text{orb}} \approx 40 \text{ days} \left( \frac{M_{\text{wd}}}{0.25 M_{\odot}} \right)^{5.5} \quad (21.23)$$

valid for circular orbits with  $P_{\text{orb}} \gtrsim 20$  days.

The low eccentricity of the orbits of low-mass binary radio pulsars indicates that orbital circularization must have occurred following the formation of the neutron star. The low mass-functions indicate white dwarf companions to the radio pulsars with masses lower than the  $\approx 0.6 M_{\odot}$  expected for a white dwarf evolved from a single star. Both these observations are explained by the scenario in which a giant fills its Roche-lobe – causing strong tidal forces and hence rapid circularization, and transfers its envelope to the neutron star – thereby cutting off the growth of its core. The mass transfer also explains the short pulse period of the radio pulsars in these binaries as a consequence of the spin-up of the neutron star as it accretes mass from an accretion disk.

Interestingly, the realization that rapidly rotating radio pulsars may emerge from low-mass X-ray binaries came with the discovery of a single radio pulsar, PSR1937 + 21. Its extremely rapid rotation can be understood as the consequence of accretion of a substantial amount of mass  $\gtrsim 0.1 M_{\odot}$  from an accretion disk, by a neutron star with a low magnetic field. The magnetic field of PSR1937 + 21 is indeed low (see Table 19.5). In order to explain the absence of any companion, several destruction mechanisms were suggested. Detailed scrutiny of these mechanisms showed that none of them are convincing. The discovery of another millisecond pulsar brought a more likely solution: PSR1957+20 is heating its companion enough to evaporate it.

## Exercises

**21.1** The system V635 Cas (see Table 19.4) is an example of a Be X-ray binary. Assume a canonical mass of  $1.35 M_{\odot}$  for the neutron star and a mass of  $15 M_{\odot}$  for the Be star (typical of the Be components in such binaries).

- (a) Why is it reasonable to assume a circular pre-supernova orbit in this system?
- (b) Assuming the supernova was symmetric, compute the mass of the neutron-star progenitor just before the explosion.

**21.2** Consider the example binary system discussed and plotted in Fig. 21.1. Assuming the pre-explosion orbit is circular with  $a = 100 R_{\odot}$ , compute the maximum kick velocity for which a star of  $1 M_{\odot}$  can survive the supernova explosion of its  $10 M_{\odot}$  companion without the binary being disrupted.

**21.3** Her X-1 is an X-ray binary with an orbital period of 1.7 days in which a main-sequence or subgiant star of  $2.0 M_{\odot}$  is transferring mass to its neutron star companion, which is observed as an X-ray pulsar. Fig. 21.7 shows two possible evolution scenarios.

The first one (the standard scenario) starts with a massive NS progenitor ( $10 M_{\odot}$ ) and a  $2 M_{\odot}$  companion in a wide orbit (stage 1), which evolves via case C mass transfer (stage 2) and spiral-in into a close binary consisting of the helium core of the progenitor and the unchanged  $2 M_{\odot}$  companion with a short orbital period (stage 3). The helium core explodes and leaves a  $1.4 M_{\odot}$  neutron star in an eccentric orbit (stage 4). Finally, after tidal interaction has circularized the orbit, Roche-lobe overflow starts and an X-ray binary with the observed parameters is formed (stage 5).

- (a) Reconstruct this evolution scenario by filling in the missing values in the Figure, using the formulae encountered in the lectures. Also compute the eccentricity induced by the supernova at stage 4. Assume the SN explosion was symmetric (i.e. ignore the possible kick velocity) and assume that the spiral-in can be described by the energy balance prescription with  $\alpha_{\text{CE}} = \lambda = 1$ . Also compute the system velocity of the binary after the explosion.

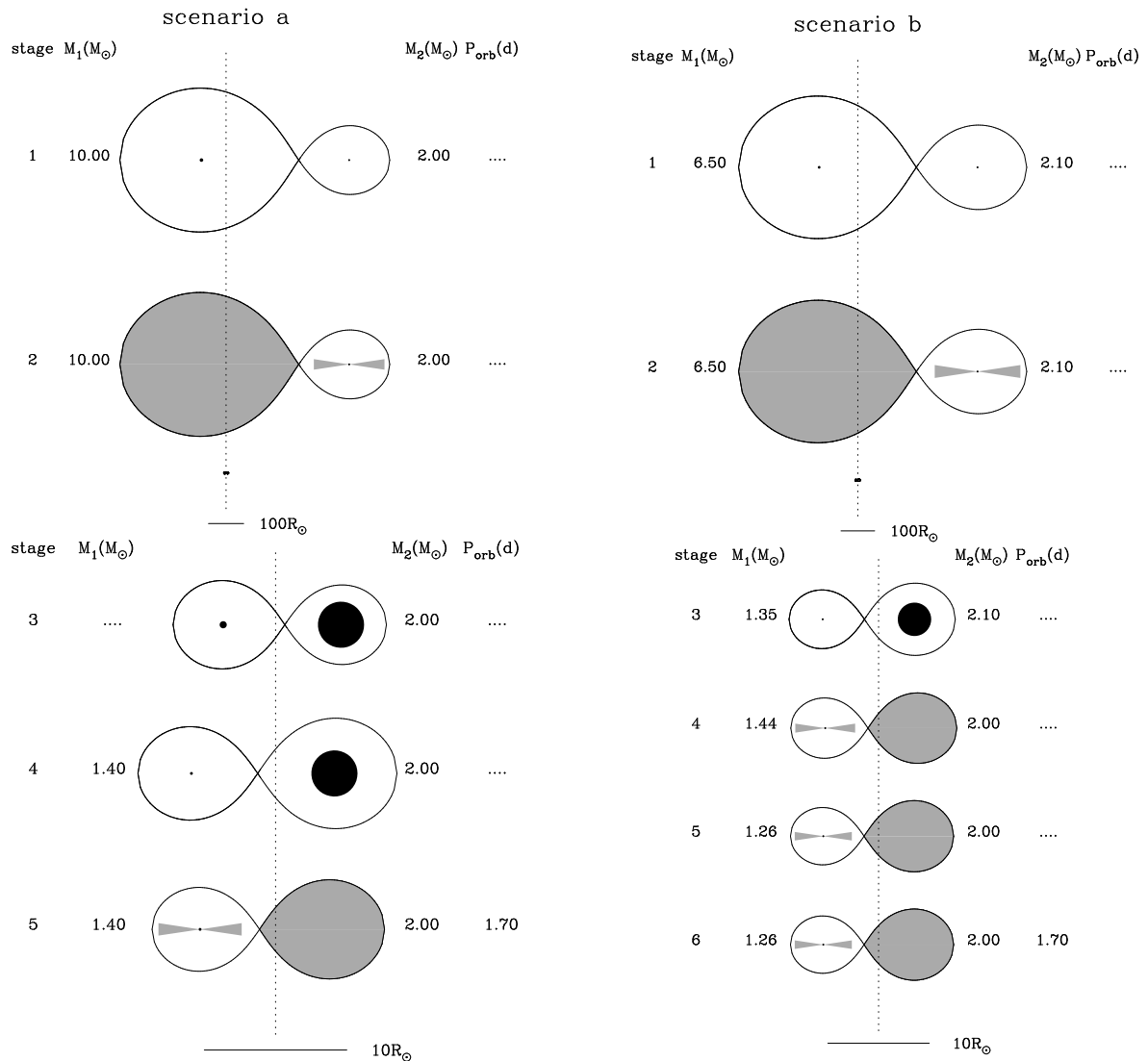


**Figure 21.7.** Drawing (to scale) of two scenarios for the evolution of Her X-1. Left: the standard scenario involving a massive primary; right: the accretion-induced collapse scenario. Note the change in scale after the spiral-in phase (stage 3).

- (b) The second scenario (accretion-induced collapse) involves an intermediate-mass progenitor, which initially forms a massive white dwarf ( $1.35 M_{\odot}$ ) after case C mass transfer and spiral-in. When the companion fills its Roche lobe, it transfers mass to the white dwarf and pushes it over the Chandrasekhar limit when its mass is  $1.44 M_{\odot}$  (stage 4). A neutron star of  $1.26 M_{\odot}$  is formed (stage 5). Compute the eccentricity and system velocity for this case, assuming no kick occurs.

Note: Her X-1 is at a distance of  $z \approx 3$  kpc from the Galactic plane. If it was born in the plane, where the high-mass progenitors of neutron stars are, then the velocity as calculated in (b) is too low to carry it to its current position. Therefore accretion-induced collapse is not an option for Her X-1. To show this conclusively one must also investigate scenarios with kick velocities.

- 21.4** Consider the low-mass X-ray binary V4134 Sgr listed in Table 19.4. In this exercise, assume that the X-ray source is a neutron star (with  $M = 1.4 M_{\odot}$  and  $R = 10$  km) and that the measured X-ray luminosity is the total accretion luminosity. Also assume the mass of the binary is conserved during mass transfer.

- (a) Use the observed properties to compute the mass transfer rate in this system.
- (b) Consider the orbital period of V4134 Sgr. Without doing any actual calculations, argue which of the following processes could be responsible for driving mass transfer in this system:
- nuclear expansion of the donor
  - orbital angular momentum loss by gravitational radiation
  - orbital angular momentum loss by magnetic braking
  - exchange of orbital and spin angular momentum by tidal interaction.
- (c) Compute the expected mass transfer rate if mass transfer is driven by (1) gravitational radiation, and (2) by magnetic braking. Compare your answers to the result you obtained for (a): which process is most likely to drive the observationally inferred mass transfer rate?
- 21.5** Now consider the low-mass X-ray binary Sco X-1, again referring to Table 19.4. Make the same assumptions as in exercise 21.4.
- (a) Consider the various types of donor star summarized in Table 20.1. Which of these are possible donors of Sco X-1?
  - (b) Assume from now on that the donor is (just) on the red giant branch and has a mass of  $1.0 M_{\odot}$ . Compute the expected mass transfer rate from nuclear expansion of the donor, and compare to the mass transfer rate inferred from its observed X-ray luminosity.  
Note: instead of eqs. 21.18–21.19, you may also use the simpler (somewhat less accurate) relations between core mass, radius and luminosity given in Table 20.1 and

$$\frac{L}{L_{\odot}} = 2.3 \times 10^5 \left( \frac{M_c}{M_{\odot}} \right)^6$$

# Bibliography

- Darwin, G. H. 1879, Royal Society of London Philosophical Transactions Series I, 170, 1
- de Mink, S. E., Pols, O. R., & Hilditch, R. W. 2007, A&A, 467, 1181
- Gies, D. R., Bagnuolo, Jr., W. G., Ferrara, E. C., et al. 1998, ApJ, 493, 440
- Hjellming, M. S. & Webbink, R. F. 1987, ApJ, 318, 794
- Hut, P. 1980, A&A, 92, 167
- . 1981, A&A, 99, 126
- Iben, I. J. & Livio, M. 1993, PASP, 105, 1373
- Nelemans, G., Verbunt, F., Yungelson, L. R., & Portegies Zwart, S. F. 2000, A&A, 360, 1011
- Nelson, C. A. & Eggleton, P. P. 2001, ApJ, 552, 664
- Packet, W. 1981, A&A, 102, 17
- Pols, O. R. 1994, A&A, 290, 119
- Soberman, G. E., Phinney, E. S., & van den Heuvel, E. P. J. 1997, A&A, 327, 620
- van der Sluys, M. V., Verbunt, F., & Pols, O. R. 2006, A&A, 460, 209
- Verbunt, F. 2013, Compact Binaries (Lecture notes, Radboud University Nijmegen)
- Verbunt, F. & Phinney, E. S. 1995, A&A, 296, 709
- Webbink, R. F., Rappaport, S., & Savonije, G. J. 1983, ApJ, 270, 678
- Wellstein, S., Langer, N., & Braun, H. 2001, A&A, 369, 939
- Zahn, J.-P. 1977, A&A, 57, 383